AN ABSTRACT OF THE DISSERTATION OF

Fabian A. Gomez for the degree of Doctor of Philosophy in Oceanography presented on December 16, 2015.

Title: Modeling Transport, Retention, and Growth of Early Life Stages of Small Pelagic Fishes in the Southern Humboldt System.

Abstract approved: _____
Harold P. Batchelder Yvette H. Spitz

Small pelagic fishes (SPF), such as anchovies and sardines, are ecologically important due to their large abundance and intermediate trophic position that links plankton production to upper trophic levels. They are also economically important, supporting large fisheries that contribute to one fourth of the world fish landings. Reproductive success in SPF strongly depends on environmental factors acting on early life stages (ELS). Among these factors are ocean circulation, habitat temperature, prey and predators. Understanding the coupling between ocean circulation and ELS is relevant to obtain insights on the processes that control SPF abundance. Using a numerical modeling approach, this dissertation examines spatiotemporal patterns in dispersal, growth and survival of ELS of anchovy (*Engraulis ringens*) and common sardine (*Strangomera bentincki*) in the southern Humboldt System (off central Chile). Three model components are integrated: 1) a realistically driven three-dimensional high-resolution ocean circulation model, coupled to an eight-component lower trophic level model (LTLM), which reproduces the main physics and plankton dynamics experienced by fish ELS; 2) a particle-tracking model (PTM) to simulate ELS dispersal; and 3) an Individual Based Model (IBM) of bioenergetics to simulate ELS development, growth, and survival. A combination of remotely sensed observations and the outputs of the ocean model are used in Chapter 2 to document the impact of intraseasonal upwelling variability on plankton abundance and structure. Intraseasonal changes in phytoplankton are consistent with

alongshore wind disturbances due to Madden-Julian oscillations. The phytoplankton intraseasonal variability exhibits largest amplitude in spring-summer, a feature related to the background seasonal conditions in ocean stratification and light. Chapter 3 documents variability in ELS dispersal using the PTM. We examine if patterns in anchovy and sardine spawning promote shelf retention and prey availability for ELS. We show that the timing of spawning (Aug-Oct) is only partially linked to high retention, but also demonstrate that the main spawning locations along the coast favor high coastal retention year-round. Experiments with ontogenetic diel vertical migration (ODVM) schemes increase retention and spawning-to-nursery connectivity. We suggest that the main spawning period is mostly explained by enhanced prey availability and connectivity, whereas inner shelf spawning and ODVM are the main strategies to increase retention of larvae nearshore. Chapter 4 examines anchovy ELS development, growth, and survival derived from an IBM. Mortality rate is assumed to decline with individual development and size, and increases with temperature. Dispersal patterns strongly determine individual growth and survival. Passive individuals initialized at 5 m depth growth fast near the coast, but they experience strong food limitation when advected far offshore. Passive individuals initialized at 20 m depth have the largest nearshore retention, but slow growth and survival due to low temperature and prey abundance. A favorable trade-off between high retention and growth was derived from individuals initialized at 10 m. Ontogenetic and diel vertical migration increased retention and survival over the shelf, but decreased larval growth. This study advances understanding of the interplay of multiple processes that modulate the timing and intensity of spawning, distribution, growth and survival of small pelagic fish in coastal upwelling ecosystems. It also documents the need for more and better field studies to represent better crucial early life stage traits and processes, such as vertical distribution, larval foraging, mortality, and bioenergetics.

Modeling Transport, Retention, and Growth of Early Life Stages of Small Pelagic Fishes in the Southern Humboldt System

by
Fabian A. Gomez

A DISSERTATION

submitted to

Oregon State University

in partial fulfillment of
the requirements for the
degree of

Doctor of Philosophy

Presented December 16, 2015
Commencement June 2016

Doctor of Philosophy dissertation of Fabian A. Gomez presented on December 16, 2015.

APPROVED:

Co Major Professor, representing Oceanography

Co Major Professor, representing Oceanography

Dean of the College of Earth, Ocean and Atmospheric Sciences

Dean of the Graduate School

I understand that my dissertation will become part of the permanent collection of Oregon State University libraries. My signature below authorizes release of my dissertation to any reader upon request.

Fabian A. Gomez, Author

ACKNOWLEDGEMENTS

I thank my co-advisors, Drs. Hal Batchelder and Yvette Spitz, for their scientific guidance and support during my doctoral path in the College of Earth, Ocean and Atmospheric Sciences (CEOAS). They gave me deep insights in population ecology, oceanography, and numerical modeling, helping me to develop better my scientific questions. They also assisted me with the multiple logistic aspects of my research. It was great to interact with them. I express my gratitude to my committee members, especially Drs. Jessica Miller and Ted Strub by their valuable suggestions to my research. Thanks to Vincent Combes, for his worthy recommendations that helped to improve the ocean circulation model, and Brie Lindsey who shared her insights on Individual Based Modeling. Thanks to all friends, professors, and colleagues who contributed to my personal development and scientific formation. Specially, I recognize professors Samuel Hormazabal (Catholic University of Valparaiso) and Aldo Montecinos (University of Concepcion) from Chile, who strongly motivated me to pursue my Ph.D. at Oregon State University (OSU), as well as to Rogelio Gomez, Rosa Romero, and M. Dolores Vazquez for their unconditional support in this process. Finally, I am thankful for the economic support provided by the Chilean National Commission of Science and Technology (CONICYT), the Fulbright Student Program, OSU Graduate School, and CEOAS, who all made my stay in Oregon possible.

TABLE OF CONTENTS

Page

TABLE OF CONTENTS (Continued)

Page

LIST OF FIGURES

LIST OF FIGURES (Continued)

Figure Page

LIST OF TABLES

1. Introduction

Small pelagic fish are important species in coastal upwelling ecosystems. They have relatively short life spans (~3 years), fast growth, high fecundity and mortality rates, and highly variable annual recruitment rates that are strongly influenced by density-independent factors (Lasker, 1975; Parrish *et al*., 1983; Pauly and Tsukuyama, 1987; Schwartzlose *et al*., 1999; Checkley *et al*., 2009). Small pelagic fish are intermediate trophic levels, transferring energy from phyto- and zooplankton to upper trophic levels, such as tuna, mackerel, sea birds and marine mammals (Rice, 1995). That intermediate trophic position along with large interannual changes in their abundance exerts a significant impact on the biomass and structure of both plankton and piscivorous community (Cury *et al*., 2000; Shannon *et al*., 2004). In addition to their key ecological role, small pelagic fish are economically important species that contribute to about one fourth of the world total fish landing (FAO, 2012). Consequently, small pelagics have been the subject of important regional and international research programs (GLOBEC SPACC, IDYLE, others), focused on understanding the leading factors determining recruitment variability.

The most important small pelagic fishes in the southern part of the Humboldt Current System (HCS) (off central Chile, Fig. 2.1) are anchovy (*Engraulis ringens*) and common sardine (*Strangomera bentincki*). The former has a broad distributional range from Ecuador to southern Chile, whereas the latter is an endemic Chilean species distributed between 30° and 42°S (Arrizaga, 1981; Serra, 1983). Both species inhabit a relatively narrow (10-80 km wide) and highly productive continental shelf, sharing similar biological traits and ecological niche (Castro *et al*., 2000; Cubillos *et al*., 2001; Gerlotto *et al*., 2004; Llanos-Rivera *et al*., 2004). Anchovy and sardine are omnivorous, but zooplankton is the main prey in terms of carbon ingestion (van der Lingen *et al*., 2009; Llanos-Rivera *et al*., 2004; Yanez-Rubio *et al*., 2011). Although they are multiple spawners, able to spawn year-round, their main reproductive period occurs in late winter and early spring (Cubillos *et al*., 2007; Claramunt *et al*., 2013). Species differences in the

spawning activity have been reported, with anchovy having a more protracted spawning season and a less marked reproductive peak than sardine (Cubillos *et al*., 2009). Fishery recruitment occurs in summer and fish sexual maturity is reached during the first year (Cubillos *et al*., 2001).

Anchovy and sardine support a large purse-seiner fishery off central Chile, which reported annual landings of about 500 thousand tons during the last decade (FAO, 2012). Because only two or three annual year classes constitute most of the adult stock, the fishery is strongly dependent on the recruited cohort size (Cubillos *et al*., 2002; Castillo et al., 2005). The impact of environmental factors on survival of the early life stages appears to drive most of the recruitment variability (Cubillos and Arcos, 2002; Betrand *et al*., 2004; Gomez *et al*., 2012). Recruitment appears to be linked to adult stock size only at low spawning biomass levels (Zheng, 1996). Cubillos and Arcos (2002) indicated that strong upwelling favorable winds and negative sea surface temperature (SST) anomalies during spring, i.e. the pre-recruitment period, could favor high sardine recruitment. Consistent with that, Gomez *et al*. (2012) found a positive relationship between sardine recruitment and wind-driven changes in phytoplankton biomass, suggesting that enhanced prey availability during springs with strong upwelling could increase survival of larval and juvenile sardine. There are also links between alongshore wind, phytoplankton production, and El Nino–Southern Oscillation (ENSO), with weak winds and negative phytoplankton concentration anomalies associated with warm El Nino years (Montecinos and Gomez, 2010; Gomez *et al*., 2012). Relationships between environmental indices and anchovy recruitment off central Chile remain elusive. However, anchovy and sardine recruitments appear to be negatively correlated, most likely indicating density-dependent interactions between species (Cubillos and Arcos, 2002; Pedraza-Garcia and Cubillos, 2007). Although the described statistical relationships are useful to identify potential factors influencing recruitment success in small pelagic fish, poor understanding of the mechanisms determining spatiotemporal

variability in fish early life stage survival limits our ability to predict fluctuations in fish cohort size.

Reproductive success in small pelagic fish emerges from a complex set of fish-environment interactions determining food availability, growth, and predation risk at multiple spatiotemporal scales (Hjort, 1914; Lasker, 1975; Cushing, 1975, 1990; Miller *et al*., 1988; Cury and Roy, 1989; Sinclair and Illes, 1989; Bakun, 1996; Bertrand *et al*., 2004). Survival of fish early life stages is tightly coupled to ocean circulation, as the latter determines the spatiotemporal patterns of prey and predator abundance, as well as changes in abiotic properties, such as temperature, salinity, and oxygen. Upwelling promotes high plankton production that fosters growth of feeding larvae and juveniles, but also can transport eggs and larvae away from the most productive coastal regions, potentially increasing the risk of starvation and predation (Parrish *et al*., 1983). Besides, upwelling variability creates strong spatiotemporal patterns of water temperature, a property that influences most biological vital rates, including early life stage duration and individual growth, that have a strong impact on fish survival (Castro and Hernandez, 2000; Xu *et al*. 2013; Batchelder *et al*., 2013).

Understanding the coupling between reproductive strategy of small pelagic fish and regional scale ocean dynamics and hydrography is relevant to identifying critical aspects in the life cycle of small pelagic fish, and foreseeing potential population response associated with disturbances (natural or human induced) in both population and ecosystem phenologies. However, many field studies are usually limited in their spatiotemporal extent and resolution, which prevents the appropriate observation of ecosystem and fish dynamics modulating the fish reproductive strategy. Despite the advances in understanding key aspects in population ecology of anchovy and sardine (Checkley *et al*., 2009), relevant processes that define their reproductive success, such as dispersal, retention, and growth of larvae, remain poorly known.

The main objective of this dissertation is to provide insights on the underlying processes determining the spawning strategies (timing and location) of small pelagic fish by examining the interplay between environment variability and ichthyoplankton fate. A numerical model approach was developed to simulate interactions between fish and dominant environment patterns. In this approach, an Eulerian model system that simulates realistic, three-dimensional, time evolving ocean physics, as well as nutrients and lower trophic level components (phyto- and zooplankton types), is integrated with Particle-Tracking and Individual-Based models. Thus, population and individual aspects difficult to measure directly, like larval dispersal and growth, respectively, could be derived. Coupled Eulerian-Lagrangian/IBM models are powerful tools to integrate existing knowledge, from small pelagic fish biology to ecosystem and climate-system patterns, producing mechanistic explanations for the drivers of fish population variability (Curchitser *et al*., 2013; Rose *et al*., 2015). They can explore plausible fish responses linked to poorly known biological and behavioral traits, helping to identify relevant fish or environmental dynamics needed for observational studies (Rose, 2012). The next three dissertation chapters show different integration levels within the modeling framework, from the physical-biological Eulerian Model (Chapter 2), to the particle-tracking model (Chapter 3), to the more complex Individual Based Model (Chapter 4).

Previous studies showed that intraseasonal (30-to-80 day period) wind variability over the HCS is strongest off central Chile (Hormazabal *et al*., 2002; Rutllant *et al*., 2004; Rahn, 2012), and can have a significant impact on the coastal upwelling ecosystem. Chapter 2 examines subseasonal upwelling dynamics, documenting for the first time the impact of intraseasonal wind oscillations on phytoplankton biomass. Intraseasonal changes in plankton biomass, structure and distribution were derived from satellite data and the regional ocean model outputs. The regions and season with the strongest intraseasonal changes on phytoplankton biomass and sea surface temperature were identified. The intraseasonal changes were consistent with disturbances linked to Madden-Julian

oscillations. Findings about the impact of intraseasonal wind fluctuations on coastal retention and stage development and growth are included in subsequent chapters.

Linked to the fish evolutive history, spawning patterns emerge from multiple environmental constraints that determine fish cohort survival (Sinclair, 1988; Cury and Roy, 1989). Ichthyoplankton shelf-retention is thought to play a lead role on larval survival, as the shelf is the richest food environment for larvae. Following previous particle tracking model (PTM) studies on ichthyoplankton retention (Lett *et al*., 2007; Brochier *et al*., 2008; Parada *et al*., 2012), Chapter 3 examines the hypothesis that the seasonal cycle of coastal retention and prey abundance determine the main reproductive timing of both anchovy and sardine (Castro *et al*., 2000; Cubillos *et al*., 2001). We documented the main shelf-retention patterns and prey fields experienced by virtual larvae during their dispersal trajectories. Three-day resolution time series of model indices for the period 2002-2008 were generated for different particle initial conditions, which allowed identification of both seasonal and intraseasonal patterns. In addition, the role of vertical migration on dispersal was evaluated using simple ontogenetic vertical migration schemes.

Chapter 4 examines the spatiotemporal variability in larval growth and survival derived from a bioenergetic model, the latter based on previous modeling studies of Peruvian anchovy by Xu *et al*. (2013, 2015), Mediterranean anchovy by Politikos *et al*. (2011, 2015), and California anchovy by Rose *et al*. (2015). Individual fish size is a critical variable that influences resource use, physiological rates, and predation risk, therefore determining ecological niche (Werner and Gilliam, 1984). Large and fast growing larvae are thought to have less predation risk than small and slow growing larvae (Miller *et al*., 1998). Although the relevance of growth variability to fish cohort survival is widely recognized, if not assumed, we have a very limited understanding of the details of how spatiotemporal patterns in larval growth and survival are related to in situ environmental factors. Obtaining estimates of larval growth and size structure in the field is difficult,

and it is very difficult to relate patterns of larval growth to experienced environmental conditions without knowledge of the space and time history of the individual, which is never available. Given these difficulties, our approach was to use a bioenergetic model embedded in a fully described biophysical model that provides the full environment experienced by the individual fish to examine growth patterns, and evaluate plausible cohort mortality rates, as functions of body size and environmental conditions (Megrey *et al*., 2007).

2. Intraseasonal patterns in coastal phytoplankton biomass off central Chile

2.1. Abstract

Environmental intraseasonal oscillations (30-130 day) can strongly affect plankton production in upwelling systems, but intraseasonal dynamics are usually overlooked in ecological studies. Although most of the wind variability occurs at submonthly frequencies, we found that wind oscillations of ca. 50 days can have a large impact on coastal phytoplankton biomass off central Chile. Our study examined the period 2003-2011 and used data from satellite sensors, together with outputs from a realistically forced eddy-resolving physical-biological model. The spectral features of SST (satellite and modeled) and phytoplankton biomass (satellite chlorophyll and modeled phytoplankton) revealed a strong intraseasonal signal over the 30-to-80 day band. This intraseasonal signal was linked to wind-driven upwelling, showing large amplitude in spring-summer and small in fall-winter. The seasonal dependence of the intraseasonal phytoplankton signal is related to the background seasonal conditions in ocean vertical stratification and light. Every spring-summer season, from 3 to 5 upwelling oscillations of ~50-day period occurred. Biological model outputs suggest that these oscillations determine changes in plankton vertical distribution and community structure. The wind stress anomalies that drove the strongest upwelling oscillations showed a poleward progressing pattern and were associated with Madden Julian Oscillation disturbances. Our results highlight the importance of environmental fluctuations shorter than the seasonal as modulators of SST and phytoplankton dynamics, which could have strong implications for the life cycle of higher trophic level species, including commercially important fishes.

Keywords: Intraseasonal variability, coastal upwelling, phytoplankton, chlorophyll, central-Chile, Humboldt Current System, Madden-Julian Oscillation

2.2. Introduction

The Humboldt Current System (HCS), located along the west coast of South America, is characterized by large phytoplankton production linked to wind-driven upwelling of cold and nutrient-rich waters (Strub *et al.* 1998). The high phytoplankton production supports huge populations of small pelagic fish, such as anchovy and sardine, which are economically important resources for the region (FAO, 2012). Decadal, interannual and seasonal oceanic and atmospheric variability have strong impacts on the Humboldt ecosystem (e.g.: Chavez *et al*., 2003; Escribano *et al*., 2004; Bertrand *et al*., 2004). Subseasonal variability, here defined as environmental oscillations within the 5 to 130 day band, strongly influences ocean physical dynamics (Shaffer *et al*., 1999; Hormazabal *et al*., 2001; 2002; Renault *et al*., 2009; 2012; Dewitte *et al*., 2011; Belmadani *et al*., 2012; Illig *et al*., 2014), but its impact on the upwelling ecosystem is less well documented.

A main component of the subseasonal band is the intraseasonal variability, which includes oscillations from 30 to 130 days. Intraseasonal upwelling variability (usually measured as SST anomaly) in the HCS is linked to both remotely forced coastal-trapped waves (CTW) and local winds (Hormazabal *et al*., 2001; Dewitte *et al*., 2011). The impact of the intraseasonal CTW on the HCS decreases southward (Shaffer *et al*., 1999; Belmadani *et al*., 2012), while the intraseasonal wind variability increases south of 25°S, reaching a maximum off central Chile (Hormazabal *et al*., 2002; Rahn, 2012). At 33°S, local winds explain most of the SST variability in the intraseasonal band (Hormazabal *et al*., 2001). The strong intraseasonal wind variability off central Chile is concomitant with an intermittent atmospheric low-level jet, a mesoscale feature characterized by strong equatorward winds (>10 m s^{-1}) on a spatial domain roughly 400 km wide and 1,000 km long, with events lasting several days (Garreaud and Munoz, 2005; Renault *et al*., 2009). The synoptic variability associated with the atmospheric jet appears to be intraseasonally modulated by Madden-Julian Oscillation (MJO) disturbances (Rahn, 2012). Previous

studies that examined the upwelling signature associated with the atmospheric jet off central Chile show significant SST variability at the submonthly and intraseasonal bands (Renault *et al*. 2009; 2012), though variability above 60 days was not examined. In addition, the SST response to wind stress varies seasonally with maximum correlation in spring and minimum in winter.

The impact of intraseasonal upwelling variability on phytoplankton production remains unknown off central Chile. Intraseasonal wind anomalies within the HCS have maximum amplitude near Point Lavapie at 37°S (Rahn, 2012) suggesting that significant phytoplankton responses linked to Ekman dynamics and nutrient availability could be expected. We hypothesize that intraseasonal wind oscillations will modulate phytoplankton production, composition and distribution. Changes in phytoplankton biomass/structure most likely will impact higher trophic levels, especially the early life stages that rely on plankton production to grow and survive. Consequently, we need to identify where and when the responses of phytoplankton to intraseasonal winds are the strongest.

This study describes wind-driven intraseasonal variability in coastal phytoplankton biomass off central Chile. We use an approach similar to that of Goubanova *et al*. (2013) to determine the intraseasonal patterns in wind stress, SST, and phytoplankton biomass. Our main goals are 1) to characterize the dominant intraseasonal variability in wind stress, SST, and phytoplankton biomass, identifying the locations, season, and frequency bands where that variability is the strongest; 2) to examine the response of SST and phytoplankton biomass to intraseasonal wind stress anomalies, including its seasonal modulation; 3) to explore the intraseasonal changes in plankton vertical distribution and species composition driven by wind; and 4) to identify large-scale atmospheric anomalies linked to the intraseasonal phytoplankton variability. The analyses are based on data from satellite sensors and output from a coupled physical-biological regional ocean model.

Satellite data products, the numerical model configuration, and the methodological approach are described in section 2. Section 3 presents the main spatial and spectral patterns of the subseasonal variability in the satellite and model data. In Section 4, we focus on the 30-to-80 day variability, exploring the connection among wind stress, SST and surface phytoplankton anomalies. Section 5 describes the simulated intraseasonal dynamics of phyto- and zooplankton occurring below the surface. Section 6 discusses the main results, describing mechanisms associated with the seasonal changes in the intraseasonal SST and phytoplankton signal, and the atmospheric disturbances linked to the strongest intraseasonal fluctuation in phytoplankton production. Concluding remarks are presented in Section 7.

2.3. Data and Methods

2.3.1. Satellite products

Daily surface wind stress data with a 0.25° spatial resolution were obtained from the Cross Calibrated Multi-Platform project (CCMP, L3.0; Atlas *et al*., 2011). Daily 1 km chlorophyll-a (OC3 algorithm) and SST data were obtained from level-2 products of the Moderate Resolution Imaging Spectro-radiometer MODIS-Aqua mission (http://oceancolor.gsfc.nasa.gov). Gaps in MODIS satellite data due to cloud coverage were filled using the Data Interpolating Empirical Orthogonal Function (DINEOF) method, with a 31-day window. DINEOF has shown to be robust in conserving time series variance in previous satellite-based studies of the southern HCS (Correa-Ramirez *et al*., 2012; Morales *et al*., 2013). In contrast to the northern HCS, which has a high frequency of satellite missing data due to cloud coverage, the southern HCS has a higher percentage of cloudless days (>35%) and temporal gaps in data are usually shorter than 4 days (Morales *et al*., 2013).

2.3.2. Numerical model

The Rutgers version of the Regional Ocean Model System (ROMS) (Shchepetkin and McWilliams, 2005) was used to simulate the physical dynamics of the upwelling system. The model domain extends from 30.5° to 43°S, and from the coast to 81°W (Fig. 1), with a mean horizontal resolution of 3 km. The 40 terrain-following vertical layers are arranged to provide enhanced vertical resolution near the surface and bottom ($\theta_s = 6$, $\theta_b = 0.2$). This resolution allows realistic upwelling dynamics to be reproduced over the relative narrow shelf off Chile. Model bathymetry is from Smith and Sandwell (1997) version 12.1 having 1 arc degree resolution.

The biological model is an 8-component NPZD model with nitrate (NO_3), ammonium (NH_4), small phytoplankton (PS, flagellates and dinoflagellates), large phytoplankton (PL, diatom), small zooplankton (ZS, microzooplankton), large zooplankton (ZL, mesozooplankton), and small (DS) and large detritus (DL). The model is parameterized similarly to the NEMURO model (Kishi *et al*., 2007). The main differences are the elimination of the silica cycle, dissolved organic nitrogen (DON), and predatory zooplankton in our model. Silica does not appear to limit diatom growth in the southern HCS. The predatory zooplankton grazing was implicitly incorporated in the mortality rate of diatom and zooplankton. The non-living particulate organic nitrogen was divided into small and large detritus with different sinking rates, and recycling in the upper water column. This was necessary since we do not explicitly model the dissolved organic nitrogen pool. Slow sinking small detritus (SD) consists of the nonliving fraction of PS, PL, and ZS, and ZS egestion. Fast sinking large detritus (LD) consists of both nonliving fraction and egestion of ZL. Both detritus decompose to ammonium. Nitrogen limitation is described by a Michaelis-Menten function, and light limitation according to the formulation of Platt *et al*. (1980). Grazing terms use a Holling type III formulation. All biological rates are temperature dependent. The main biological parameters and their values are given in Table 2.1.

The open boundary condition is Flather for the barotropic velocity (Flather, 1976), Chapman for the free surface (Chapman, 1985), and a combination of Radiation and Nudging for the baroclinic velocity and passive and biological tracers (Marchesiello *et al*., 2001). The open boundary nudging timescale is 1 day for the incoming signal and 1 year for the outgoing signal. A third order upstream scheme and a fourth order Akima scheme are used for horizontal and vertical momentum advection, respectively. Horizontal viscosity and diffusivity are set to 7 m s^{-2} increasing gradually to 30 m s^{-2} in a 100 km width sponge layer at the open boundaries to minimize signal reflection problems. Mellor and Yamada 2.5-level closure scheme is used for vertical turbulence (Galperin *et al*., 1988).

Initial and open boundary temperature, salinity and velocities for the physical model are from the Simple Ocean Data Assimilation (SODA) model (Carton and Giese, 2008). Surface heat fluxes and wind stress are estimated using bulk parameterization. Daily water flux, air temperature, sea level pressure, humidity, shortwave radiation, and downward longwave radiation are from the European Center for Medium Range Weather Forecast (ECMWF) ERA-Interim reanalysis product (0.75° resolution, Dee *et al*., 2011), and daily surface wind fields from QuikSCAT are from the Centre d' Exploitation et de Recherche Satellitaire d' Archivage et de Traitement (CERSAT) products (0.25° resolution). Missing winds from the QuikSCAT coastal blind zone are filled with a nearest-neighbor procedure. Initial and open boundary conditions for the biological model are derived from the Ocean general circulation model For the Earth Simulator (OFES) (Masumoto *et al*., 2004). Because the OFES biological outputs include only NO_3, one phytoplankton, and one zooplankton, we partitioned the OFES fields into our model components as follows: 70% (30%) of the phytoplankton is diatom (small phytoplankton); 40% (60%) of the zooplankton is microzooplankton (mesozooplankton); NH_4 is 10% of the phytoplankton biomass, and is subtracted from the OFES NO_3 pool. Large and small detritus concentrations are assumed to be 10% each of the phytoplankton

biomass, and are subtracted from the NO_3 pool. OFES results are available only until 2006; for modeling 2007-2008 we prescribe the biological boundary conditions based on climatological values from OFES. A 1-year spin-up was done using 2002, after which the model was run until 2008, with averaged daily fields saved.

The physical-biological model reproduces reasonably well the mean state and seasonal variability of temperature, mixed layer depth, sea surface height, and phytoplankton. A validation of the model is presented in Appendix A.

2.3.3. Time series analysis

Time series of meridional wind stress (MWS), satellite and model SST, satellite chlorophyll (CHL), and surface model phytoplankton (PHY, diatom plus small phytoplankton) were examined over an 80-km wide coastal region, between 34° and 41°S (Fig. 2.1). A band-pass Lanczos filter (Duchon, 1979) was applied to those time series to isolate the subseasonal variability, using cut-off periods of 5 and 130 days [5-130d]. This subseasonal variability was characterized using procedures similar to those of Goubanova *et al*. (2013). For each coastal field (MWS, SST, CHL, and PHY), the dominant spatial and temporal patterns of the [5-130d] filtered time series were extracted with Empirical Orthogonal Function (EOF) decomposition (von Storch and Zwiers, 1999). Normalized Wavelet Power Spectrum climatologies of the first Principal Component (PC1) time series were estimated with the Morlet wavelet, using a scale resolution of 1/15 (Torrence and Compo, 1988; Liu *et al*., 2007). The PC1 time series were band-pass filtered (Lanczos) over the 30-to-80 day ([30-80d]) band to isolate the dominant intraseasonal variability. The temporal phasing between the [30-80d] filtered PC1 (*f*PC1) time series was examined with lagged correlation analysis. Correlation significance was estimated with the modified Chelton method to account for time series autocorrelation (Pyper and Peterman, 1998).

2.4. Subseasonal variability

The first EOF (EOF1) modes explain 83, 58, and 23% of the satellite MWS, SST, and CHL variability, and 51 and 32% of the model SST and PHY, respectively. EOF1 in all those fields reflects the alongshore coherence of the pattern (Fig. 2.2a-e). The following specific features can be distinguished: 1) MWS has the highest anomalies between 36.5 and 39°S, with a maximum (~0.1 N m^{-2}) near Point Lavapie (PL, 37.2°S); 2) satellite SST has the highest near-shore anomalies south of PL (~0.8°C); a jet-like structure extending northward detaches from PL; 3) model SST shows higher near-shore anomalies (~1.2°C) and cross-shore gradients than satellite SST; the largest differences between satellite and model SST occur north of PL; 4) satellite CHL has anomalies >0.8 mg m^{-3} at several shelf locations, most notably at 36-37.2°S, where the CHL anomalies exceed 1.7 mg m^{-3}; 5) model PHY closely reproduces the location of the large shelf CHL anomalies, with maximum PHY anomalies near 2.0 mmol N m^{-3}. Assuming a constant chlorophyll-to-nitrogen ratio (CHL:N) of 1 (mg chlorophyll)(mmol nitrogen)$^{-1}$, which is typical of CHL:N ratios in coastal upwelling regions (e.g. Li *et al*., 2010), we find that CHL has a weaker EOF1 pattern than PHY on most of the shelf. While the model may overestimate near-shore variability in SST and PHY, smoothing of the satellite variability by the DINEOF interpolation contributes also to the differences, since between 65 and 50% of missing observations in the satellite time series are due to cloud coverage. In addition, the comparison between CHL and PHY can be affected by changes in CHL:N, which varies both across-shore and temporally (Geider *et al*., 1997; Li *et al*., 2010). Moreover, unknown amount of colored dissolved organic matter could add bias to the satellite chlorophyll observations (Saldias *et al*., 2012). The second EOF (EOF2) explains 13, 16, and 9% of the satellite MWS, SST, and CHL variability, and 14 and 10% of the model SST and PHY. This EOF2 mode represents a meridional dipole with zero amplitude near Point Lavapie (Fig. 2.2f-j).

The time-frequency patterns from the PC1 time series, described by the annual climatology of the Normalized Wavelet Power Spectrum (NWPS), reveal seasonal changes in the subseasonal mode of the satellite and modeled fields (Fig. 2.3). The highest variability in MWS occurs in fall-winter, and least in spring-summer (Fig. 2.3a). Most of the MWS variability is at periods shorter than 20 days; the weak signal in the intraseasonal band, centered near 40 days in spring-summer and 48 days in winter is not statistically significant. Conversely, the spectrum of satellite SST shows large variability in spring-summer and small in fall-winter (Fig. 2.3b). Smaller secondary peaks are present in the submonthly band (at 20-25 days and below 16 days) during summer. The NWPS of CHL (Fig. 2.3c) also has maximum intraseasonal variance in spring-summer and is similar to the satellite SST in its pattern. The model SST and PHY power spectra (Fig. 2.3d-e) reproduce the main spectral features of satellite SST and CHL, i.e. weak variability in fall-winter, large in spring-summer, with a maximum over the [30-80d] band. Overall, the wavelet analysis reveals that seasonal changes in subseasonal variance of SST (satellite/modeled) and surface phytoplankton biomass (CHL/PHY) are not related to those of wind stress. On the other hand, the similar spectral features of SST and phytoplankton suggest that a common underlying process is modulating their 30-80 day intraseasonal variability.

2.5. Variability over the 30-to-80 day band

The *f*PC1 of SST and CHL have between 3 and 5 oscillations during spring-summer, the largest ones occurring in Dec-Jan (Fig. 2.4). Cold (warm) SST and high (low) CHL periods are linked to equatorward (poleward) MWS. The lagged correlation analysis indicates that in spring-summer MWS leads the satellite SST and CHL by 5 and 3 days, respectively (Table 2.2). The correlation between SST/CHL and MWS is weak but still significant in fall-winter, with MWS leading the satellite SST and CHL by 7 and 1 day, respectively (Table 2.2). That CHL leads satellite SST is odd for a coastal upwelling dynamic, as we would expect that wind-driven changes in SST lead the changes in CHL.

This inconsistency in the lag might be associated with interpolation error, which can preclude a finer estimation of the phase relationship with the Modis-derived time series. The model SST reproduces well the [30-80d] signal from the satellite SST (r = 0.93, model SST lags the satellite SST by 1 day) (Fig. 2.4c). Likewise, the model PHY reproduces the [30-80d] signal of satellite CHL (r = 0.71, PHY lags CHL by 3 days), although the coherence between those time series decreases in early spring (Fig. 2.4d). MWS is more highly correlated with the modeled variables than the satellite variables (Table 2.2). In spring-summer, MWS leads the model SST (PHY) by 3 (6) days, and SST leads PHY by 3 days. From the previous *f*PC1s time series analysis, we infer that the spatial EOF1 modes of SST and CHL/PHY represent the spatial signature of wind-driven upwelling and the associated phytoplankton response.

The *f*PC1 time series also show an important interannual variability. The weakest spring-summer intraseasonal oscillations occur in 2010/2011, and the strongest in 2005/2006 and 2006/2007. Considering that in these last two seasons the amplitude in the *f*PC1 anomalies is close to 2, and that for each field the spatiotemporal anomalies are obtained multiplying *f*PC1 by EOF1, the corresponding maximum spring-summer anomalies over the shelf are around 1.7°C in satellite SST, 2.4°C in model SST, 5.4 mg m^{-3} in CHL, and 5.5 mmol N m^{-3} in PHY.

Time series of MWS, satellite SST and CHL, and model SST and PHY, zonally averaged over the 80 km wide coastal region, and [30-80d] filtered, are shown in the time-latitude diagrams of Figure 2.5. The strong [30-80d] signal in spring-summer has amplitudes of ca. 1.5°C in SST (model and satellite), 2 mg m^{-3} in satellite CHL, and 3 mmol N m^{-3} in model PHY. Winter patterns are much weaker. Most of the [30-80d] band fluctuations extend along the entire region, consistent with the meridional coherence in EOF1 modes. However, an alongshore progression of anomalies is evident for several periods, especially in the CHL and PHY fields. A lagged correlation analysis between the time series and the associated *f*PC1 for spring-summer shows maximum correlation at negative

lags north of Point Lavapie (~37°S), and positive lags south of it (Fig. 2.5, right panels). The latitudinal shift in the sign of the lags suggests a poleward progression for MWS, SST, CHL, and PHY, possibly linked to the meridional dipole of the second EOF mode. Indeed, a lagged correlation analysis between the *f*PC1s and time series reconstructed from the first two EOF modes reveals a corresponding latitudinal shift in lags (not shown). To investigate processes responsible for the poleward progression in coastal upwelling and phytoplankton biomass, we perform a lagged composite analysis of the mean [30-80d] filtered anomalies of wind stress and surface phytoplankton, based on the 21 intraseasonal PHY-*f*PC1 peaks higher than 0.7, threshold equivalent to 1 std. dev. of *f*PC1 (Fig. 2.4). The composite at 0 d lags represents the average anomaly at the PHY-*f*PC1 peak, whereas for lags of –n (+n) days, the composite represents the average anomaly n days before (after) the PHY-*f*PC1 peak. We used model PHY instead of satellite CHL for this analysis to avoid the anomalous phase error of SST and CHL seen in the correlation analysis. However, the composites based on satellite CHL produced similar patterns. The wind stress composites show a poleward anomaly progression (Fig. 2.6), consistent with the pattern identified in the time-latitude diagrams. The strongest positive MWS anomalies (>0.03 N m^{-2}) occur during the two weeks preceding the PHY-*f*PC1 peak, with a main core centered at 74°-76°W. Similar spatial structure and magnitude are observed for the negative MWS anomalies that dominate the region for two weeks after the PHY-*f*PC1 peak. Consistent with a wind-driven dynamic, the peak positive (negative) anomalies in the phytoplankton composite (depicted by green (orange) contours in Fig. 2.6) lag the equatorward (poleward) anomalies in MWS by about 1 week.

2.6. Vertical changes

Surface temperature and CHL/phytoplankton biomass showed strong intraseasonal variability significantly correlated with meridional wind stress. We use the physical-biological model to examine the impact of intraseasonal wind oscillations on the vertical distribution and biomass of plankton trophic levels. We focus on a vertical section across

the shelf at 39°S during Nov-Dec, where strong intraseasonal variability in satellite CHL and model PHY is observed. In the following analyses the model outputs were band pass filtered, using a cut-off frequency of 1/30 day^{-1} to eliminate the submonthly variability.

During an intraseasonal oscillation in November-December of 2004 (Fig. 2.7) a strong equatorward jet is located at about 40 km offshore (maximum velocity ~0.6 m s^{-1}), whereas a weak one is observed near the coast. On November 9th (Fig. 2.7a), the 5 mmol N m^{-3} NO_3 contour outcrops to the surface, indicating strong coastal upwelling driven by the energetic wind burst of early November. The highest diatom and mesozooplankton concentrations occur close to the surface, with zonal diatom maxima onshore of the coastal and 40 km offshore jets. On November 24th (Fig. 2.7b), the near-shore NO_3 exceeds 10 mmol N m^{-3} and surface diatom is reaching a peak (>6 mmol N m^{-3}). The mesozooplankton maximum is offshore of the diatom maximum. On December 9th (Fig. 2.7c), when the MWS approaches its minimum, coastal upwelling is weak and solar heating enhances the vertical density stratification (not shown). NO_3 decreases below 5 mmol N m^{-3} within the upper mixed layer, and a subsurface phytoplankton maximum (SSPM) develops around 22 m, exhibiting high concentration of diatom and mesozooplankton (maximum of 6 and 2 mmol N m^{-3}, respectively). In the mixed layer, mesozooplankton concentration exceeds the diatom concentration. On December 24th (Fig. 2.7d), the stratified condition persists, and the SSPM deepens slightly. Diatom concentration in the SSPM decreases 50%, whereas the mesozooplankton remains relatively stable. At this time, the diatom concentration within the upper mixed layer is the smallest (<0.2 mmol N m^{-3}). The stratified condition is disturbed by another strong wind pulse in late January 2005 (not shown), which reinforces the coastal upwelling, cools the upper layer, reduces the vertical stratification, and establishes conditions similar to early November.

Vertical changes in the modeled ecological fields during three strong intraseasonal wind oscillations in spring-summer 2004-2005 are illustrated in a time varying vertical profile

from a station 30 km offshore at 39°S (Fig. 2.8). The two modeled phytoplankton components (Fig. 2.8c-d) responded differently to the wind oscillations (Fig. 2.8a). Diatoms grow rapidly as the wind-driven NO_3 increases (not shown), reaching a maximum concentration ~10 days after the wind peak. A subsurface diatom maximum develops ~15 days after the wind peak, linked to low wind condition, when temperature vertical stratification is increasing (Fig. 2.8b). On the other hand, small phytoplankton show little enhancement during the diatom maximum, but peak subsurface later when vertical stratification is the strongest. Diatom contributions to the total phytoplankton concentration varies from ~95% during the diatom peaks to ~60% during the diatom minima. Zooplankton responds to the changes in phytoplankton concentration and distribution (Fig. 2.8e-f). The microzooplankton maxima lag the small phytoplankton maxima, and reflect microzooplankton grazing reducing the subsurface peak of flagellates. The mesozooplankton maxima lag the diatom peak by 2-3 weeks. Both zooplankton components have subsurface maxima during low wind conditions when phytoplankton has subsurface maxima. The mesozooplankton contribution to total zooplankton biomass ranges from ~78 to 62%. Similar variability in plankton biomass occurs in spring-summer from other years (not shown).

2.7. Discussion

Unlike previous studies on intraseasonal satellite microwave SST variability (Renault *et al*., 2009; Dewitte *et al*., 2011; Goubanova *et al*., 2013; Illig *et al*., 2014), we examined SST and chlorophyll variability using MODIS passive satellite sensors. This allowed resolving the coastal region over a narrow continental shelf, but with potential uncertainty due to DINEOF averaging in space and time to estimate missing data. Because relatively few satellite data gaps exceeded 4 days, we think the tradeoff had a minor effect on the data used. Moreover, we complemented the satellite data with model-derived estimates of SST and phytoplankton for the analysis. Satellite data noise due to cloud coverage might explain part of the differences between EOF patterns derived from MODIS and model

outputs. In addition, bias in the wind forcing that drives the numerical model could contribute to those differences near-shore. Because QuickSCAT winds are not resolved within 50 km of the coast, the near-shore cross-shelf coastal wind may be inaccurate, possibly resulting in overestimation of coastal upwelling (Renault *et al*., 2012). High-resolution wind products that properly resolve the coastal region are required to better represent coastal upwelling dynamics. The lack of river discharges in the model could affect density stratification near-shore, especially in winter and early spring, and might impact phytoplankton production. That might explain part of the PHY-CHL disagreement in the NWPS during early spring. Despite these uncertainties, we obtained consistent and similar patterns of intraseasonal variability from two sources: satellite data and model outputs. This redundancy provides added confidence that our intraseasonal analysis of upwelling dynamics off central Chile is robust.

2.7.1. Intraseasonal response of SST and phytoplankton

The wavelet power spectrum patterns of wind stress and SST off central Chile resemble patterns reported previously for other eastern boundary current regions off Namibia and Peru (Goubanova *et al*. 2013; Illig *et al*., 2014). In those regions and Chile (this study) the strong intraseasonal spectral peaks of SST are not linked to similar intraseasonal peaks in the wind stress. The maximum SST intraseasonal variability occurs in spring-summer, when the MWS variability is the smallest. Goubanova *et al*. (2013) link the seasonal changes in the intraseasonal SST signal to changes in the vertical temperature gradient. A strong (weak) near surface temperature gradient, associated with a shallow (deep) mixed layer depth, favors strong (weak) wind-driven disturbances in SST during spring-summer (winter). The variability in SST and mixed layer depth (MLD) off central Chile are consistent with that mechanism. Disturbances in the vertical temperature gradient would explain also the strong MWS-SST correlation in spring-summer, a feature previously reported off central Chile by Renault *et al*. (2009). In addition, we document similar intraseasonal signals in surface phytoplankton biomass, measured as satellite

chlorophyll and modeled phytoplankton. The winter-to-summer differences in the intraseasonal phytoplankton biomass signal can be explained by the seasonal changes in ocean stratification and light. Vertical temperature stratification controls the availability of light and nutrients for phytoplankton, so a deeper MLD in winter, along with reduced solar radiation, imposes light-limitation on phytoplankton growth. In fact, light limitation due to changes in stratification explains the seasonal cycle in coastal phytoplankton off Peru (Echevin *et al.*, 2008). A stronger light limitation could be expected off central Chile, as the seasonal change in shortwave radiation increases with latitude. In addition, a deeper nutricline in winter, as a result of the prevailing downwelling to weak upwelling seasonal condition off central Chile, reduces the ability of an equatorward wind burst to fertilize the photic layer. All those factors (stratification, light, nutricline depth) will reduce the response of phytoplankton to intraseasonal MWS variability during winter.

To visualize the underlying dynamics leading to the seasonal modulation of SST and phytoplankton biomass at the intraseasonal band, low pass filtered time series of MWS, surface short wave radiation, MLD, the 5-50 m vertical temperature gradient (dT/dz), and NO_3 concentration at 5 and 50 m depth, derived from the numerical model, are plotted for a location 30 km offshore at 39°S (Fig. 2.9). The 5 m depth represents the near-surface condition, whereas the 50 m depth represents a point below the seasonal thermocline. The MWS time series shows a strong seasonal cycle, with equatorward wind stress dominating during spring-summer, and poleward winds occurring during fall-winter. Strong intraseasonal MWS anomalies are observed year round. The MLD is approximately 20 m in spring-summer and 40 m in fall-winter, being well correlated to dT/dz, which has maximum values (~6°C) in summer and minimum (<1°C) in winter. Subsurface NO_3 (NO_3 at 50 m depth, NO_3[50m]) has a strong seasonal cycle, with a minimum in winter (10 mmol N m^{-3}) and maximum in summer-fall (30 mmol N m^{-3}). Low NO_3[50m] periods are associated with poleward MWS anomalies. An intraseasonal NO_3[50m] signal, modulated by MWS, is evident, especially in winter. Maximum surface NO_3 values (NO_3[5m]) occur in fall and winter, indicating potential light limitation of

phytoplankton growth during winter. Peak surface NO_3 in fall is associated with cooling of the upper layer (e.g., seasonal negative trend in dT/dz and SST) and strong equatorward MWS intraseasonal anomalies. The model phytoplankton responds strongly to the MWS intraseasonal anomalies only in spring-summer, when the wind disturbances of a seasonally enhanced vertical stratification are concurrent with high solar radiation.

The main processes controlling the SST and phytoplankton variability are coastal upwelling and ocean mixing, disturbing the vertical stratification of temperature and NO_3. Counteracting those mechanisms is solar heating. Both Ekman divergence near the coast and cyclonic wind stress curl contribute to upwelling over the shelf, as the wind stress pattern of Figure 2.6 shows: when the positive (negative) MWS anomalies are the strongest, a sharp negative (positive) zonal gradient of MWS occurs near the coast, determining cyclonic (anticyclonic) wind stress curl. In spring-summer, satellite SST (CHL) lags MWS by 5 (3) days, whereas modeled SST (PHY) lags MWS by 3 (6) days. Discrepancies between correlation lags derived from satellite products and model outputs might be explained by the process used to estimate missing satellite observations due to cloudiness. The MWS-SST lags are smaller than the lags determined from the 60-day intraseasonal oscillations in the Benguela (7 days) and Peru (8 days) upwelling regions (Goubanova *et al.*, 2013; Illig *et al.*, 2014). This difference in lags might be explained by the shorter intraseasonal oscillations (~50 days) off central Chile, although regional differences in the processes controlling temperature might also contribute. Our MWS-PHY lag is similar to the one obtained by Bane *et al*. (2007) off Oregon (7.4 days), while they obtained a much longer lag between wind stress and satellite chlorophyll (13.6 days).

2.7.2. MJO and intraseasonal variability

Intraseasonal upwelling variability off central Chile has been associated with atmospheric disturbances linked to Madden-Julian Oscillation (MJO) (Hormazabal *et al*., 2002; Rutllant *et al*., 2004), although the underlying mechanisms have not been clarified. By

performing a composite analysis based on the Wheeler and Hendon (2004) MJO index phases, Rahn (2012) found significant equatorward (positive) wind (sea level pressure, SLP) anomalies off central Chile associated with MJO phases 4-5-6, and poleward (negative) wind (SLP) anomalies during phases 7-8-1, suggesting modulation of the synoptic wind variability by the MJO. Those phases are linked to deep convection over Indonesia and the central-Pacific, respectively. In agreement with the Rahn (2012) findings, we found that the MJO phases 4-5 (8-1) dominated during the two weeks preceding the intraseasonal phytoplankton maximum (minimum) (not shown). To examine the connection between MJO and coastal phytoplankton production, we estimated the mean composites of SLP and 200-hPa geopotential height (200-gph) based on i) MJO phases 4-5 and 8-1, and ii) the periods preceding the PHY maxima/minima, referred to as high/low PHY composites. To account for the response lag between MWS and PHY, the selected high/low PHY composite periods extend from 15 to 5 day before the strongest maxima/minima in the *f*PC1 time series (Fig. 2.4d). The SLP and 200-gph from the high (low) PHY and MJO 4-5 (8-1) composites show similar spatial patterns (Fig. 2.10a-d). The presence of anticyclonic SLP anomalies off southern Chile leads to an increase in the meridional SLP gradient along the Chilean coast, which is linked to strong equatorward wind and atmospheric coastal jet activity off central-Chile (Garreaud and Falvey, 2009; Renault *et al*., 2009; 2012).

The SLP and 200-gph patterns shown in Figure 2.10a [2.10b] resemble the patterns described by Montecinos and Aceituno (2003) for spring of El Niño [La Niña] periods. They suggested that an equatorward [poleward] shift of the mid-latitude storm track, due to increased [decreased] blocking at high latitudes acts to decrease [increase] coastal upwelling and phytoplankton production in spring-summer. Thus, during the low (high) PHY periods, positive (negative) zonal wind anomalies dominate in the subtropical region, and negative (positive) zonal wind anomalies in the Westerlies region (Fig. 2.10e-f). Similar patterns are observed for the composites based on MJO phases 8-1 (4-5) (not shown). The relationship between the atmospheric disturbances and MJO might be linked

to the Pacific-South America (PSA) teleconnection pattern (Ghil and Mo, 1991). The PSA is an eastward propagating atmospheric wave train, triggered by anomalous deep convection over the equatorial Pacific. This teleconnection pattern has been related with blocking activity at high latitude and the strength of the South Pacific Subtropical Anticyclone (Rutllant and Fuenzalida, 1991; Montecinos and Aceituno, 2003; Rutllant *et al*., 2004).

Previous studies have documented the impact of equatorial originating disturbances and coastal upwelling in the HCS. Dewitte *et al.* (2011) suggested that the intraseasonal SST variability off Peru could be linked to mid-latitude atmospheric disturbances triggered by MJO, and coastal-trapped waves (CTWs) driven by equatorial Kelvin waves. Using a realistically forced numerical model, Illig *et al*. (2014) showed that equatorially originating CTWs explain only a small fraction (~20%) of the intraseasonal SST variability off Peru. However, Echevin *et al*. (2014) showed a significant impact of CTWs on phytoplankton production, but mostly in coastal regions at lower latitudes (4°-14°S). An idealized modeling study off central Chile indicated significant impacts of CTWs on coastal upwelling, which was not corroborated by in-situ evidence (Leth and Middleton, 2006). Our findings using satellite and model fields strongly indicate that local wind variability is the main driver of the intraseasonal SST and phytoplankton patterns off central Chile during 2003-2011. The similar patterns shown in Figure 2.10 suggest that these winds may be modulated by MJO atmospheric disturbances at high latitude. Further studies are required to understand better the mechanisms of that teleconnection.

2.7.3 Impacts on higher trophic levels

Intraseasonal wind variability, by creating periods with alternating high and low phytoplankton abundance, could impact higher trophic levels, including commercially important small pelagic fish such as common sardine (*Strangomera bentincki*) and

anchovy (*Engraulis ringens*). Because both species have extended, multi-month spawning seasons, the survival of early life stages may be affected by the spatiotemporal coupling/uncoupling between feeding larvae and the wind-driven larval prey availability (abundance and type). The timing of the first strong intraseasonal peak of phytoplankton biomass during spring (seen in the *f*PC1 time series of PHY and CHL) varies from September to early November interannually (Fig. 2.4d), and might impact annual recruitment of common sardine, which is linked to spring phytoplankton production (Gomez *et al*., 2012). In addition, wind-driven changes in the upper layer temperature will affect biological rates, modulating egg and larval development durations. Finally, the intraseasonal wind variability could have a significant impact on dispersal and connectivity patterns between sites of adult spawning and sites of juvenile recruitment. These potential impacts suggest that intraseasonal upwelling variability should be considered when examining the dynamics of higher trophic levels.

2.8. Concluding remarks

Satellite observed SST and CHL, as well as modeled SST and surface phytoplankton display a strong intraseasonal variability off central Chile in spring-summer, and weak in fall-winter. Between 3 and 5 strong intraseasonal oscillations in SST and coastal production occur every year during spring-summer, with an average duration of roughly 50 days. Although wind stress does not show strong variability in the intraseasonal band, our results indicate that the intraseasonal signals in SST and phytoplankton production are driven by wind. The seasonal change in the amplitude of the intraseasonal SST is consistent with a modulation of the SST disturbances by the MLD annual cycle. Furthermore, the annual cycle of MLD, in conjunction with light, explains the seasonal change in the amplitude of the intraseasonal phytoplankton signal. Coherent with the reported link between MJO disturbances and alongshore winds off central Chile, a relationship between MJO phases and coastal phytoplankton production is suggested. Our results stress the impact of the upwelling intraseasonal variability on SST and coastal

production, which might significantly influence upper trophic levels. Further studies are required to evaluate better the underlying dynamics of the intraseasonal variability and its impacts on the coastal upwelling ecosystem.

Acknowledgements

F.G. is very grateful for the support of the Chilean National Commission for Scientific and Technological Research (CONICYT), the Fulbright Student Program, and the Graduate School of Oregon State University.

Table 2.1. Biological model parameters

Parameter	Name			Source
	Phytoplankton parameters	PS	PL	
V_{max}	Maximum photosynthetic rate at 0°C (d^{-1})	0.5	1.0	1, 2, 3, 4
k_{Gpp}	Temperature coefficient for photosynthesis $(°C)^{-1}$	0.0693	0.0693	1
α_P	Initial slope of the P-I curve (m^2 W^{-1}) d^{-1}	0.023	0.028	4, 5
β_P	Photoinhibition coefficient (m^2 W^{-1}) d^{-1}	$9*10^{-4}$	$4*10^{-4}$	4, 5
KNO_3	Half saturation constant for nitrate (mmol N m^{-3})	1.0	3.0	1
KNH_4	Half saturation constant for ammonium (mmol N m^{-3})	0.1	0.3	1
ψ_P	Ammonium inhibition coefficient (mmol N $m^{-3})^{-1}$	1.5	3.0	1, 3, 4
PMor	Mortality at 0°C (m^3 $mmolN^{-1}$ d^{-1})	0.020	0.020	*
k_{PMor}	Temperature coefficient for mortality $(°C)^{-1}$	0.0531	0.0531	1
PRes	Respiration at 0°C $(day)^{-1}$	0.03	0.03	1
k_{PRes}	Temperature coefficient for respiration $(°C)^{-1}$	0.0519	0.0519	1
AttP	Light attenuation due to phytoplankton (m^2 mmol N^{-1})	0.0095	0.0095	6
	Zooplankton parameters	ZS	ZL	
GRmPS	Maximum grazing rate at 0°C on PS (d^{-1})	0.40	0.10	1, 2, 3
GRmPL	Maximum grazing rate at 0°C on PL (d^{-1})	0.10	0.30	1, 2, 3
GRmZS	Maximum grazing rate at 0°C on ZS (d^{-1})		0.20	1, 2, 3
k_{Gra}	Temperature coefficient for grazing $(°C)^{-1}$	0.0693	0.0693	1
KPS	Zooplankton half saturation on PS (mmol N $m^{-3})^2$	0.30	0.8	*
KPL	Zooplankton half saturation on PL (mmol N $m^{-3})^2$	0.30	0.8	*
KZS	Zooplankton half saturation on ZS (mmol N $m^{-3})^2$		0.8	*
ZMor	Zooplankton mortality at 0°C (m^3 mmol N^{-1} d^{-1})	0.028	0.045	*
k_{ZMor}	Temperature coefficient for mortality $(°C)^{-1}$	0.0531	0.0531	1
α_Z	Zooplankton assimilation efficiency	0.70	0.70	1
β_Z	Zooplankton growth efficiency	0.30	0.30	1
	Other Parameters			
Nit0	Nitrification rate at 0°C (d^{-1})		0.07	1, 2
k_{Nit}	Temperature coefficient for nitrification $(°C)^{-1}$		0.0693	1
SD2NH4	Small detritus decomposition rate at 0°C (d^{-1})		0.10	1
LD2NH4	Large detritus decomposition rate at 0°C (d^{-1})		0.10	1
K_{D2NH4}	Temperature coefficient for decomposition $(°C)^{-1}$		0.0693	1
wSD	Small detritus sinking rate (m d^{-1})		8	6
wLD	Large detritus sinking rate (m d^{-1})		40	7
Attsw	Light attenuation due to seawater (m^{-1})		0.067	6

PS: small phytoplankton; PL: large phytoplankton; ZS: small zooplankton; ZL: large zooplankton. [1]Kishi *et al.* (2007); [2]Rose *et al*. (2007); [3]Yoshie *et al*. (2007); [4]Chenillat *et al.* (2013); [5]Li *et al.* (2010); [6]Spitz *et al.* (2003); [7]Fischer and Karakas (2009); *Present study.

Table 2.2. Maximum lagged correlation between the *f*PC1 time series time series of meridional wind stress (MWS), satellite and modeled SST, satellite chlorophyll (CHL), and modeled surface phytoplankton (PHY). The lag (days) at maximum correlation is indicated in parenthesis.

	All months	October-March	April-September
MWS –satellite SST	-0.68 (-5)	-0.88 (-5)	-0.54 (-7)
MWS – CHL	0.53 (-3)	0.72 (-3)	0.31 (-1)
satellite SST –CHL	-0.60 (+2)	-0.65 (+2)	-0.24 (+5)
MWS – model SST	-0.78 (-4)	-0.93 (-3)	-0.70 (-7)
MWS – PHY	0.72 (-7)	0.91 (-6)	0.51 (-8)
model SST – PHY	-0.93 (-3)	-0.95 (-3)	-0.78 (-4)

* Correlation coefficient significant at 95% level. Sample size in the significance test was obtained with the modified Chelton method to account for time series autocorrelation (Pyper and Peterman, 1998)

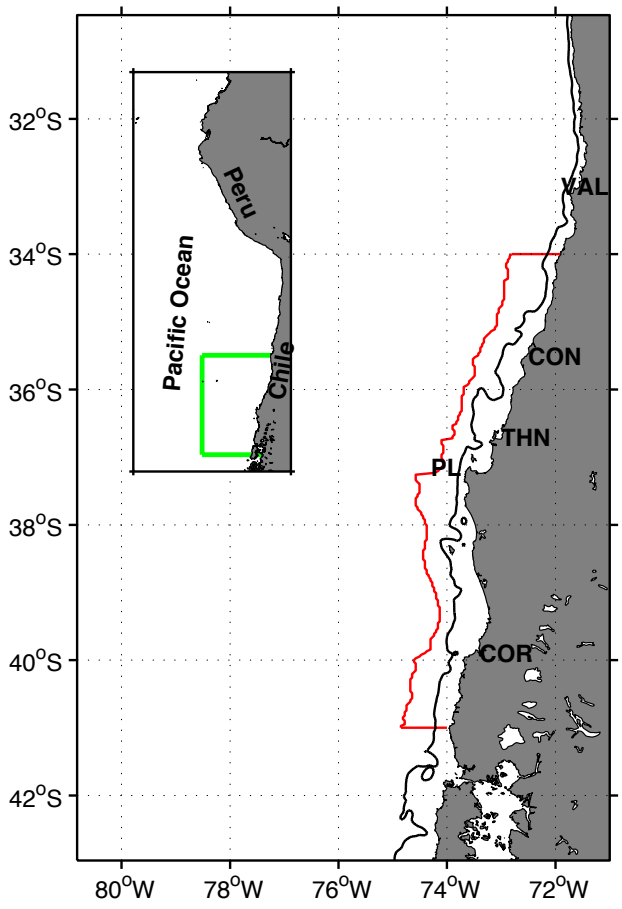

Figure 2.1. Model domain. The red contour demarks the 80 km wide coastal region from 34 to 41°S, and the black contour shows the 250 m isobath. The locations of Valparaiso (VAL), Constitucion (CON), Talcahuano (THN), Point Lavapie (PL), and Corral (COR) are shown. Inset shows the Humboldt Current System with the full model domain shown by green lines.

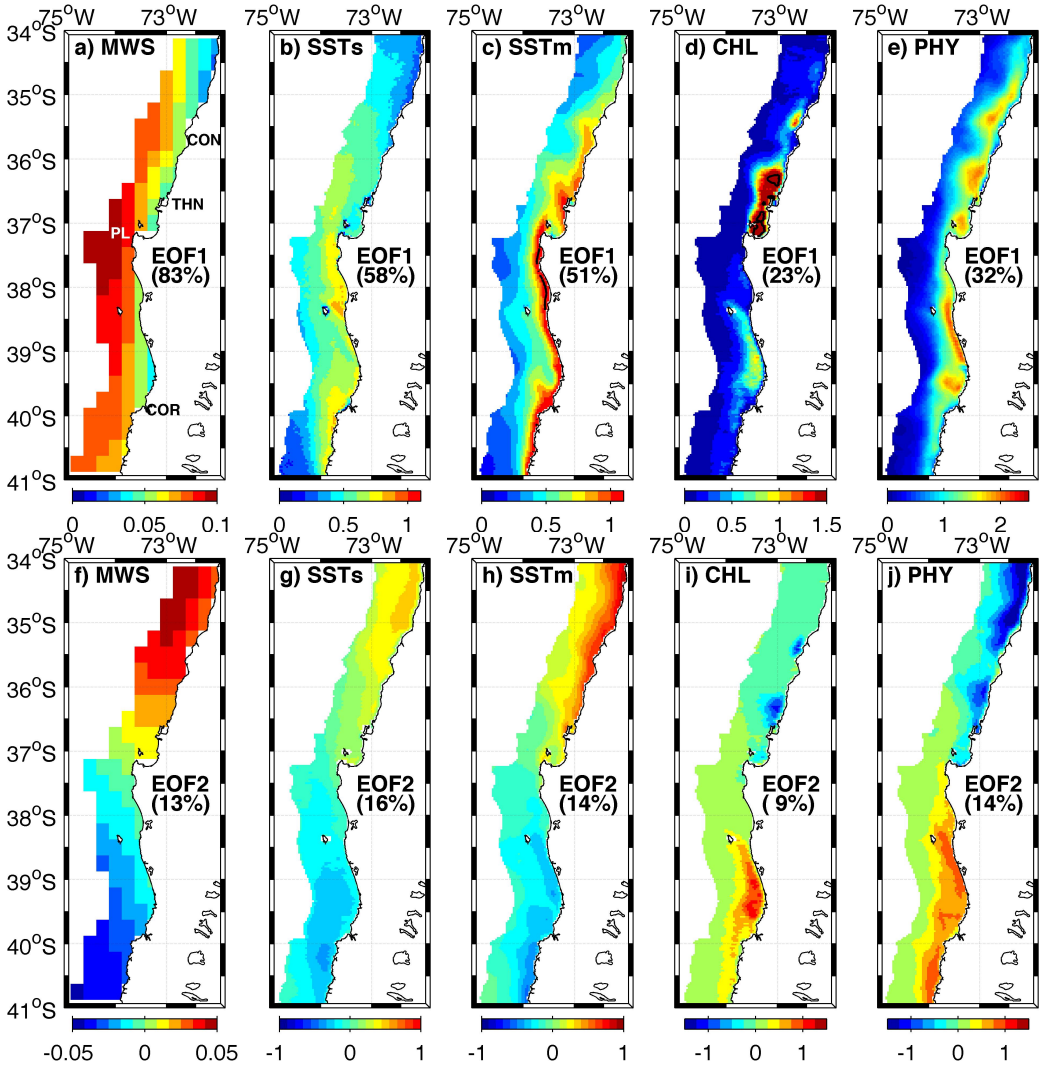

Figure 2.2. EOF analysis. First (a-e) and second (f-j) EOF modes derived from the sub-seasonal time series of the satellite Cross-Calibrated Multi-Platform meridional wind stress (MWS), satellite Modis SST (SSTs), model SST (SSTm), satellite Modis chlorophyll (CHL), and model surface phytoplankton (PHY). The EOF units of MWS, SST, CHL, and PHY are N m^{-2}, °C, mg m^{-3}, and mmol N m^{-3}, respectively. Black contours depict 1.2°C in EOF1-SSTm, and 1.7 mg m^{-3} in EOF1-CHL. Panel a) shows locations of Constitucion (CON), Talcahuano (THN), Point Lavapie (PL), and Corral (COR).

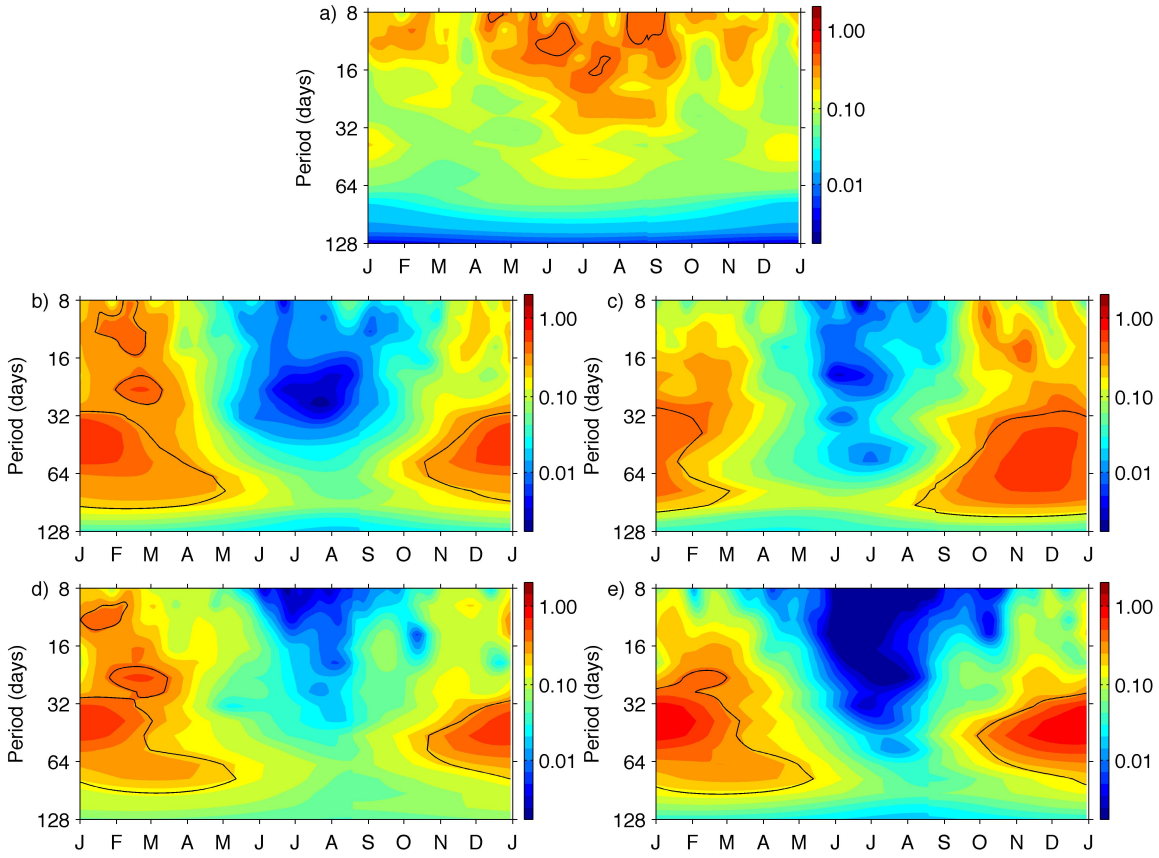

Figure 2.3. Climatology of the Normalized Wavelet Power Spectrum (NWPS) of the first EOF mode time series of a) satellite Cross-Calibrated Multi-Platform MWS, b) MODIS satellite SST, c) MODIS satellite CHL, d) ROMS model SST, and e) ROMS model surface phytoplankton concentration. Black contours depict the 95% significance level.

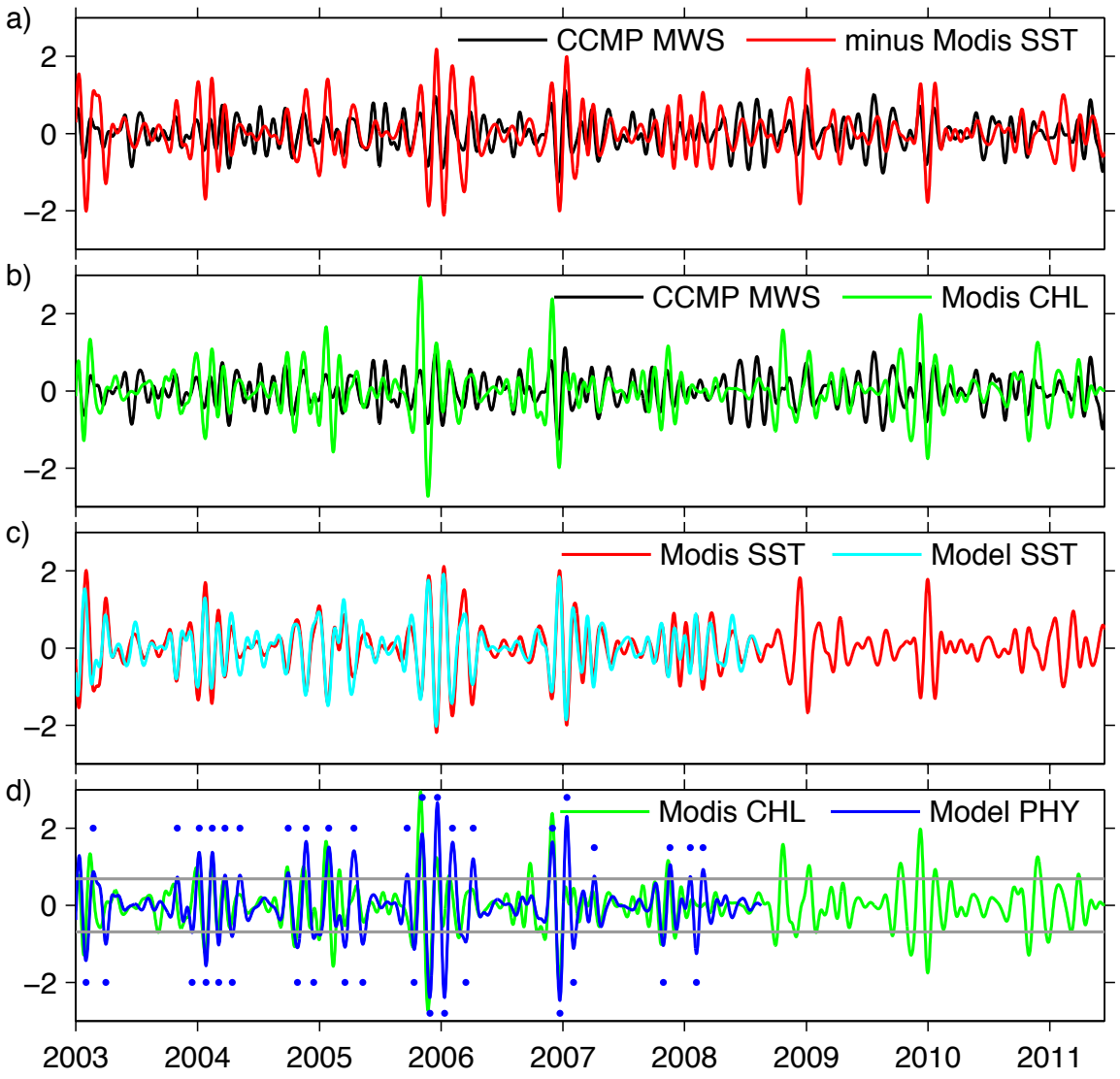

Figure 2.4. 30-to-80 day band-pass filtered PC1 time series (*f*PC1s) from the satellite meridional wind stress (MWS), satellite SST, satellite chlorophyll-a, model SST, and model surface phytoplankton (PHY). Blue dots in panel d indicate the PHY peaks higher or lower than 0.7 (gray line) that were selected for the composite analyses (describe in text). Note that the model derived PCs end in 2008. Tics on the ordinate mark January 1st of each year.

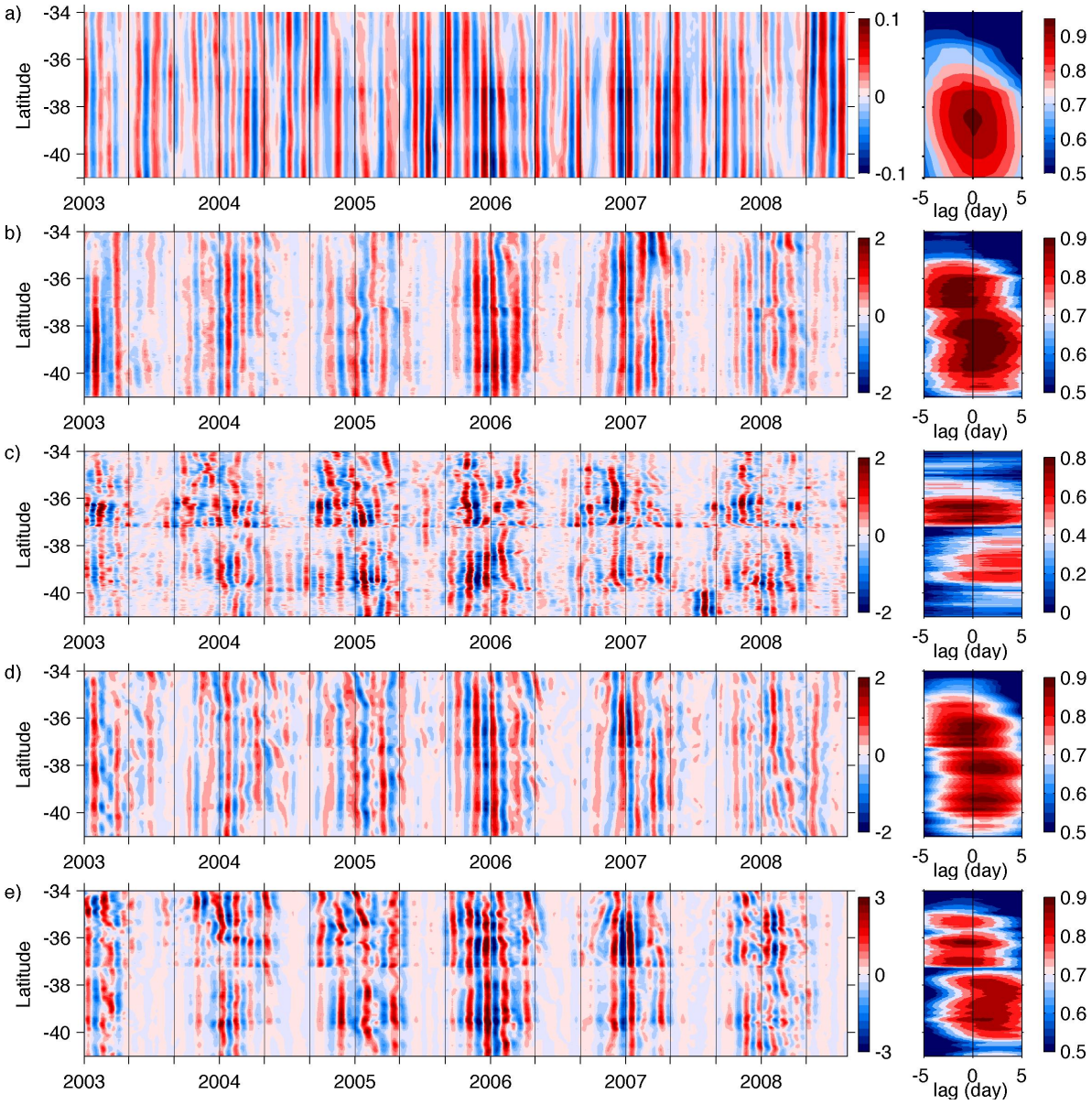

Figure 2.5. Left panels: 30-to-80 day variability from zonally averaged (coast to 80 km offshore; see Fig. 1) time series of satellite MWS (a), satellite SST (b), satellite CHL (c), model SST (d), and model surface phytoplankton (e). Right panels: spring-summer lagged correlation between the zonally averaged time series in left panels and the corresponding *f*PC1 time series shown in Figure 2.4.

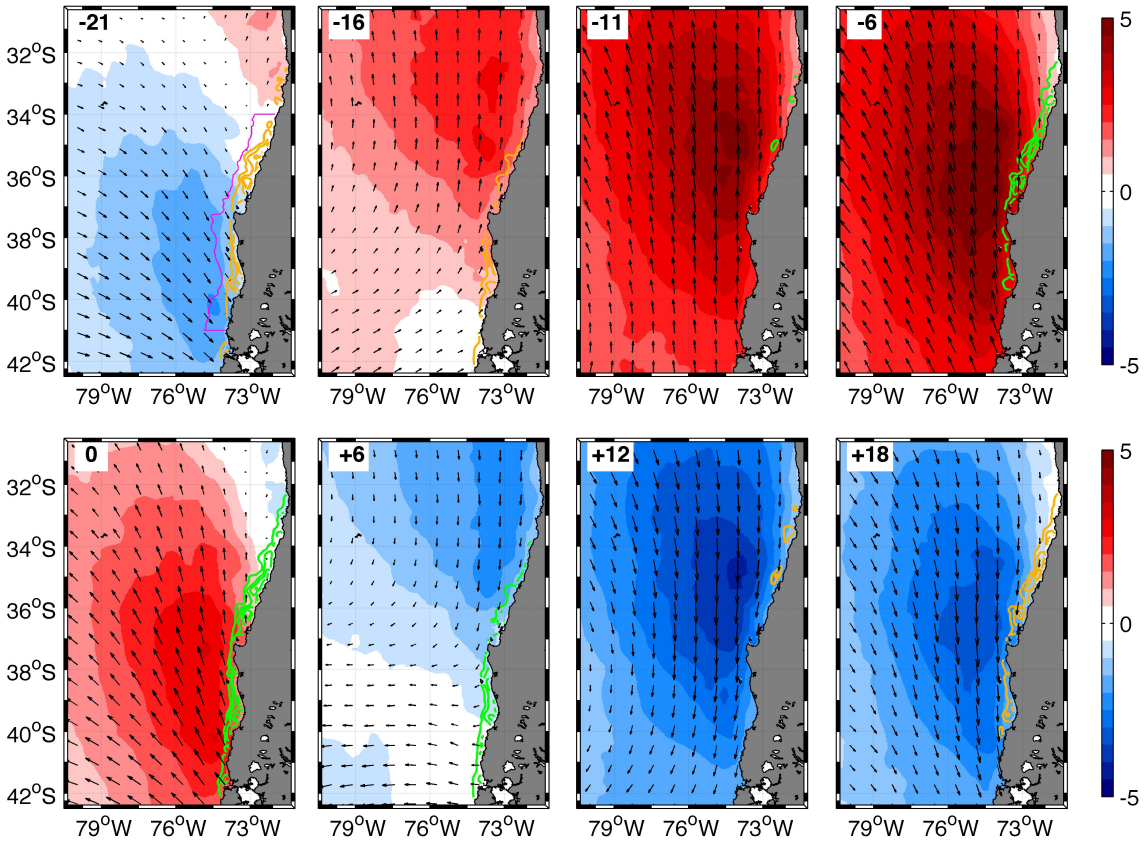

Figure 2.6. Lagged composite of the mean 30-to-80 day band anomaly of MWS and model surface phytoplankton based on the PHY-*f*PC1 time series (details in Section 4). The background colors (red-white-blue scale bars) are the MWS intraseasonal anomaly (10^{-2} N m^{-2}). Arrows correspond to the wind stress vector. The green (orange) contours depict the positive (green) and negative (orange) contours of the model phytoplankton anomaly at 0.5 mmol N m^{-3} intervals. Lag in days is indicated in the upper left corner of each panel. The magenta line in the upper left panel depicts the 80 km wide coastal region from which the PHY-*f*PC1 was obtained.

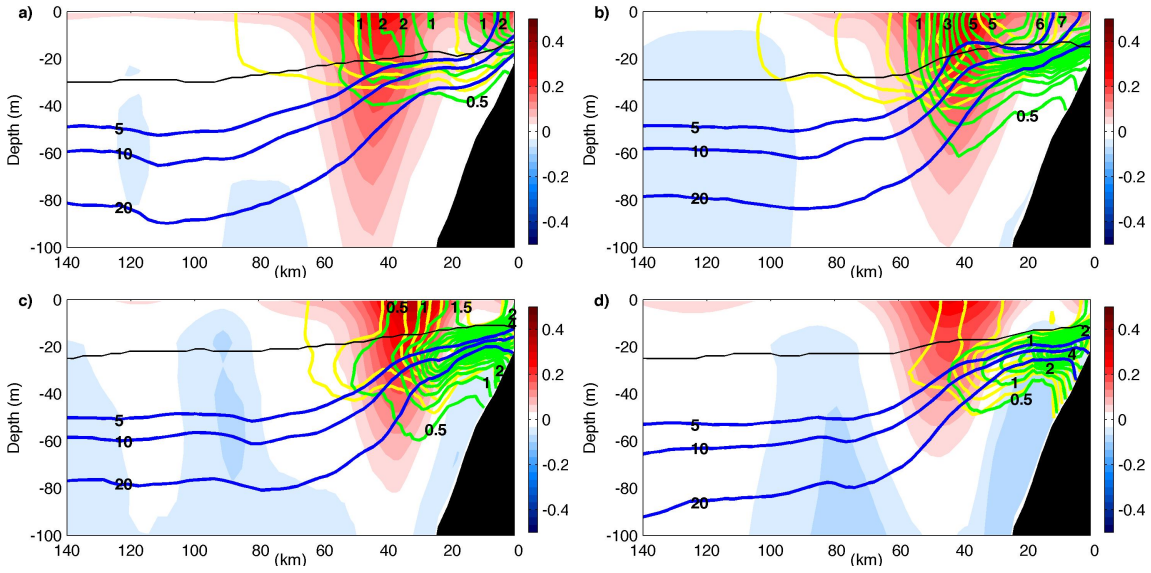

Figure 2.7. Cross-shore vertical sections at 39°S showing several fields from the coupled biophysical model during an intraseasonal oscillation in November-December 2004: Blue, green, and yellow contours correspond to NO_3, diatom, and mesozooplankton concentration, respectively; background color (red-white-blue scale) shows the meridional velocity (positive northward). Thin black line shows the mixed layer depth. Panel sequence is Nov 9th(a), Nov 24th(b), Dec 9th(c), and Dec 24th(d). Mesozooplankton contours are not labeled. Diatom (mesozooplankton) contours are every 0.5 (0.2) mmol N m^{-3} starting at 0.5 mmol N m^{-3}. Modeled fields in panels are snapshots from 30-day low-pass filtered time series.

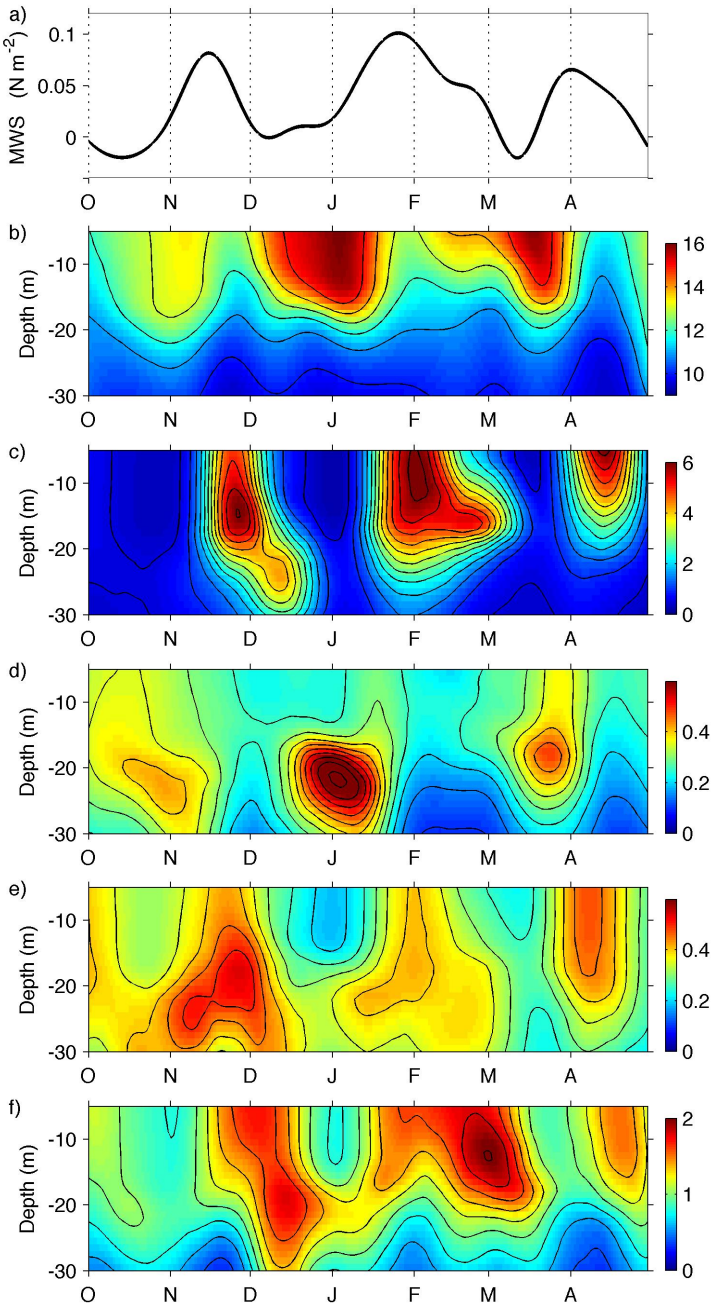

Figure 2.8. Impact of the intraseasonal wind variability on a modeled vertical plankton profile at 39°S-73.6°W during spring-summer of 2004-2005: 30-day low-pass filtered time series of a) satellite meridional wind stress, b) temperature (°C), c) diatoms, d) small phytoplankton, e) microzooplankton, and f) mesozooplankton concentration (mmol N m^{-3}). The contours in plankton fields (c-f) are every 0.5, 0.05, 0.05, and 0.2 mmol N m^{-3}, respectively.

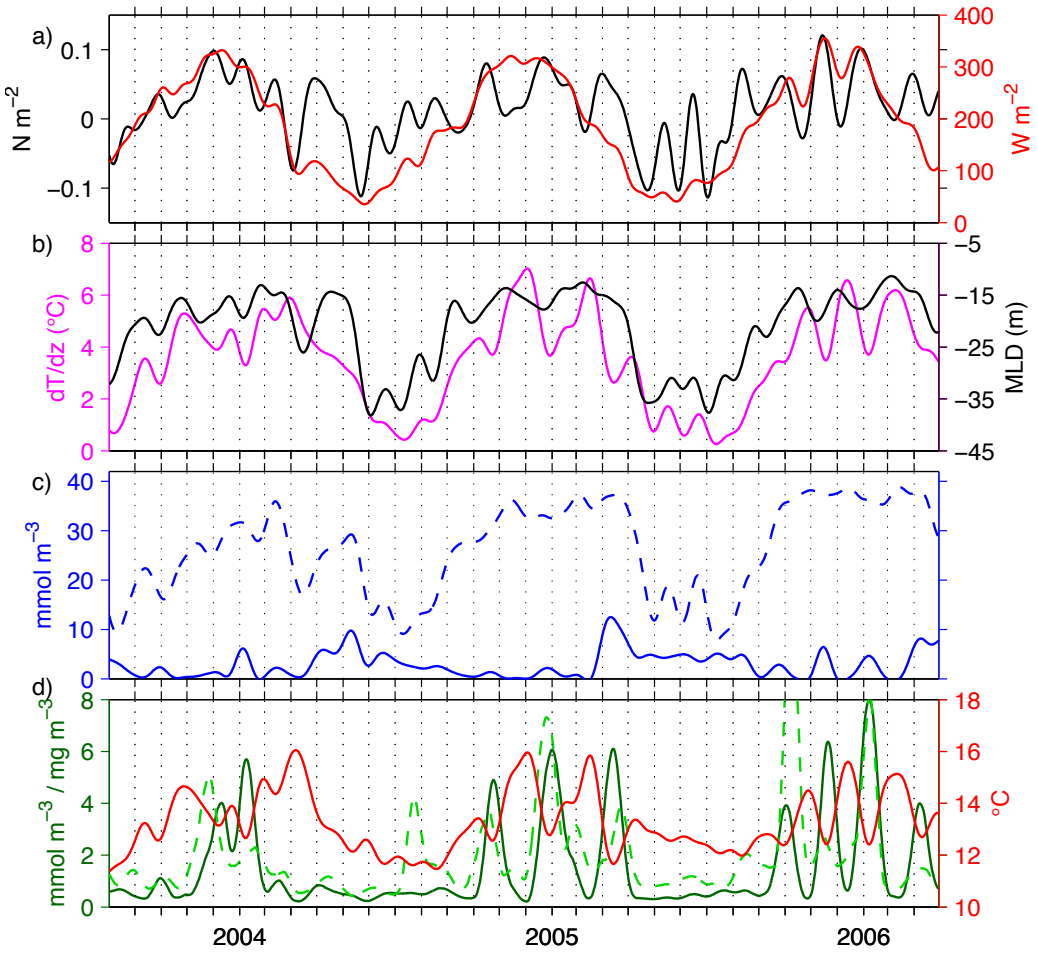

Figure 2.9. Seasonal modulation of intraseasonal variability (Jul 2003-Mar 2006): 30-day low-pass filtered time series at 39°S 73.6°W of a) Cross-Calibrated Multi-Platform meridional wind stress (black) and ERA-interim short wave radiation (red); b) Model derived series of temperature vertical gradient between 5 and 50 m depth (dT/dz; purple)) and mixing layer depth (MLD; black); c) Model derived series of NO_3 at 5 m (solid blue line) and 50 m (dashed blue line); d) Model derived series of SST (red) and phytoplankton at 5 m depth (solid green line), and satellite chlorophyll (dashed green line).

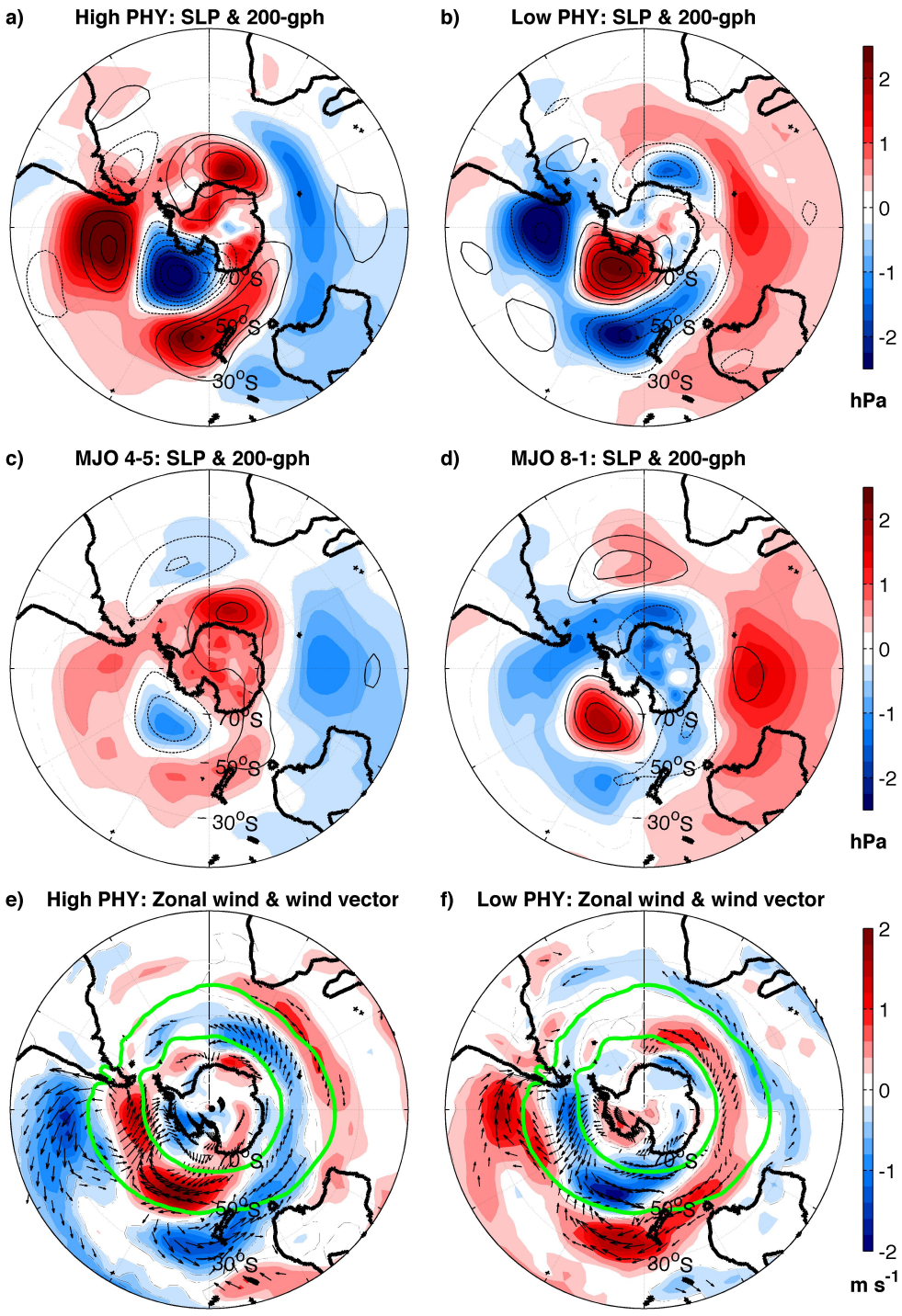

Figure 2.10. (legend on next page)

Figure 2.10 (previous page). Madden-Julian Oscillation and Intraseasonal Phytoplankton Variability: a-d) Composites of intraseasonal anomalies of SLP (background color) and 200 hPa geopotential height (solid and dash contours for positive and negative anomalies -every 10 m-, respectively) for periods preceding the PHY-*f*PC1 maxima (a) and minima (b), and for MJO phases 4-5 (c) and 8-1 (d); e-f) composites of zonal wind (background color) and wind vector (arrows, only wind anomalies >0.5 m s^{-1} plotted) for the periods preceding the PHY-*f*PC1 maxima (e) and minima (f). All composites are based on data from Oct-Mar. Green contours show the long-term position of the Westerlies belt (depicted by the 5 m s^{-1} zonal wind contours). SLP, 200-gph, and winds were obtained from NCEP-NCAR Reanalysis (Kalnay *et al*., 1996).

3. Coastal retention, prey density, and spawning strategy of anchovy and common sardine

3.1 Abstract

Ocean circulation and plankton production seasonal patterns can modulate the timing and location of spawning of marine populations. Understanding the coupling between environmental patterns and reproductive strategies is important to predict population responses to disturbances in ecosystem phenologies. Here we examined the hypothesis that spatiotemporal patterns in spawning of anchovy (*Engraulis ringens*) and common-sardine (*Strangomera bentincki*) from the southern Humboldt System promotes shelf retention and prey availability for fish early life stages. To examine this we used a particle-tracking model (PTM) coupled to an ocean circulation and lower-trophic-level model (LTLM) from 2002-2008. The model simulates the dispersal of virtual egg/larvae, recording the experienced LTLM plankton fields as proxies of prey abundance. Experiments with passive and neutrally buoyant virtual egg/larvae showed that the main spawning period (Aug-Oct) maximized the connectivity between spawning locations and nursery regions. Spawning timing was only partially linked to high retention, but the main spawning grounds, shoreward of the 100-m isobath, promoted high coastal retention year round. Experiments that incorporated ontogenetic diel vertical migration behavior enhanced coastal retention and connectivity. Virtual fish larvae experienced peaks in micro- and mesozooplankton during the main spawning period. We suggest that the Aug-Oct spawning period of small pelagic fish in the southern Humboldt System is largely explained by higher prey availability and enhanced connectivity patterns, whereas inner shelf spawning and ontogenetic vertical migration are strategies that increase ichthyoplankton retention.

Keywords: Small pelagic fish, particle-tracking, ichthyoplankton dispersal, coastal retention, spawning strategy, DVM, central-Chile, Humboldt System

3.2. Introduction

The southern Humboldt Current System (HCS), off the west coast of South America, is home to large populations of common sardine (*Strangomera bentincki*) and anchovy (*Engraulis ringens*). Like small pelagic fish from other eastern boundary upwelling systems, these intermediate trophic fish exert a strong control on the trophodynamics of the coastal ecosystem (Rice, 1995). They have high fecundity and growth rates, relatively short life span (<3 years), gregarious behavior, and recruitment dynamics strongly affected by density-independent factors (Castro *et al*., 2000; Cubillos *et al*. 2001; Cubillos and Arcos, 2002; Gomez *et al*., 2012). Common sardine and anchovy form mixed aggregations over the central Chile continental shelf (Gerlotto *et al*., 2004), and are harvested by purse-seining vessels that produce annual landings of ca. 500 thousand tons during the last decade (FAO, 2012). Due to their economic importance, substantial effort and resources have been directed to monitoring the biomass of these fish, and to understanding the dynamics that control their recruitment variability.

Both species spawn over the shelf from 35° to 40°S (Castillo-Jordan *et al*., 2007). The main spawning ground between Mocha Island (38°20'S) and Corral (40°S) contributes ca. 80% of the spawning during Aug-Oct. Common sardine and anchovy reproduce year round, but the main spawning period is from late winter to early spring (Cubillos *et al*., 2007; Claramunt *et al*., 2013). Between-species differences in reproductive timing have been suggested, with anchovy showing a more protracted spawning season and a less marked spawning peak than sardine (Cubillos *et al*., 2009). Common sardine and anchovy recruitment occurs from December to March (austral summer), and sexual maturity is reached over the first year (Cubillos *et al*., 2001).

Characterizing the main processes affecting the early life stages of fish, such as retention, growth, and predation, is relevant to understanding the drivers of recruitment variability. Eggs and larvae that are retained in the coastal region, where planktonic food is abundant,

have higher probability of surviving to recruitment. In the southern HCS, the coastal circulation is strongly seasonal, with strong upwelling in spring-summer, and downwelling or weak upwelling during fall-winter, which creates a strong seasonal cycle in plankton biomass. Cubillos *et al.* (2001) postulated that the main spawning period of common sardine and anchovy is an evolutionary adaptation to the seasonality in coastal circulation and plankton production: downwelling or weak upwelling in late winter favors ichthyoplankton retention, whereas the increased planktonic biomass in spring favors rapid growth of feeding-larvae and juveniles. However, as the reproductive activity of the fish may extend to late spring, especially for anchovy in the northern spawning sites (Cubillos and Claramunt, 2009), the question of how the early life stages cope with a potentially strong offshore surface transport remains.

Particle-Tracking Models (PTMs) coupled to regional circulation ocean model outputs are useful tools to represent dynamics affecting early life stages of small pelagic fish (e.g. Mullon *et al*., 2003; Lett *et al*., 2007; Brochier *et al*., 2008; Parada *et al*., 2012). This study uses PTMs coupled to a realistically forced physical-biological ocean model from the southern Humboldt system to explore the spatiotemporal variability in ichthyoplankton coastal retention, as well as the coupling between fish larvae and model-derived plankton fields. The main goals are to identify the dominant scales of variability in coastal retention, and investigate if the observed spatial and temporal spawning patterns of common sardine and anchovy may be explained by patterns in coastal retention, dispersal and/or prey availability.

3.3. Data and Methods

3.3.1. Numerical model

The ocean circulation model is based on the Rutgers version of the Regional Ocean Model System (ROMS version 3.6) (Shchepetkin and McWilliams, 2005). The model

domain spans from 30.5° to 43°S, and from the coast to 81°W (Fig. 3.1), with a mean horizontal resolution of 3 km. The model has 40 terrain-following vertical layers and bottom topography based on Smith and Sandwell (1997). The physical model is coupled to an 8-component NPZD model (nitrogen-based; units: mmol N m^{-3}), which simulates the concentrations of nitrate, ammonia, two phytoplankton types (flagellates and diatoms), two zooplankton types (micro and mesozooplankton), and two detritus (small and large) types. The coupled physical-NPZD model is forced with wind velocity from QuikSCAT and ERA-Interim atmospheric fields (water flux, rain, pressure, humidity, air temperature, shortwave radiation, and downward longwave radiation) from 2002-2008. The coupled model produces physical and ecological outputs that agree with the main seasonal and subseasonal dynamics of circulation, temperature, mixed layer depth, sea level, and phytoplankton production (Chapter 2, Appendix A).

3.3.2. Particle tracking experiments

The PTM is an updated version of the model implemented by Batchelder (2006), which uses a fourth-order Runge-Kutta integration scheme to simulate Lagrangian particle trajectories. The PTM was forced by horizontal and vertical currents. At each time step, the 3D velocity fields at the location of each particle were linear interpolated in space and time from the stored daily ROMS fields. The particle's location was saved to an output file daily; also stored daily was the time-averaged environment (plankton concentration, temperature) experienced by each particle over the preceding day. Particle trajectories were simulated for 30 days, a period when horizontal swimming in young sardine and anchovy is weak and does not influence retention (Brochier *et al*. 2008). The time step of the PTM simulations was 15 minutes. In all simulations, particles were seeded uniformly every 3 km over the shelf (shoreward of the 250 m isobath). This corresponds to more than 2,900 particles, with ca. 1,200 in the northern spawning region (NSR, 34°30'-37°20'S) and ~1,700 in the southern spawning region (SSR, 37°20'-41°00'S) (Table 3.1), regions where most of the spawning is observed (Cubillos *et al*., 2007).

We performed three types of particle-tracking experiments to consider different processes controlling positions in the water column: 3-D advection only (ADV), advection plus ontogenetic - diel vertical migration (O-DVM) and advection plus ontogenetic vertical migration to 20 m depth (OVM20) (Table 3.1). In the ADV experiments, we consider that eggs and larvae are neutrally buoyant passive particles. Because small pelagic fish eggs and larvae are mainly distributed in the upper 20 m of the water column (Coombs *et al*., 2004; Landaeta and Castro, 2012), the effect of initial depth on eventual retention was evaluated by seeding particles every 3 days, from April 2002 to November 2008, at four depth levels: 5, 10, 15, and 20 m. Those experiments are referred to as ADV05, ADV10, ADV15, and ADV20, respectively. This implies 805 seeding times at each depth and the release of more than 10^7 passive particles. In the O-DVM experiments particles were initialized at 10 m depth, and simulations were performed every 3 days as in the ADV10 experiments, but we added a simple diel scheme of vertical migration from day 16 to day 30. Previous studies suggested that larvae with standard length > 10 mm (post-flexion) inflate their gas bladder during nighttime to stay closer to the surface (Landaeta and Castro, 2012). Based on an observed age-size relationship for anchovy (Hernandez and Castro, 2000), we assumed that O-DVM began at day 16 of the simulation. Two O-DVM depth ranges were tested, 10-35 m and 20-35 m, derived from the day and night anchovy distribution showed by Landaeta and Castro (2012). Particles were kept 5 m above the bottom during the day in regions where the water depth was less than 35 m. The vertical movement was simulated using the parameterization described by Drake *et al*. (2013), considering a maximum speed of 0.5 cm s^{-1} that decreases exponentially as the particle approaches the daytime or nighttime target depth. Time of sunset and sunrise were functions of latitude and day of the year. In the OVM20 experiment, particles were initialized at 10 m depth, experienced 3D passive advection during the first 16 days, and horizontal advection at a target depth of 20 m for the remaining simulation period. The retention patterns from OVM20 and O-DVM [20-35] were compared to evaluate in which extent the daytime depth in the O-DVM experiment contributed to retention enhancement. We did not consider a vertical random walk (RW) to simulate vertical

diffusion in any of the experiments above, since adding a RW effect substantially increases the computation time. However, exploratory analyses revealed similar retention indices derived from experiments with and without vertical RW (not shown).

To examine coastal retention, we defined a Retention Index (RI), which is the fraction of released particles that after 30 days of simulation were located in regions where the bottom depth was shallower than 500 m. This bathymetric contour follows closely the 250 m isobath, but keeping a more uniform width along the study region (Fig. 3.1). The importance of the starting (seeding) location to nearshore retention was evaluated with a Seeding Performance Index (SPI), which is the number of retained particles contributed by a specific seeding point during a multi-release time interval, normalized by the total number of particles released at that point. For example, a location with a SPI of 0.4 in Aug-Oct means that 40% of the particles released from that location during Aug-Oct were retained inshore of the 500 m isobaths after 30 days. The SPI does not distinguish between particles that have remained nearshore throughout the 30-day simulation and particles that went offshore but returned onshore to within the 500 m isobaths on day 30. SPI maps generated from Aug-Oct releases are compared with the distribution of small pelagic eggs derived from 0-70 m vertical net sampling from Aug-Oct surveys done since 2002 (except 2005) in the region from 33° to 41°S, and from the coast to near the 250 m isobath (Cubillos *et al*., 2007; Castillo-Jordan *et al*., 2007). A reasonable expectation, if the observed spawning grounds favor high nearshore retention of fish early life stages, is similar patterns of the SPI and egg distributions, with high egg density collocated with high SPI values.

3.4. Results

3.4.1. Coastal Retention Patterns

In the southern spawning region (SSR, Fig. 3.1), the mean RI during the period examined (Apr 2002 - Nov 2008) is 0.32, 0.39, 0.45, and 0.48 for the ADV05, ADV10, ADV15, and ADV20 experiments, respectively. Retention shows strong seasonal variability, with maximum values in winter and minimum in spring-summer (Fig. 3.2a, b). RI decreases with release depth in May-Jul, and increases in Aug-Apr, so the strength of the annual cycle decreases with depth. The amplitude of the annual signal varies interannually, being the smallest in 2007, especially for ADV15 and ADV20 (Fig. 3.2a). In addition to seasonal and interannual variability, the RI time series show strong 40-to-60 day oscillations, especially in the spring-summer of 2005-06 and during the entire 2007 year (Fig. 3.2a). On the other hand, RI shows relatively weak submonthly variability. The SSR-RI time series of the four depth levels are highly correlated to the 30-day low-pass alongshore wind stress, indicating that wind variability strongly drive retention south of Point Lavapie (Table 3.2; Fig. 3.2a, e).

In the northern spawning region (NSR, Fig. 3.1), the mean RI from the study period is 0.17, 0.28, 0.36, and 0.42 for the ADV experiments initialized at 5, 10, 15, and 20 m depth, respectively. The seasonal patterns in the NSR-RI differ from those in the SSR-RI (Fig. 3.2c, d). This can be partially linked to the weaker downwelling favorable winds over the NSR (Fig. 3.2f), which leads to reduced nearshore retention in fall-winter. Particles released at 5 m depth show one RI peak (>0.5) in fall-winter, remaining small (<0.15) during the rest of the year, whereas particles released at deeper depths also have high retention in late spring and summer (Fig. 3.2c). The average seasonal cycle for ADV15 and ADV20 show maximum retention in summer (Feb) rather than fall-winter. Releases slightly shallower in the water, ADV10, have similar retention during summer and winter (Fig. 3.2d). The magnitude of the summer RI peaks exhibits strong interannual variability, with the greatest retention in 2008 (>0.75) and the weakest in 2004 (0.3-0.4) (Fig. 3.2c). Variability in summer retention appears to be disconnected from the surface wind signal. The correlation between NSR-RI and wind stress markedly decreases with particle release depth (Fig. 3.2e; Table 3.2).

The highest retention period in SSR and NSR do not coincide with the core spawning times of common sardine and anchovy. Actually, from July to October, the mean SSR-RI declines from ca. 0.6 to 0.12 (ADV05), 0.25 (ADV10), 0.38 (ADV15) and 0.43 (ADV20) (Fig. 3.2b, solid lines), and the mean NSR-RI declines from ca. 0.33 to 0.08 (ADV05), 0.18 (ADV10), and 0.28 (ADV15) (Fig. 3.2d). Note that the RI criterion evaluates if a particle after 30 days is someplace on the shelf, not discriminating among shelf locations. However, the shelf north of Point Lavapie (~37°S) is highly productive and appears to be the main nursery region of anchovy and sardine (Cubillos *et al*., 2009). We examined if the timing of spawning is linked to retention on the shelf north of Point Lavapie. Indeed, the highest fraction of particles originating from the SSR that are retained north of Point Lavapie are those that are released during the main spawning period (Fig. 3.2b, dash lines), suggesting that connectivity to the main nursery region is important to the reproductive strategy of these small pelagic fish.

The 20-35m O-DVM scheme had a greater effect on the retention index than did the larger amplitude (10-35m) O-DVM (Fig. 3.3). In the SSR simulations, O-DVM [20-35m] increases the spring-summer retention by more than 0.1 the ADV10 levels (equivalent to >25% increase), whereas the fall-winter retention does not show significant changes (Fig. 3.3b). Also, O-DVM [20-35m] increases by ca. 0.07 (39%) the connectivity from the SSR to the region north of Lavapie during Sep-Oct (Fig. 3.3b, grey bars). In the NSR simulations, O-DVM [20-35m] increases RI by around 0.06 in winter and >0.10 in spring-summer (18 and 30%, respectively; Fig. 3.3e), accentuating the February retention peak. O-DVM [20-35m] retention is in average only ~0.025 larger than OV20 retention (Fig. 3.3c, f), which implies that the daily change in larval depth does not produce a significant change in retention.

SPI patterns in Aug-Oct

We compared spatial egg density of common sardine derived from ichthyoplankton sampling in Aug-Oct with the corresponding Seeding Performance Index (SPI) from the PTM (Fig. 3.4). Anchovy eggs are distributed similarly to common sardine (Cubillos *et al*., 2007). To describe the cross-shore pattern, we refer to the region inshore of the 100 m isobaths as the inner shelf, and beyond as the outer shelf. The highest egg density is observed in the inner shelf, especially around Constitucion (CON), Dichato (DI), Concepcion Bay (CB), Gulf of Arauco (GA), and off the embayment between Tirua (TI) and Point Galera (PG) (Fig. 3.4a; See Fig. 3.1b for locations). The similarity between the egg distribution and the Aug-Oct SPI varies between regions and among experiments (Fig. 3.4b-f). Considering both the NSR and SSR, the strongest agreement is with ADV20, O-DVM [20-35m] and OVM20, and the weakest with ADV05. In the southern seeding region, the SPI increases southward linked to the meridional trend in downwelling favorable winds (Fig. 3.2f). Since egg density does not show a southward increase, factors other than retention determine the southern limit of the spawning region. A potential factor could be the connectivity between the SSR and the nursery region north of Point Lavapie. To evaluate this, we estimated the SPI distribution with the retention criterion constrained to be the continental shelf north of Point Lavapie. The spawning region with the highest contribution to the nursery region north of Lavapie is located on the inner shelf north of ~39°30'S (Fig. 3.4h-l). The potential connectivity between the SSR and the northern nursery region increases with increasing release depth and with O-DVM.

To visualize dispersal differences among experiments, we estimated the particle densities at simulation day 30, derived from Aug-Oct particle releases (Fig. 3.5). Particle density is low south of each seeding region, reflecting a dominant northward particle transport. Particle meridional dispersal and distance to the coast (DC) decrease with increasing initial depth and by including vertical migration after day 16. O-DVM increases the

number of particles within the first 20 km from the coast (see DC histogram in Fig. 3.5 panels). In the ADV05 and ADV10 experiments most of the retained particles north of Point Lavapie are located on the outer shelf. The only two places with relatively high particle density on the inner shelf are the Gulf of Arauco and Concepcion Bay (Fig. 3.5e, f). In contrast, the ADV20 and O-DVM [20-35m] experiments have high particle density over both the inner and outer shelf (Fig. 3.5g, h).

SPI seasonal changes

The meridional variability of the SPI seasonality over the inner and outer shelf is shown in Figure 3.6. On the outer shelf, the four experiments produce maximum values in winter south of 36°S (Fig. 3.6a-d). The transition to the lowest SPI values, after the winter maximum, occurs progressively later in the year as latitude increases, reflecting the meridional progression in alongshore wind stress near the coast (Fig. 3.2f). In addition to the winter SPI maximum, a weak summer maximum (stronger north of Lavapie) is observed in ADV10, ADV20 and O-DVM [20-35m] (Fig. 3.6b-d). Those seasonal patterns are also observed in the inner shelf, though important differences exist. All the experiments but ADV05 (during winter in the southernmost region) have higher retention on the inner shelf (Fig. 3.6e-h), with SPI values >0.5 prevailing in the ADV20 and O-DVM [20-35m] experiments. The amplitude of the summer peak is much stronger on the inner shelf. Also, Concepcion Bay, Gulf of Arauco, and the southern portion of the Tirua-Point Galera embayment have high SPI values in the four seasons, indicating that successful egg and larval retention is possible year-round.

3.4.2. Coupling with plankton fields

We estimated average plankton concentration values experienced -over the Lagrangian trajectories- by particles from a given experiment, as a function of seeding time and simulation day (drift period, 1 to 30 days), from which 5-day mean climatologies were

derived. The climatologies for ADV10 are showed in Figure 3.7. Seasonal amplitudes of diatoms are the greatest (>3 mmol N m^{-3}), and significantly larger than the maxima within the micro- and mesozooplankton (ca. 0.4 and 1.2 mmol N m^{-3}, respectively). The seasonal plankton amplitude decreases with drift period in spring-summer, as the prevailing upwelling condition moves particles offshore. The main spawning period of small pelagics (demarked by dash lines in Fig. 3.7) starts after a minimum in diatom and mesozooplankton prey fields. A peak in microzooplankton occurred during the early spawning season, as well as a secondary maximum in mesozooplankton in the mid and late spawning period (stronger in the NSR).

Changes in the daily mean plankton concentration experienced by particles through the simulation time, during the mid-spawning season, are shown in Figure 3.8. When the simulation started, the lowest plankton concentration values were for ADV20, since the plankton maximum was usually located at depths shallower than 20 m near the coast (not shown). Diatom concentration was largest at or near the simulation onset. As particles moved offshore, diatom concentration decreased ca. 53, 38, and 22% over the simulation period in ADV05, ADV10, and ADV20, respectively (Fig. 8a). Unlike diatoms, the largest mesozooplankton concentration was observed around day 8 in ADV05/10 (Fig. 8b), reflecting that the mesozooplankton maximum is located offshore of the diatom maximum. Because the cross-shore gradient in mesozooplankton was smaller than for diatoms, a smaller mesozooplankton concentration decrease was observed in ADV05/10, around 16 and 19%, respectively. Microzooplankton values were about a half of the mesozooplankton values, showing relatively small variation during the simulation (Fig. 3.8c). The O-DVM [20-35] scheme (thin solid line) produced an initial decrease in diatom and zooplankton concentration, which was mainly associated with lower plankton concentration at 35 m depth. That negative trend changed a few days later as particles tended to move onshore to more productive waters. Particles performing O-DVM [20-35] were exposed to higher mean plankton concentration than ADV10 during nighttime.

3.5. Discussion

The coastal retention index we used is based on a bathymetric criterion (<500 m depth) following previous studies on ichthyoplankton dynamics (e.g. Mullon *et al*., 2003; Brochier *et al*., 2008). Retention is assumed to increase larval survival, since conditions that lead to low mortality, such as high prey availability and low gelatinous predator abundance, occurs in the coastal region. Plankton observations (e.g. Castro *et al*., 2000 and the outputs from the physical-biological ocean model (Chapter 2) support the retention assumption. Egg/larvae mortality was not considered in our model, so the derived dispersal/retention patterns represented potential dispersal/retention driven by ocean circulation only. We also assumed that the seasonal retention patterns from the period 2002-2008 are typical of long-term seasonal conditions that modulate the success of reproduction of sardine and anchovy. Wind variability linked to ENSO can affect seasonal retention patterns, as negative (positive) upwelling anomalies prevail during El Nino (La Nina) years (Montecinos and Gomez, 2010). This is evident by comparing a weak El Nino year (2002) and strong La Nina year (2007) (Fig. 3.2). Nevertheless, 2002-2008 was characterized by neutral to weakly warm ENSO conditions that did not strongly alter seasonal circulation patterns.

The seasonal patterns of the retention index from passive particle tracking experiments varied as function of seeding region and release depth. In the SSR the maximum (minimum) retention was in winter (summer) for all initial depths, linked to the prevailing wind-driven downwelling (upwelling) condition. The amplitude of the RI seasonal cycle decreased with initial depth, reflecting the decrease in both along- and cross-shore currents with depth. Seasonal retention in the NSR varied substantially with the initial depth. At 5 m, the RI pattern was similar to that in the SSR. On the other hand, Particles seeded deeper (15 and 20 m) had maximum RI in summer, and minimum in spring. The differences reflect a strong vertical current shear north of Lavapie, with opposed cross-shore circulation patterns in the upper 20 m layer (Fig. 3.9). Seasonal

changes in the vertical current shear can have significant impact on particle dispersal and retention. Off Peru, Brochier *et al*. (2008) reported that a thin Ekman layer in summer enabled relatively shallow onshore return current that decreased retention near the surface and increased retention at 30-45 m depth. A thicker Ekman layer in winter produced the opposite effect. Off central Chile, the maximum retention during February for particles at 15 or 20 m might also be related to the weaker alongshore current north of Lavapie. The last is concomitant with a weakening in meridional wind stress (Fig. 3.2f) and a secondary maximum in coastal sea level (not shown) after the spring-summer transition (Rahn *et al*, 2015). As in other eastern boundary current upwelling systems (Brink and Robinson, 1998), the dominant currents off central Chile are alongshore, with relatively weak and spatially variable cross-shore currents, and significant mesoscale variability (Fig. 3.9). Our model outputs and altimetry observations suggest significant changes in mesoscale circulation between spring and summer. Loss of virtual larvae from the coastal region is greatest during Sept-Nov, when the modeled coastal jet has a seasonal maximum with flow off the shelf to the north/northwest at surface and 20 m depth (Fig. 3.9a-b). In Jan-Mar, when particles seeded at 15 and 20 m are maximally retained along the coast, the prevailing surface flow is also to the north/northwest (Fig. 3.9d) as in Sept-Nov, but the flow at 20 m shows mesoscale structures, including a persistent cyclonic eddy off 34-36°S (Fig. 3.9e). These circulation features would transport virtual eggs/larvae poleward near the shelf-break, opposite to the prevailing equatorward flow on the shelf. As a consequence, the northward particle advection is reduced and coastal retention increases.

Temporal and spatial spawning patterns in small pelagic fish may be constrained by a combination of factors operating concurrently, such as coastal retention, connectivity to nursery regions, and both prey and predator density (Parrish *et al*., 1983; Bakun, 1996; Castro *et al*., 2000). Previous observational studies related the winter-spring timing of common sardine and anchovy spawning to favorable retention conditions, as intermittent downwelling events are frequent during late winter and early spring (Castro *et al*., 2000;

Cubillos *et al*., 2001). In the southern spawning region, our passive particle tracking experiments showed high retention during the early spawning season (Aug), but reduced retention for the mid and late spawning season (Sep-Oct). In the northern spawning region, the retention of larvae was close to the seasonal minimum, throughout Aug-Oct, which is clearly inconsistent with the hypothesis that spawning is exclusively controlled by retention. This differs from Brochier *et al*. (2011), which found maximum model ichthyoplankton retention in the southern HCS coincident with the anchovy's main spawning period. However, they considered winter only, which is inconsistent with observations that show that peak spawning extends from late winter to mid spring (Cubillos and Claramunt, 2009; Claramunt *et al*., 2013). Spatially, the similarities between egg density and the Aug-Oct SPI (Fig. 3.4), both with maximum values inshore of the 100 m isobath, suggest that nearshore retention is important in defining spawning site fidelity in these small pelagic species. Moreover, the SPI revealed that although the overall retention over the NSR is substantially lower than retention from the SSR during Aug-Oct, several northern spawning locations, like the Gulf of Arauco and Dichato, have relatively high retention favoring larval survival. Consequently, coastal retention explained the observed spawning areas but weakly constrained the observed spawning timing.

Potential connectivity between spawning and nursery regions could be another factor explaining the spatiotemporal patterns in spawning. Although the most productive coastal region and main nursery regions of common sardine and anchovy are north of Point Lavapie (Cubillos *et al*., 2009), the most important spawning region is south of this point (38°-39°S). Virtual eggs/larvae seeded there had better chance of being transported to the nursery regions than particles seeded further south. This could explain the disagreement between the SPI and the egg distribution trends in the SSR (Fig. 3.4). The highest fraction of particles seeded in the SSR and retained nearshore north of Lavapie is found during the main spawning period, mainly driven by the equatorward coastal jet near the shelf break (Fig. 3.9a, b). A strong coastal jet is also observed in summer (Fig. 3.9d, e), but the

associated offshore transport is stronger than during spring, increasing the advective losses. Larvae that are transported to and retained in this main nursery region could take advantage of a higher plankton production.

Changes in potential prey density were examined using the plankton fields derived from the physical-biological ocean model. Diatom, microzooplankton and mesozooplankton are model simplifications of more diverse prey types upon which clupeid larvae feed. We use these three model components as proxies of larval food availability. The model simulations indicate that the spawning season in Aug-Oct is a transition period from low to high plankton biomass. In mid-winter months of June and July diatoms and mesozooplankton are near annual minima. During spring, due to coastal upwelling and increasing light for photosynthesis, the productivity of the ecosystem picks up, resulting in greater concentrations of microzooplankton and mesozooplankton. Studies of sardine and anchovy diet show that the larvae of both species have similar prey preferences, foraging on a combination of phytoplankton and microzooplankton, including diatoms, tintinnids, microflagelates, copepods eggs and nauplii (Llanos-Rivera *et al*., 2004; Yanez-Rubio *et al*., 2011). Villavicencio and Muck (1983) estimated a maintenance prey density for anchovy larvae of 168 nauplii liter^{-1}, and a mean nauplius mass of 0.15 µg dry weight (~0.75 µg wet weight). Considering that 1 g wet weight m^{-3} is roughly equivalent to 1 mmol N m^{-3} (Megrey *et al*., 2007), that maintenance prey density corresponds to 0.126 mmol N m^{-3}, much smaller than the derived model prey concentration. Therefore, the model is consistent with observations suggesting that despite plankton biomass in late winter being an order of magnitude lower than in summer, food is not strongly limiting larval growth (Castro *et al*., 2000). Spawning in late-winter/early-spring instead of summer implies a longer growing season, which could favor larger individual size and higher survival at the end of the fish's first year (Cargnelli and Gross, 1996). We did not explicitly model predation during the upwelling season. However, if we assume that mesozooplankton abundance is linked to predation rates on ichthyoplankton, as suggested for Pacific sardine off California (Agostini *et al*., 2007), then strong predation might be

expected in summer, which might exert evolutionary pressure for earlier spawning, perhaps to peak during the winter-spring transition.

Previous modeling studies showed that vertical migration could play an important role in coastal retention of planktonic species (e.g. Batchelder *et al*., 2002; Carr *et al*., 2008; Ospina-Alvarez *et al*., 2012a; Drake *et al*., 2013). Zooplankton (including ichthyoplankton) can take advantage of opposing cross-shore currents during a DVM cycle, or avoid the strongest surface offshore flow by migrating to deeper depths through their ontogeny. Besides, DVM can enhance connectivity from spawning to nursery regions (Parada *et al*., 2008). Observational studies addressing the vertical migration dynamics in clupeid larvae are scarce. The information available for anchovy off central Chile showed vertical differences (although not strong) between the distributions of pre- and post-flexion anchovy larvae, linked to the ability of the post-flexion larvae to inflate/deflate their gas bladder during nighttime/daytime (Landaeta and Castro, 2012). Information on other clupeid species also suggests larval DVM, which could range from the surface to 30-60 m depth, being more clearly identified in late larvae (e.g. *Engraulis encrasicolus*, Olivar *et al*. [2001]). Because of our limited information on fish DVM, in this study we evaluated only two simple step-wise, non-evolving depth schemes, 10-to-35 and 20-to-35 m. Sunrise and sunset keyed the transitions between day and night depths. These two ontogenetic DVM scenarios were used to explore whether diel changes in vertical distribution impacted retention patterns and spawning strategies. Because the O-DVM [20-35m] scheme enables virtual larvae to remain below the strong offshore flows of the surface layer during both day and night, retention nearshore was increased during spring-summer in the SSR and year-round in the NSR, resembling the seasonal patterns derived from ADV20. However, the O-DVM [10-35m], which had virtual larvae in the surface boundary layer during nighttime, produced a minor impact on retention. This result is consistent with modeling studies by Carr *et al*. (2008) and Drake *et al*. (2013), which showed that offshore transport of larvae is reduced more effectively when larvae remain below the surface boundary layer (~15 m deep), since the strong surface offshore

flow cannot be fully compensated by a weak subsurface onshore flow. The similarity between the retention patterns derived from O-DVM [20-35m] and OVM20 indicate that most of the enhanced retention was due to removing larvae from the surface flows. This means that particles incursion to 35 m depth during daytime in the O-DVM experiment had low impact. The O-DVM [20-35] and OVM20 increase in retention was concurrent with a decrease in the mean particle distance to the coast, and a higher connectivity between the SSR and the northern nursery region. Although O-DVM [20-35] kept particles close to the coast, where the highest prey concentration values existed, the greater depths decreased initially the daily mean plankton concentration experienced by particles. The latter was a consequence of the daytime spends at 35 m depth, where plankton concentration values were usually low. The decrease is compensated at the simulation end, as particles approach to more productive water near the coast. Particles that stayed at 20 m were exposed to higher plankton concentration than passively drifting particles, especially when a subsurface phyto- and zooplankton maximum occurred away from the inner shelf (not shown). This explains that OVM20 had a more positive impact on plankton concentration than O-DVM [20-35m].

The potential effect of egg or larval buoyancy on the particle trajectory was not examined. Sensitivity analysis from model particle retention patterns in other upwelling systems suggested a negative relationship between coastal retention and egg buoyancy (e.g. Parada *et al*., 2003; Brochier *et al*., 2008). However, information on anchovy and common sardine egg/larval density is not available in the Humboldt System. Observations for similar clupeids showed neutral to slightly buoyant eggs, a positive relationship between egg and seawater density at the spawning site, and egg buoyancy varying as a function of egg development and salinity (Boyra *et al*., 2003; Ospina-Alvarez *et al*., 2012b). Clupeid larvae buoyancy and its changes through ontogeny remain undocumented. Since most of our modeled 30-day drift period corresponds to larval stage (the hatching age is ~2-3 days), we chose to exclude buoyancy from the analysis.

By generating RI at temporal resolution of 3-days, we found strong intraseasonal variability in retention, especially south of Point Lavapie, linked to near 50-day wind oscillations. Although this intraseasonal variability is strongest in late spring and summer, it also occurred over the main spawning season (Fig. 3.2a, c). Chapter 2 showed that the intraseasonal wind oscillations drive significant changes in coastal upwelling and plankton production, which can modulate prey and predator density. The intraseasonal variability in coastal retention and prey/predator density may impact larval survival within the multiple months fish-spawning season. Because of differences in the timing of peak reproduction of anchovy and common sardine, anchovy having a more protracted spawning season than sardine, we might expect that intraseasonal variability would produce differential impacts on their recruitment. It is beyond the scope of this paper to describe in detail the intraseasonal changes on retention and prey/predator fields, but they probably are relevant to ichthyoplankton survival and worth of examination in future studies.

3.6. Concluding remarks

The transport, dispersal and prey density spatiotemporal patterns of early life stages of common sardine and anchovy off central Chile were simulated with a coupled Eulerian-Lagrangian modeling approach. We first tested the hypothesis that the observed spawning patterns promote high coastal retention. The results showed that the main August-October time of spawning was only partially associated with high retention nearshore, but the observed spawning locations promoted high coastal retention year round. Connectivity from the main spawning region (off the Tirua-Point Galera embayment) to the main nursery regions (north of Point Lavapie) was the highest during the spawning period, suggesting that this could be a key factor constraining the spawning timing. Simulations that explored several ontogenetic-diel vertical migration schemes provided greater coastal retention, and also enhanced the connectivity from the spawning locations to the nursery regions. We also evaluated using the low trophic model plankton fields whether the

seasonal peak in clupeid spawning might be related to high (favorable) prey density for larvae. Spawning timing appears favorable for larval feeding success, since peaks in microzooplankton and mesozooplankton, both main prey items in the larval diet, were found during that period.

Acknowledgements

F.G. is very grateful for the support of the Chilean National Commission for Scientific and Technological Research (CONICYT), the Fulbright Student Program, and the Graduate School of Oregon State University. We thanks to the Chilean Undersecretary of Fisheries by kindly providing observations of egg density.

Table 3.1. Particle tracking experiments discussed in text

Experiments	Description	Release depth (m)	Number of particles released per simulation	
			NSR	SSR
ADV05	3D advection	5	1228	1711
ADV10	3D advection	10	1228	1711
ADV15	3D advection	15	1205	1704
ADV20	3D advection	20	1182	1683
O-DVM [10-35]	3D advection from day 1 to 15; Horizontal advection plus DVM from day 16 to 30; DVM range: 10-35 m	10	1228	1711
O-DVM [20-35]	3D advection from day 1 to 15; Horizontal advection plus DVM from day 16 to 30; DVM range: 20-35 m	10	1228	1711
OVM20	3D advection from day 1 to 15; Horizontal advection at 20 m depth from day 16 to 30	10	1228	1711

Table 3.2. Maximum correlation between time series of Retention Index at simulation day 30 and the 30-day low-pass filtered meridional wind stress at 34°, 36° and 39°S. Lag at maximum correlation is between parenthesis (days). Time series were filtered with a 31-day triangular filter.

		WS 34°S	WS 36°S	WS 39°S
NSR	ADV05	-0.75 (16)	-0.73 (16)	-0.61 (16)
	ADV10	-0.64 (15)	-0.53 (17)	-0.31 (18)
	ADV15	-0.37 (14)	-0.23 (16)	-
	ADV20	-0.12 (13)	-	-
SSR	ADV05	-0.68 (14)	-0.82 (15)	-0.86 (16)
	ADV10	-0.71 (14)	-0.82 (15)	-0.83 (15)
	ADV15	-0.64 (12)	-0.71 (14)	-0.70 (14)
	ADV20	-0.50 (11)	-0.52 (12)	-0.48 (12)

* Only correlation coefficients significant at 95% level are shown. Sample size in the significance test was obtained with the modified Chelton method to account for time series autocorrelation (Pyper and Peterman, 1998)

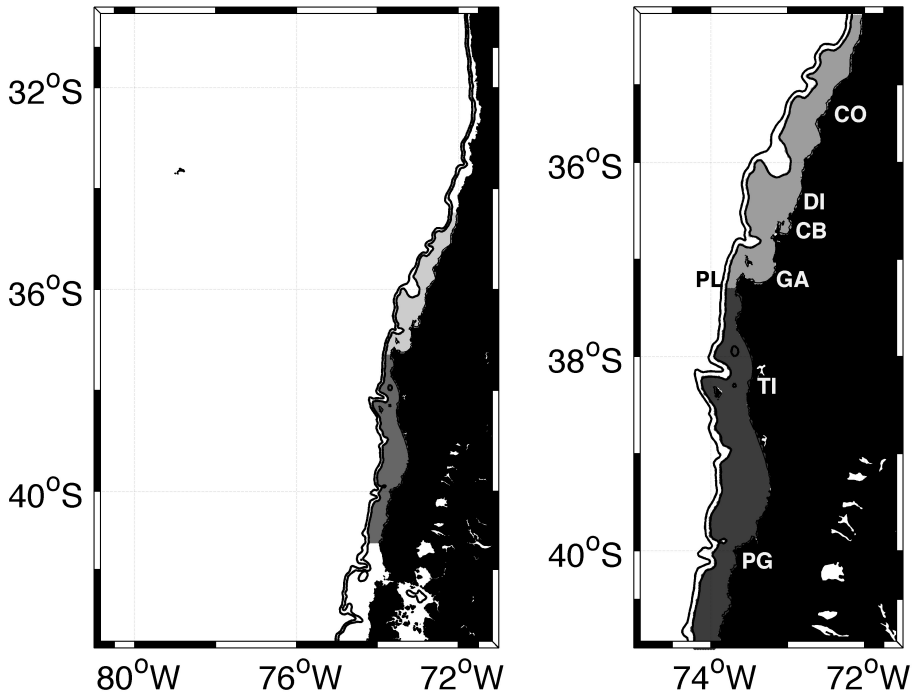

Figure 3.1. Study region. Left: Ocean model domain with the northern (light gray) and southern (dark gray) seeding regions used in the particle tracking experiments. Right: Detailed seeding regions with the locations of Constitucion (CO), Dichato (DI), Gulf of Arauco (GA), Punta Lavapie (PL), Tirua (TI), and Punta Galera (PG) are shown. The black contours depict the 250 and 500 m isobath.

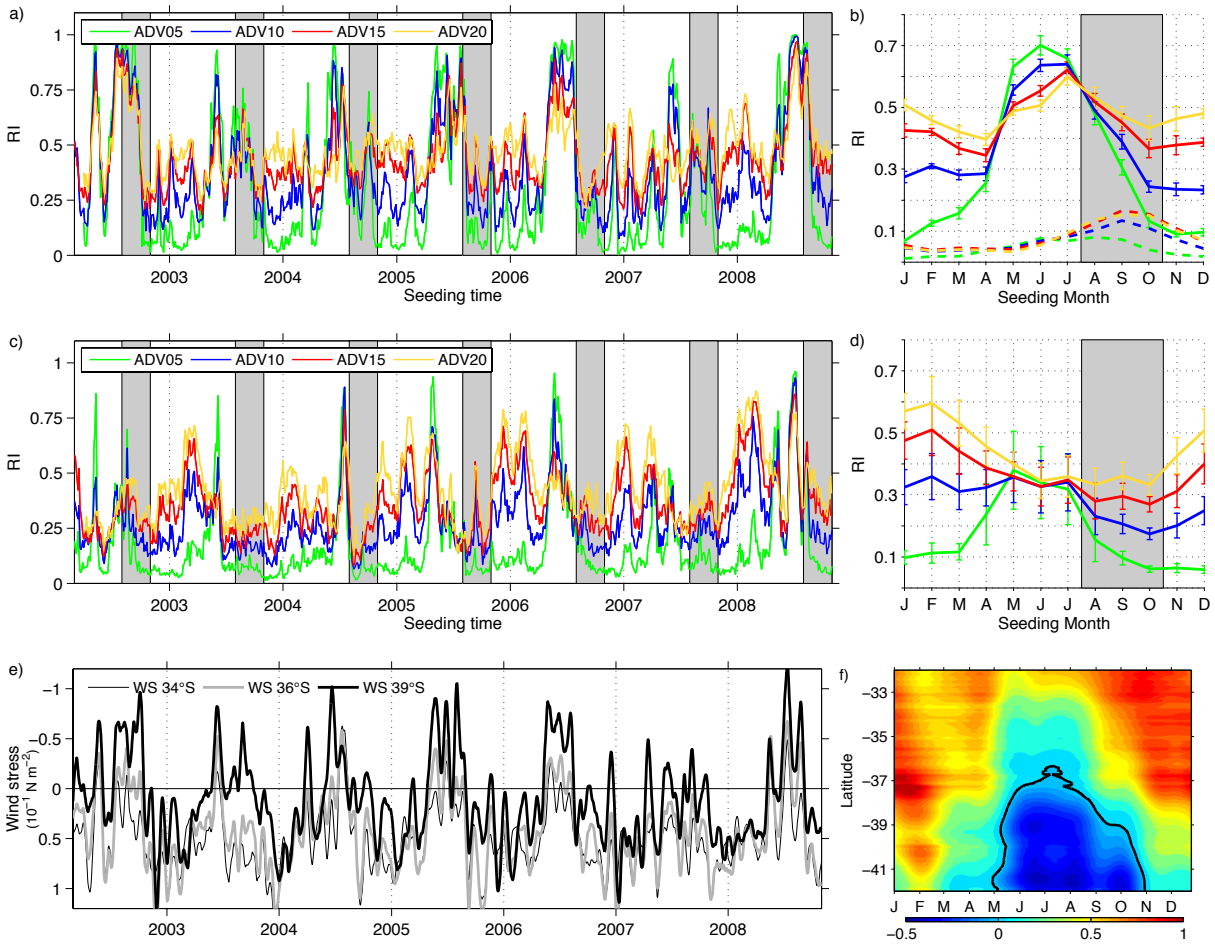

Figure 3.2. Retention index (RI) and wind stress variability. Left panels: RI time series at simulation day 30 derived from experiments initialized in the southern (a) and northern (c) spawning region, and 30 day low-pass filtered meridional wind stress (QuikSCAT) at 34°, 36° and 39°S (e); ADV05, ADV10, ADV15, and ADV20 refers to the ADV experiments with an initial depth of 5, 10, 15, and 20 m, respectively. Wind stress series are zonal averages over a ~75 km wide coastal band. Right panels: b, d) Monthly mean of RI (solid lines with the bars indicating one standard deviation) derived from the time series in left panels; dash lines in panel b show retention north of Point Lavapie; f) time-latitude diagram of the QuikSCAT meridional wind stress climatology (in 10^{-1} N m^{-2}). Gray area in panels a-d indicates the main spawning season. QuikSCAT data was obtained from the Centre d' Exploitation et de Recherche Satellitaire d' Archivage et de Traitement (www.cersat.ifremer.fr).

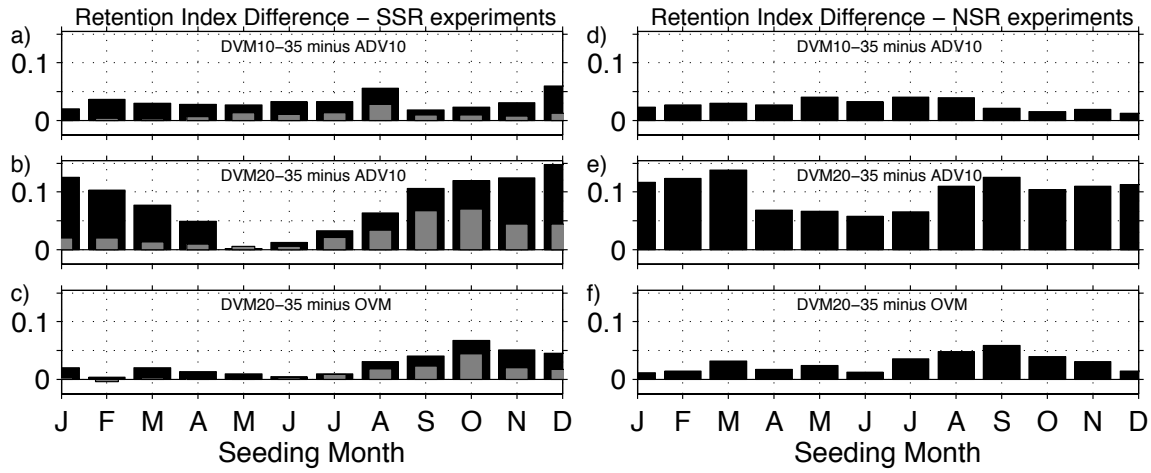

Figure 3.3. Vertical migration impact on retention: Retention Index differences (black bars) between experiments with vertical migration (O-DVM [10-35m] and [20-35m], OVM20) and ADV10 for particles seeded in the SSR (left) and NSR (right) at 10 m depth. Gray bars in left panels show the vertical migration effect on retention north of Point Lavapie.

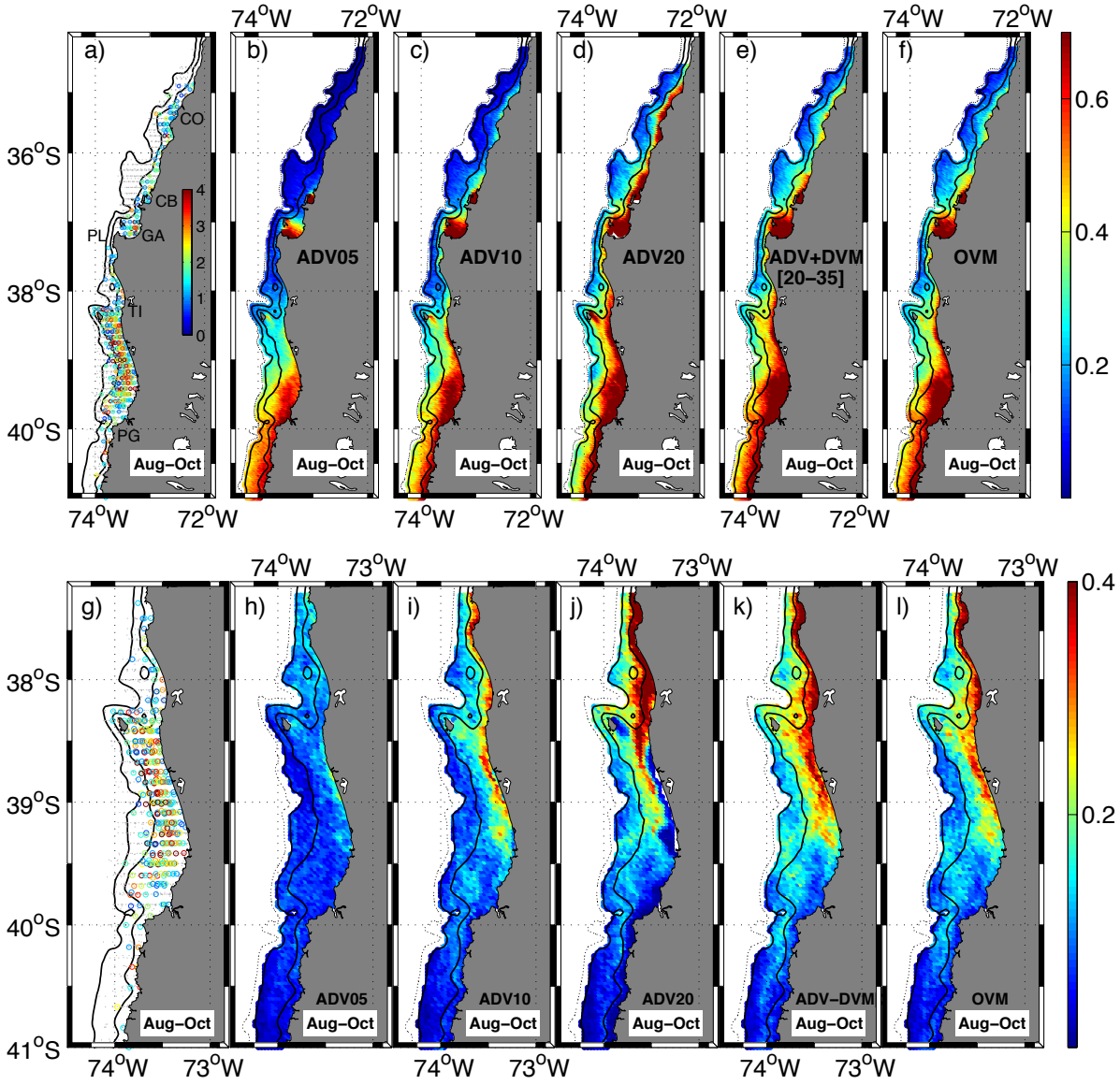

Figure 3.4. Spawning and Seeding Performance Index (SPI): a, g) Logarithm of common sardine egg density (in number per 50 cm^2) based on the Aug-Oct ichthyoplankton sampling from 2002-2010; both panels use the colorbar shown in panel a; b-f) Aug-Oct SPI derived from ADV experiments for particles seeded in the SSR and NSR; h-l) as in b-f but for particles seeded in the SSR only and retained north of Point Lavapie. The solid black contours depict the 100 and 250 m isobaths. The maximum possible SPI is equal to 1.

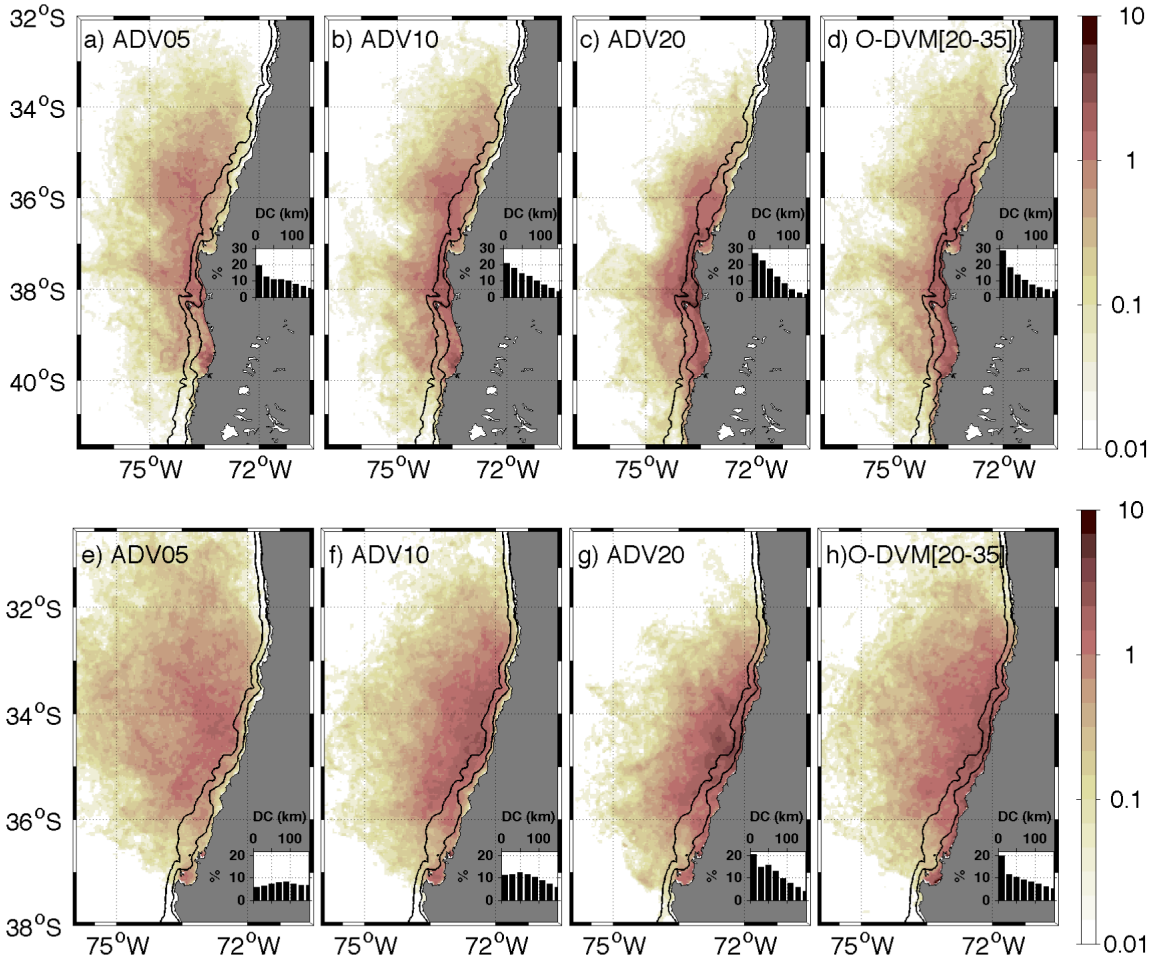

Figure 3.5. Particle density. Particles density at simulation day 30 derived from: a, e) ADV05; (b, f), ADV10, (c, g) ADV20, and (d, h) O-DVM[20-35] experiments initialized in the southern (a-d) and northern (e-h) spawning region during Aug-Oct. Solid black contours depict the 250 and 500 m isobaths. Particle density was scaled by the total number of particles released and multiplied by 10^4. Insets in panels show the frequency histograms (%) from the particle's mean distance to the coast (DC).

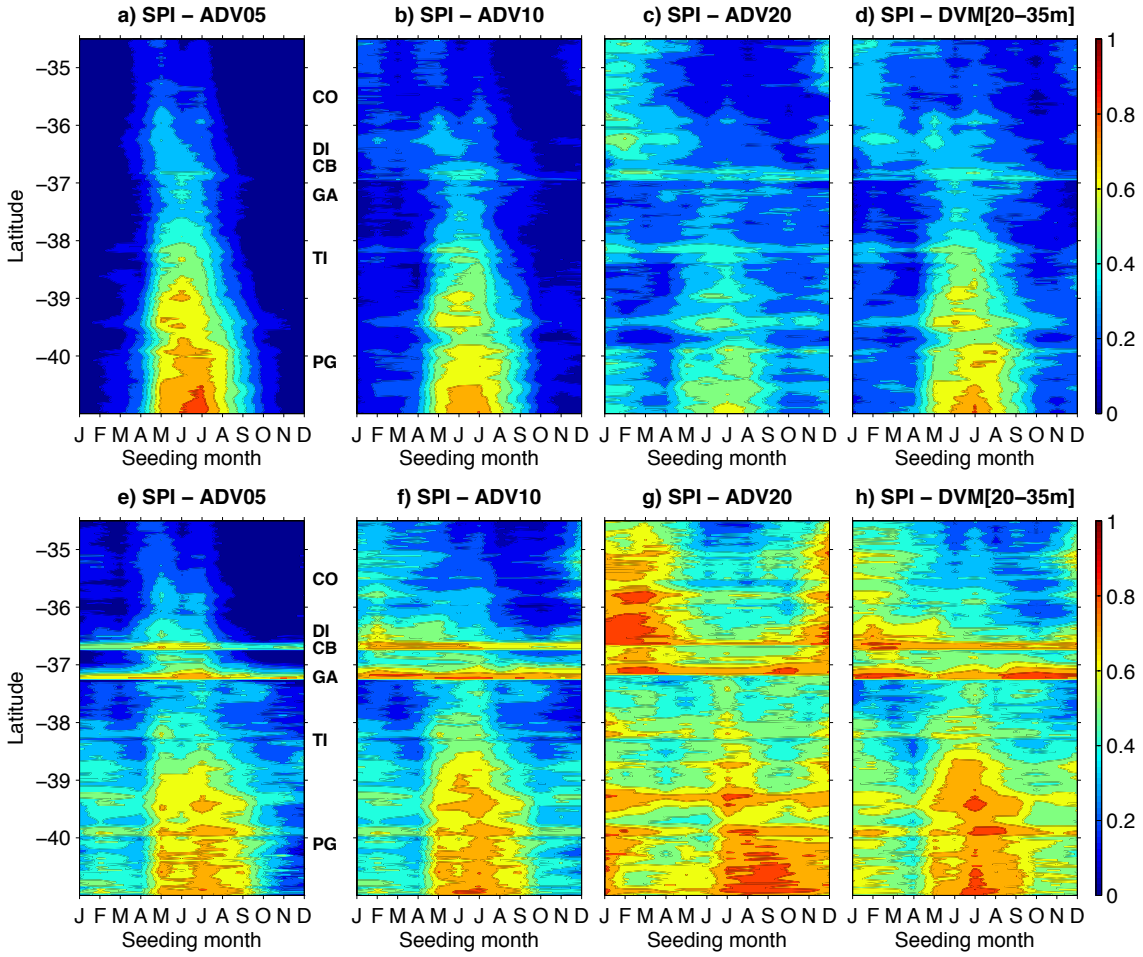

Figure 3.6. Monthly variability of the Seeding Performance Index. Top and bottom panels show patterns for the outer and inner shelf, respectively.

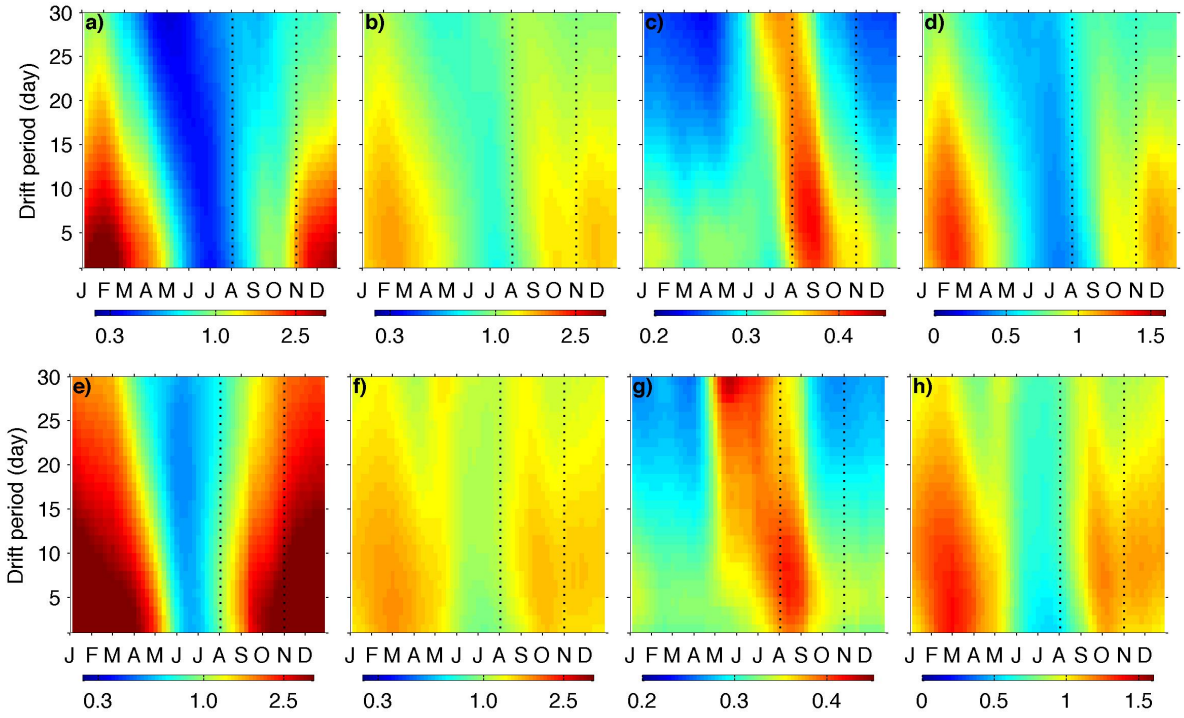

Figure 3.7. Seasonal patterns in plankton concentration (mmol N m^{-3}) experienced by particles (retained and non-retained). Patterns were derived from passive particle tracking experiments initialized at 10 m depth in the southern (top) and northern (bottom) spawning region during the period 2002-2008: Diatom (a, e), total zooplankton (b, f), microzooplankton (c, g), and mesozooplankton (d, h). The colorbars in panels a, b, e, and f are in log10 scale. Dotted lines mark spawning season (Aug-Oct).

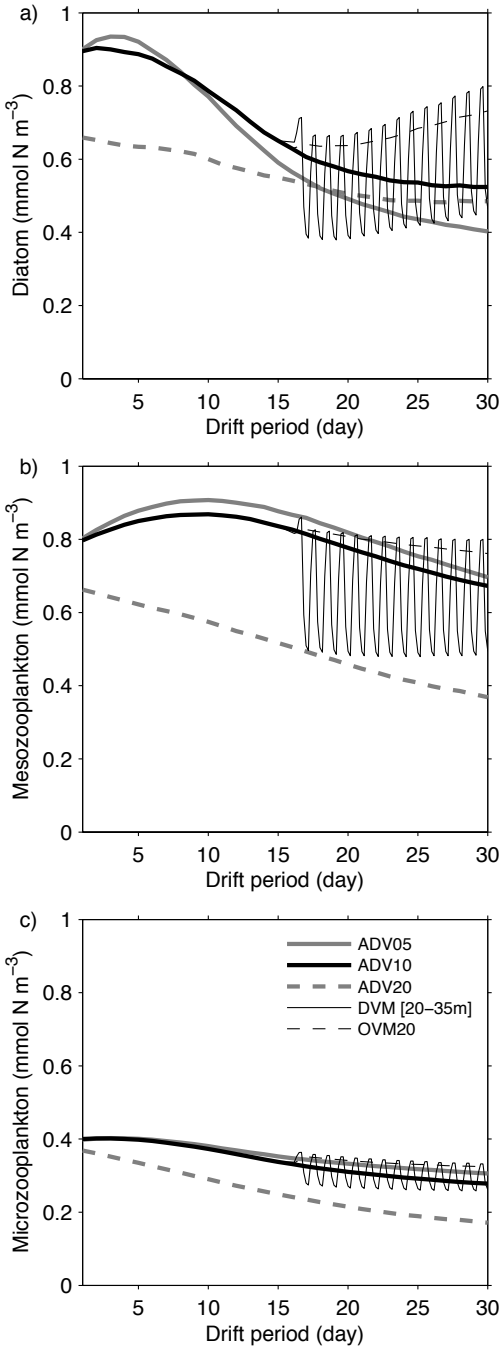

Figure 3.8. Plankton changes over drift period. Daily mean diatom (a), mesozooplankton (b), and microzooplankton (c) concentration as a function of drift time for experiments initialized in the SSR during September.

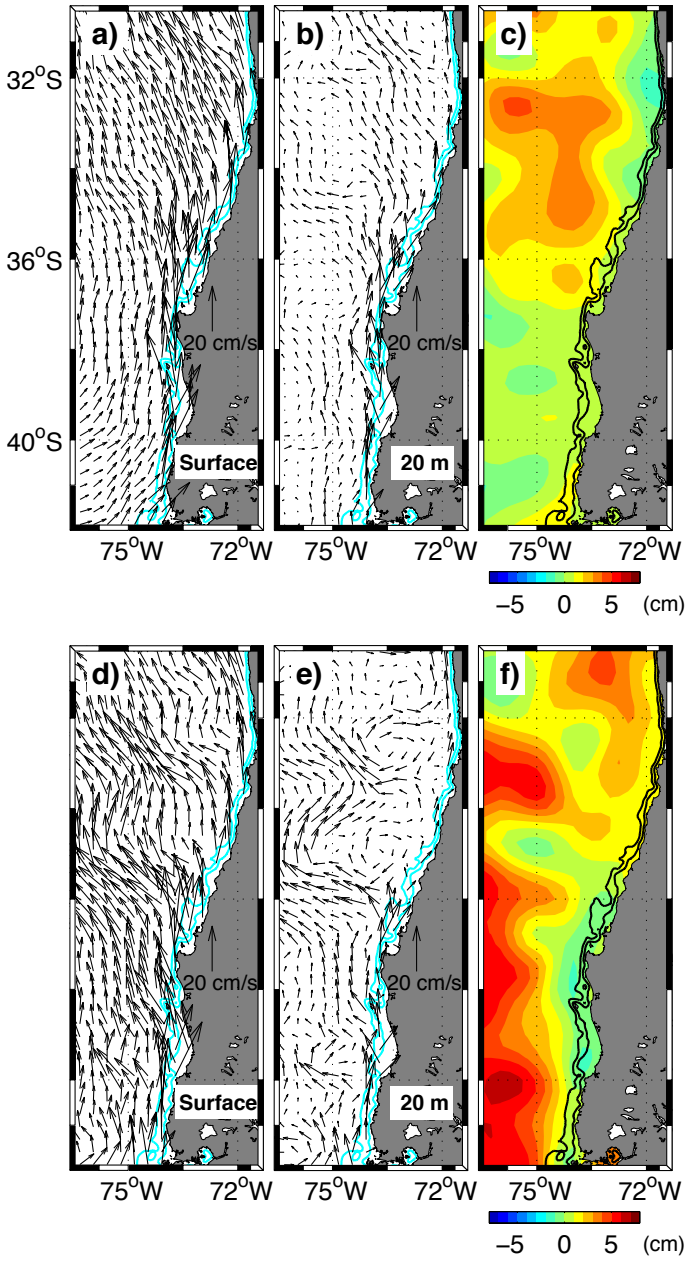

Figure 3.9. Seasonal changes in ocean circulation: average fields from Sep-Nov (a-c) and Jan-Mar (d-f) of the model horizontal velocity at surface (a, d) and 20 m depth (b, e), and sea level anomaly (c, f). The cyan and black contours depict the 100 and 250 m isobaths. All the fields shown are based on data from the period 2002-2008. The seal level anomaly was obtained from satellite AVISO products (www.aviso.altimetry.fr)

4. Spatiotemporal influence of environmental conditions on larval anchovy growth in the southern Humboldt System derived from an Individual Based Bioenergetic Model

4.1. Abstract

Environmental variability strongly determines development and growth in early life stages (ELS) of small pelagic fishes and influences survival and recruitment. However, our understanding of spatiotemporal variability in ELS development/growth and survival, and its connection to environmental patterns is still limited. Here we use an Individual Based Model (IBM) coupled to ocean circulation and lower trophic level models to describe dominant patterns in development, growth, and mortality of ELS of anchovy (*Engraulis ringens*) in the southern Humboldt System. We investigate whether the main spawning season (Aug-Oct) is associated with increased development/growth/survival, considering different scenarios for spawning depth and larval vertical migration over the period 2002-2008. Our results show significant seasonal and intraseasonal variability in stage duration of eggs and yolk-sac larvae (YSL) that lead to changes in early survival. Egg and YSL survival is not maximized during the spawning period, showing a weak connection with late larvae survival. Individual body length at day 30 reveals important differences among scenarios. The slowest growth is derived from individuals seeded at 20 m, as they experience lower zooplankton concentration and temperature than individuals seeded at shallower depths. Individuals seeded at 5 m show strong food limitation when advected far offshore to low prey and warm waters in spring-summer. Ontogenetic migration to 20 m and diel vertical migration, both effective mechanisms to increase coastal retention, decrease individual growth on the shelf. Body length 30-day after spawning peaks in early summer, but secondary maxima are usually found during the main spawning season. Maximum late-larval growth occurs during the early spawning period. Survival appears to increase in the late spawning season (Oct). Our study advances understanding of the interplay of multiple processes that modulate larval

development and growth, and identify the necessity of more observational studies on key aspects affecting ELS fate, like fish vertical distribution, foraging and predation patterns.

Keywords: Anchovy, IBM, bioenergetics, early life stages, growth, mortality, central-Chile, Humboldt System

4.2. Introduction

Recruitment in small pelagic fishes is highly variable and appears to be controlled by environmental factors during the fish early life stages (ELS), since eggs and larvae are more vulnerable to disturbances in abiotic factors, starvation, and predation (Lasker, 1975; Cushing, 1975; Parrish *et al.*, 1983; Cury and Roy, 1989; Bakun, 1996). Body size is a critical factor influencing feeding and predation risk of fish larvae (Werner and Gilliam, 1984). Prevailing hypotheses on fish survival indicate that slow-developing or small larvae are more susceptible to predation than fast-developing or large larvae (Miller *et al*., 1988; Leggett and DeBlois, 1994). Consequently, environmentally driven larval growth may have a great impact on fish abundance (Le Pape and Bonhommeau, 2015). Despite the recognized influence of growth on survival and recruitment variability in small pelagic fish, limited knowledge exists about spatiotemporal patterns of larval growth and their connection with environmental variability.

Peruvian anchovy (*Engraulis ringens*) and common sardine (*Strangomera bentincki*) are the most abundant small pelagic fish from the southern part of the Humboldt Upwelling System, off the central Chile coast (Arrizaga, 1981; Serra, 1983) (Fig. 4.1). Previous studies of this region have documented strong seasonal and intraseasonal variability in coastal circulation that drives significant changes in temperature and plankton abundance (Castro *et al*., 2000; Gonzalez *et al*, 2015; Chapter 2), which likely influence larval growth (Kitchell *et al.*, 1977). Because anchovy and sardine are multiple spawners, capable of spawning year-round, larvae will experience seasonally variable conditions.

Field studies suggest differential growth and survival of anchovy cohorts over the main spawning season in Aug-Oct, associated with intraseasonal changes in upwelling (Castro and Hernandez, 2000; Hernandez and Castro, 2000). The impact of upwelling variability on growth is not straightforward, as the potential positive effect on growth associated with abundant planktonic food in upwelled waters near the coast may be offset by slower growth due to the colder temperatures.

Previous studies hypothesized that the main spawning in late winter and early spring (Aug-Oct) favors retention of ELS of anchovy and sardine over the continental shelf where planktonic food is abundant (Castro *et al.*, 2000; Cubillos *et al.*, 2001). However, the modeling results presented in Chapter 3 showed that that spawning period is not clearly related to nearshore retention. Instead, spawning coincided with peaks in micro- and mesozooplankton concentrations derived from a lower trophic model of phytoplankton and zooplankton, suggesting that a favorable foraging environment that promotes survival of small pelagic fish larvae is key. An evaluation of the coupling between environmental variability and larval growth and survival is needed to determine if the observed spawning seasonality of small pelagic fishes is related to ecosystem dynamics acting on the ELS.

Wisconsin Bioenergetic fish models that simulate growth as a mass balance between consumption, egestion, excretion, and respiration are valuable tools for exploring fish growth dynamics (Kitchell *et al*, 1977; Ney, 1993). The bioenergetic model can be configured within an Individual Based Model (Grimm and Railsback, 2005) to examine patterns in growth and survival emerging from evolving environmental conditions (Xu *et al*., 2013). In this Chapter, we implement an Individual Based Model (IBM) with a bioenergetic component to characterize the spatiotemporal patterns in growth and survival of anchovy larvae under realistic coastal dynamics of the southern Humboldt Upwelling System. The IBM is configured using previous modeling studies of Peruvian anchovy (Xu *et al*., 2013, 2015), Mediterranean anchovy (Politikos *et al*., 2011, 2015),

and California anchovy (Rose *et al*., 2015). A model for *S. bentincki* is not implemented because of the scarcity of information available for this species. However, since *S. bentincki* and *E. ringens* share similar ecological niches and biological traits, the IBM configured here for *E. ringens* could be used to examine also the larval growth dynamics of *S. bentincki*. The main goals of this chapter are: 1) to characterize the larval growth of *E. ringens* in response to its spatiotemporal spawning strategies; and 2) to evaluate plausible larval survival patterns linked to development and growth rates of ELS.

4.3. Model settings

The Individual Based Model (IBM) is an updated version of the model implemented by Batchelder *et al*. (2002) and Batchelder (2006). The IBM simulates development and growth of ELS of anchovy from egg to late larvae (~23 mm total length) exposed to realistic environmental conditions from 2002-2008 derived from a regional ocean model. Stage duration for egg and yolk-sac larvae is temperature dependent. Growth of feeding larvae is a function of prey density and temperature, as well as fish weight, which scales the bioenergetic rates. Potential survival is evaluated as a function of temperature and individual body length. Eggs and larvae are advected through a continuous three-dimensional space. The IBM uses a super-individual (SI) approach (Scheffer *et al.*, 1995) to deal with mortality losses. Each SI represents a large number of identical individuals interacting with an evolving environment. Each SI is quantified by the variable *worth*, which represents the number of surviving individuals, which declines over time due to mortality. The SI approach provides an efficient computation for exploring mortality patterns because it does not require simulating an excessively large number of individuals. The IBM has variables characterizing individuals and environment, which we grouped in six categories: SI, Position, Development, Individual Size, Environment and Bioenergetics (Table 4.1).

The environment that forces growth and survival dynamics is from the output of a three-dimensional, time-evolving, ocean circulation model of the southern Humboldt System, based on the Rutgers Regional Ocean Model System (ROMS, version 3.6; Shchepetkin and McWilliams, 2005). The model has 3 km horizontal resolution, 40 terrain-following vertical layers, bottom topography based on Smith and Sandwell (1997), and zonal and meridional extent of 1,065 and 1,747 km, respectively (Fig. 4.1). The ocean physics model is coupled with a nitrogen-based (units: mmol N m^{-3}) eight-component Lower Trophic Level Model (LTLM), which has two types of phytoplankton (nanophytoplankton, diatom) and zooplankton (micro- and mesozooplankton). Complete details of the coupled model configuration can be found in Chapter 2. All environmental variables are linearly interpolated to the SI location and time at each model time step. An offset of 1°C was added to the temperature in the bioenergetic model to account for the temperature underestimation near the coast (Chapter 2).

4.3.1. Sub-models

The IBM contains four sub-models that consider the following biological processes: Development, Bioenergetics, Movement, and Mortality. Each is described fully below.

Development:

The development sub-model simulates the individual progression from egg to yolk-sac larvae (YSL), and from YSL to feeding larvae. We followed Xu *et al.* (2013) to estimate age at hatching and age at the end of yolk-sac absorption. This procedure is based on the accumulation of a temperature-dependent hourly fractional development rate (Rose *et al.* 1999), derived from temperature controlled laboratory experiments (Pauly, 1987; Llanos-Rivera and Castro, 2006):

$$CDE_n = CDE_{n-1} + \left(24 \cdot 10^{(6.953-4.09 \cdot log10(T_n+26))}\right)^{-1} \cdot \left(\frac{\Delta t}{3{,}600}\right) \quad \text{Eq. 1}$$

$$CDY_n = CDY_{n-1} + (13{,}069 \cdot T_n^{-1.86})^{-1} \cdot \left(\frac{\Delta t}{3{,}600}\right) \quad \text{Eq. 2}$$

where CDE and CDY are the accumulated development of egg and YSL, respectively, T is the experienced environmental temperature (°C), Δt is time step (s), and subscript n indicates step number. CDE is set to 0.0, when the egg is released by the female, and CDY is set to 0.0 at the moment that the egg hatches. A SI transitions to the following life stage once the corresponding accumulated development exceeds a value of 1.0. YSL changes in body length or mass are not simulated in our model. Instead, an initial weight (W_0) is assigned at the beginning of the feeding-larvae stage. From that time on, the bioenergetics sub-model evolves larval weight and length.

Bioenergetics:

Growth in mass

Daily mass growth (G [wet mg of fish day^{-1}]) is a function of total consumption (C, [mg prey day^{-1}]), assimilation efficiency (A, [dimensionless]), and respiration (R [wet mg of fish day^{-1}]):

$$G = \left(A \cdot C \cdot \frac{Cal_p}{Cal_a} - R\right) \quad \text{Eq. 3}$$

where Cal_p and Cal_a are the energy density (cal mg^{-1}) of plankton and anchovy, respectively, and are used to convert the different energy densities of prey and fish. An individual weight decreases when respiration is greater than assimilated consumption. As in Xu *et al.* (2013), the energy density of phytoplankton, zooplankton, and anchovy is assumed to be 0.271, 0.617, and 1.151 cal mg^{-1}, respectively. Assimilation integrates the bioenergetic losses due to egestion, excretion, and specific dynamic action (Hanson *et al.*, 1997), and for larvae can be simulated as a weight-dependent fraction (Rose *et al.*, 2015):

$$A = a_A \cdot (10^{-3} \cdot W)^{b_A} = 0.7061 \cdot (10^{-3} \cdot W)^{0.0467} \quad \text{Eq. 4}$$

where W is the individual weight (wet mg of fish). Simulated assimilation ranged from ca. 0.6 to 0.75. C is the sum of the specific consumption of nanophytoplankton, diatom, microzooplankton, and mesozooplankton, identified with subscripts j = 1, 2, 3, and 4, respectively:

$$C = \sum_{j=1}^{4} C_j \quad \text{Eq. 5}$$

Specific consumption (C_j) is the product of a maximum consumption rate (C_{max}, [wet mg of prey day^{-1}]) and a prey limitation function, $f_c(prey)$ (Rose *et al*., 1999):

$$C_j = C_{max} \cdot f_C(prey) = C_{max}\left(\frac{\frac{PD_j v_j}{K_j}}{1+\sum_{k=1}^{4}\frac{PD_k v_k}{K_k}}\right) \quad \text{Eq. 6}$$

$$C_{max} = a_c \cdot W^{b_c} \cdot f_C(T) = 4.90 \cdot W^{0.45} \cdot f_C(T) \quad \text{Eq. 7}$$

where C_{max} depends on individual weight (W, wet mg) and an asymmetric dome-shaped function of temperature $f_c(T)$ (Thornton and Lessem, 1978), that was parameterized to produce values of 0.20 at 4°C, >0.95 between 14° and 17.5°C, and 0.10 at 26°C; $f_c(prey)$ is a function of prey density (PD_j, wet g m^{-3}), prey vulnerability (v_j), and prey half saturation constant (K_j, wet g m^{-3}). A factor of 1 was used to convert plankton concentration from mmol N m^{-3} to g m^{-3} (Megrey *et al*., 2007). The prey vulnerability coefficients varied as a function of fish length (Fig. 4.2), such that the ontogenetic prey shift of anchovy (Yanez-Rubio *et al*., 2011) could be simulated. Once the vulnerability coefficients were chosen, the half saturation constants were calibrated to obtain reasonable agreement between modeled and observed anchovy length reported by Hernandez and Castro (2000). The calibration was based on model simulations using averages and time evolving conditions of temperature and prey derived from the ocean model. The derived half saturation constants for phyto- and zooplankton components are 1.5 and 1.0 g prey m^{-3}, respectively.

Respiration is adapted from a model by Villavicencio and Muck (1983), and depends on weight and environmental temperature:

$$R = a_R \cdot (10^{-3} \cdot W)^{b_R} \cdot e^{c_R \cdot T} = 2.223 \cdot (10^{-3} \cdot W)^{0.9} \cdot e^{0.096 \cdot T} \quad \text{Eq. 8}$$

Growth in body length

At each time step, a predicted body length (mm) is estimated from wet weight (mg) using a weight-length relationship for anchovy larvae reported by Politikos *et al.* (2011):

$$BL = 10^{(log10(W)+3.1158)/3.57642} \quad \text{Eq. 9}$$

Individual body length is updated to the weight based estimated length only if the body length change is positive ($BL_n - BL_{n-1} > 0$), which implies that shrinking in length is not allowed.

Movement:

SI location is updated every 15 minutes using a Runge-Kutta 4th order advection scheme driven by the 3-D modeled currents. Three types of particle-tracking experiments were performed: 3-D advection only (ADV); advection plus ontogenetic - diel vertical migration (O-DVM); and advection plus ontogenetic vertical migration to 20 m depth (OVM20). The vertical migration scheme was the same as in Chapter 3, with the exception that the migration onset is associated with a larval size threshold instead of a specific day (day 16). Following field evidence reported by Landaeta and Castro (2012), here we defined that individuals start migrating when they reach a size >10 mm.

Mortality:

Specific mortality rates (M, day^{-1}) are similar to those from Xu *et al.* (2013) and Rose *et al.* (2015), but with a temperature dependence function, assuming that mortality increases with temperature (Houde, 1989). The specific daily mortality rates (day^{-1}) at 12°C for eggs, YSL, and feeding larvae are:

$$M_e = 0.60 \quad \text{Eq. 10}$$

$$M_y = 0.16 \quad \text{Eq. 11}$$

$$M_f = (a_m \cdot BL^{-b_m} + c_m) = (0.425 \cdot BL^{-0.14} - 0.21) \quad \text{Eq. 12}$$

where subscripts *e, y,* and *f* stand for eggs, YSL, and feeding larvae, respectively. Mortality at environment temperature is given by:

$$f_M(T) = e^{(\beta \cdot (T-12))} = e^{(0.041 \cdot (T-12))} \quad \text{Eq. 13}$$

$$M_e(T) = M_e \cdot f_M(T) \quad \text{Eq. 14}$$

$$M_y(T) = M_y \cdot f_M(T) \quad \text{Eq. 15}$$

$$M_f(T) = M_f \cdot f_M(T) \quad \text{Eq. 16}$$

4.3.2. Simulations and analysis

We examined the patterns in dispersal, development, growth, and mortality of anchovy ELS that were advected by the 3-D current field. Model simulations were performed with spawning occurring every 3 days, from April of 2002 to November of 2008, implying more than 800 SI cohorts per scenario. The SI cohort contained 1,423 super individuals with an initial worth value of 10^6, which were uniformly released every 3 km over the main spawning region (grey area in Fig. 4.1) and followed for 40 simulation days. Feeding larvae were initialized with a weight and length of 0.166 mg and 4.5 mm, respectively, based on larval size reported by Llanos-Rivera and Castro (2006).

Body length sensitivity to changes in relevant parameters was examined using Individual Parameter Perturbation (IPP). In this procedure, single parameter values were increased or decreased, while all other parameters remained unchanged, and the impacts on mean body length and seasonal pattern were examined. The parameters selected for the IPP analysis were the multiplier and the exponent for allometric effect on consumption (a_C, b_C; Eq. 7) and respiration (a_R, b_R; Eq. 8), half saturation constants (K_j; Eq. 6), the exponent for temperature dependence of mortality (β; Eq. 13), and the allometric effect on mortality (b_m; Eq. 12).

4.4. Results

4.4.1. Growth curves

Estimated body length (BL) as a function of age after hatch agrees well with a von Bertalanffy model fitted by Hernandez and Castro (2000), based on late winter observations of anchovy larvae (Fig. 4.3a). The mean BL growth rate was ~0.49 mm day^{-}

[1]. Mean weight specific growth rates vary from ~0.45 to ~0.10 day^{-1}, which are within the range reported for engraulid larvae by Houde (1989) and Urtizberea *et al*. (2008). The highest variability in daily growth occurs 8 to 9 days post hatching. Modeled BL is not strongly influenced by changes (±10%) in bioenergetic parameters. IPP slightly modifies the annual mean but not the seasonal and intraseasonal patterns. The largest impact is produced by changes in the multiplier and exponent for the allometric effect on consumption, but the variation of BL is lower than 7% (Table 4.2).

4.4.2. Early development

Since a rapid development to less vulnerable stages is thought to produce a positive impact on fish abundance (Cushing, 1990), we examine if modeled temporal variability in egg and YSL development and survival can be linked to patterns in anchovy spawning. Significant differences in age at yolk-sac absorption (i.e. egg plus YSL stage duration) are found among experiments (Fig. 4.5a-c), as the seasonal temperature pattern varies with depth. Because the seasonal cycle of temperature near the surface is opposite to the cycle at 20 m depth, the derived stage duration patterns for ADV05 and ADV20 are opposite. The seasonal variation of age at yolk-sac absorption is about 1.3 days at 5 m and 1.7 at 20 m. The longest stage duration of individuals seeded at 5 m (20 m) depth is in late winter (summer). Strong intraseasonal variability in temperature during spring-summer produces changes of ca. 2 days in the age at yolk-sac absorption. Seasonal and intraseasonal changes in egg and YSL duration strongly modulate early survival (Fig. 4.5e). ADV05 and ADV10 have the highest early survival in late spring and summer, and ADV20 in June (Fig. 4.5f). Therefore, neither fast development of eggs and yolk-sac larvae nor high early survival appears to be connected to the main August to October timing of spawning. A reason for that could be a weak correlation between early and late larvae survival time series. Indeed, the correlation between survival at day 8 and survival at simulation day N (Fig. 4.6) shows a declining trend in all experiments as the simulation progresses, such that at day 40 the correlation is <0.3.

4.4.3. Larval Growth and Survival

Time Series

To describe how changes in prey abundance and temperature modulate larval growth and survival in the multiple cohorts simulated over the period 2002-2008, we derived time series of mean body length, growth rate, and SI worth at day 30 after spawning, mean plankton concentration from the feeding onset to day 30, and mean temperature over the 30-day drift period. Similar patterns are derived at day 40 after spawning, but we show day 30 for consistency with analyses presented in Chapter 3. Figure 4.7 shows the results for all individuals (retained and non-retained). Differences in environmental conditions over the 30-day individual trajectories lead to significant differences in BL at day 30 (BL30) among experiments (Fig. 4.7a-b). BL30 from individuals seeded at 10 m and 20 m have maximum values in summer, whereas BL30 from individuals seeded at 5 m show maxima in late winter (Aug) and early fall (Mar), with a slight decrease in between those months, since more individuals are advected to low prey waters during that period (see Spatial Patterns section). Individuals seeded at 20 m are 2-3 mm smaller than individuals seeded at 5 and 10 m, a consequence of long egg/YSL duration and slow growth. Intraseasonal changes in BL30 are also evident in all experiments, coherent with intraseasonal fluctuations in prey concentration and temperature. Patterns in larval growth rate at day 30 (G30) (Fig. 4.7c-d) show differences with respect to BL30, since the former reflects environmental conditions experienced by late feeding larvae only, whereas BL30 is dependent on conditions experienced throughout all earlier life stages. G30 from individuals seeded at 10 m is the largest from late winter to summer, showing a maximum in August. Similarly, G30 from individuals seeded at 5 m has maximum values in August, but rates markedly decrease in spring-summer. G30 from individuals seeded at 20 m has maximum values during summer and strong deceleration during winter. The interplay among development, growth and temperature determine significant differences in SI worth at day 30 (SI-W30) among experiments (Fig. 4.7d-e). Survival from

individuals spawned at 5 m has the strongest seasonal signal, with the lowest values in spring-summer, linked to slow larval growth and high temperature (due to increased advection of individuals to low-prey, warm waters far offshore). Seasonality of survival derived from individuals spawned at 10 and 20 m is weaker than at 5 m, but its intraseasonal variability is strong. Patterns from O-DVM [20-35] and OVM20 resemble the one in ADV10 but with higher survival during spring-summer.

BL30, G30, and SI-W30 time series and climatologies derived from individuals retained nearshore (Fig. 4.8a-f) differ in some respects from those derived using all individuals (retained and non-retained, Fig. 4.7a-f). BL over the shelf is larger than offshore. The BL offset between ADV20 and the other experiments is smaller, and the BL differences between ADV10 and non-passive experiments (O-DVM and OVM20) are greater. Seasonal changes in BL30 from retained individuals are consistent among experiments, producing maximum BL in summer and minimum in winter. Although the main BL30 maximum is located in summer, secondary BL30 peaks exist during the main spawning period. Interannual variability in Aug-Oct BL is evident, with the smallest size occurring during 2002, a weak El Niño year. G30 from retained individuals (Fig. 4.8c, d) show smaller differences among experiments than those from all-individuals. Retained larvae show growth peaks during the early spawning season (Aug) in all experiments but ADV20. Spring-summer growth rates from retained individuals spawned at 20 m are larger than individuals spawned at 5 m or performing ontogenetic vertical migration. Growth rates from retained individuals spawned at 5 m do not markedly decrease in spring-summer as was found in non-retained individuals. Retained SI-W30 from ADV05 (Fig. 4.8e, f) does not have the strong seasonal signal derived from all-individuals (Fig. 4.7e, f). High survival is obtained from retained individuals during the late spawning season.

Spatial Patterns

Spatiotemporal pattern of mean BL30/G30, SI-W30, and individual density are derived to determine locations favorable for growth, survival and retention of ELS. To visualize this, model outputs were binned on a horizontal 3-km resolution grid. Individual density corresponds to the sum of SI worth over each grid cell. BL30, G30 and SI-W30 show strong cross-shore gradients, with the largest size and survival found over the shelf (Figs. 4.9, 4.10 and 4.11). The intensity of cross-shore gradients increases in late spring and summer and decreases in winter, linked to similar patterns in plankton distribution and temperature (not shown). BL30, G30 and SI-W30 derived from experiments initialized at 5 m (ADV05) and 10 m (ADV10) show increased values north of Point Lavapie (37.5°S), especially in locations where high larval concentration has been reported historically (Soto-Mendoza *et al*., 2010; Landaeta and Castro, 2012), like Gulf of Arauco, Concepcion Bay, and Dichato (Fig. 4.1). SI-W30 from OVM20 has stronger cross-shore gradient compared to ADV10, reflecting a positive impact of vertical migration on survival over the shelf.

Regions with high/low individual density do not necessarily coincide with regions favorable/unfavorable to growth or with large/low SI worth (Fig. 4.12). For example, ADV05 produces the lowest individual density and the largest larvae over the shelf during spring-summer. On the other hand, ADV20 produces the largest nearshore density but the smallest larvae compared to other experiments. The most favorable combination of high individual density, large growth, and high survival is derived from cohorts initialized at 10 m.

4.4.3. Sensitivity Analysis on Mortality

Because the uncertainty in the parameterization of mortality for ELS is large, we examined the response of SI-W30 to the parameter values of temperature dependence and

allometric coefficient for mortality (β and b_M, respectively). The results show that the seasonal survival pattern from ADV05 is mostly determined by temperature dependence on mortality, with the annual signal disappearing at low β values (Fig. 4.13a). Influence of temperature on individual survival is less pronounced in other initial depth scenarios, as individuals do not experience large temperature departures from the reference point of 12°C used in the mortality formulations (Fig. 4.13b). Changes in the allometric coefficient for mortality determine the mean survival level and the intensity of the intraseasonal signal (Fig. 4.14). Small/large b_m implies enhanced/reduced mortality pressure on older larvae.

4.4. Discussion

Individual Based Models of fish coupled to regional circulation models are tools increasingly used in population ecology to examine the interaction of early life stage dynamics with the environment, and to disentangle the processes controlling population abundance (Travers *et al*., 2007; Curchitser *et al*., 2013; Rose *et al*., 2015). Although the uncertainty associated with the parameterization is still important (Miller, 2007; Peck and Hufnagl, 2012), these coupled models provide insight on processes that are not adequately studied in the field, helping to identify critical population dynamics in both space and time (Rose *et al*., 2012). We developed an IBM of the ELS of Peruvian anchovy to document spatiotemporal patterns in egg/larvae development, growth, and mortality off central Chile, and to explore the connection of those patterns to the observed spawning seasonality. We focused on seasonal variability, unlike previous studies on Peruvian anchovy off Peru that dealt with interannual variability on growth and recruitment (Xu *et al*., 2013; 2015).

Several earlier modeling studies that examined the impact of fish dispersal on growth, did not explicitly represent the prey fields. For example, Vikebø *et al*. (2007) derived larval cod growth and survival under the influence of larval vertical positioning. Allain *et al*.

(2007) and Catalan *et al.* (2013) linked observed growth rates to modeled physical factors, including temperature and stratification. However, evidence suggests that food limitation of fish larvae/juveniles can be strong (Le Pape and Bonhommeau, 2015), requiring spatiotemporal representation of prey fields and bioenergetic models to understand better growth dynamics. Our results show that larval vertical positioning strongly influences both dispersal patterns and larval growth, as horizontal and vertical gradients in plankton distribution determine prey availability for feeding larvae. We found a balance between larval growth and coastal retention for individuals initialized at 10 m. Ontogenetic migration to 20 m and O-DVM [20-35] decreased growth on the shelf (compared to ADV10), but significantly increased retention and survival, potentially favoring the formation of individual aggregations nearshore. The impact of OVM20 and O-DVM [20-35] off the shelf was opposite to that on the shelf, reflecting between region differences in the vertical distribution of prey and temperature.

We recognize that more complex scenarios of vertical migration need to be evaluated, in which late larvae can actively select vertical positioning following certain environmental clues. For example, Rose *et al*. (2015) simulated active vertical positioning of larval anchovy driven by potential growth and optimal temperature; the highest larval abundance were found at 10-15 m depth, linked to enhanced zooplankton abundance at that depth range. This is consistent with our results showing fast larval growth in individuals spawned at 10 m, as they remained close to that depth range over the simulation period. Rose *et al*. (2015) approach did not produce diel vertical patterns, because modeled plankton did not perform DVM, and neither diel foraging nor predation risk cycles were included in the model. Those aspects were examined in a modeling study on larval cod by Vikebø *et al*. (2007), who showed that DVM emergence is possible from variable light conditions influencing predation risk and larval foraging. Further observational studies to parameterize this last approach will be required for anchovy larvae.

Prevailing hypotheses of fish population dynamics indicate that rapid development through the egg and larval stages favors fish survival (Houde, 1987; Miller *et al*., 1988). An example of this positive connection is the Norwegian herring, which recruitment appears to be positively linked to early hatching (Husebø *et al.*, 2009). We explored if fast development in anchovy ELS was a factor determining spawning period, but the model results did not support this hypothesis. Instead, age at yolk sac absorption derived from ADV05 and ADV10 reached maximum values (e.g., slowest development) during the early spawning season. A relatively weak coupling between early and late larval survival could explain this result, as suggested by the decreasing coherence in SI worth as the simulation period progresses. Indeed, a negative correlation between time series of SI worth at day 8 and 30 is derived from individuals spawned at 5 m. That is consistent with the study of Xu *et al.* (2015), which obtained an inverse relationship between egg/YSL survival and feeding larval survival. This is because warm (cold) waters have low (high) prey abundance, implying that fast (slow) egg/YSL development is followed by slow (fast) growth of feeding larvae. The non-coherence between early and late survival could suggest a weak link between egg abundance and recruitment. However, temporally variable egg production, which was not considered in our model as initial SI number and worth were the same in all simulations, could determine changes in recruitment and adult abundance. Indeed, Fiechter *et al.* (2015) obtained a strong correlation between modeled egg production and abundance of one-year-old anchovies off California.

In Chapter 3 we found favorable conditions for larval foraging during the main spawning period, with peaks in microzooplankton concentration during the early spawning season. Seasonal coupling between prey and feeding-larvae phenologies are expected to increase larval growth and survival (Cushing, 1990). We examined if those favorable conditions in prey lead to high growth of late larvae, using BL30 and G30 as growth indices. BL30 is controlled by processes occurring over the 30-day simulation period, including egg/YSL development, as the latter determines when the feeding-larva stage starts. Instead, G30 is a metric that reflects late-larvae growth only. Although the period that maximizes BL30

is summer, secondary BL30 peaks occurred during the main spawning season. In addition, most experiments produced the fastest late-larvae growth during the early spawning season. Those findings are consistent with the hypothesis that the spawning period is favorable for larval growth (Cubillos *et al*., 2001).

Our model scenarios produce maximum survival over the shelf in the late spawning period. This result agrees with some observational evidence that showed increasing anchovy larval survival as the spawning season progresses (Castro and Hernandez, 2000). However, we recognize that our limited knowledge of the factors modulating mortality, like fish starvation threshold, physical/chemical tolerance range, and predator abundance, preclude an accurate estimation of survival patterns. Mortality is one of the most challenging processes to simulate properly, and studies usually do not address the sensitivity analysis of the mortality assumptions (Peck and Hufnagl, 2012). Our sensitivity analysis on mortality revealed that temperature dependence was needed to generate the annual signal in survival from ADV05. Inclusion of temperature dependence on mortality is supported by observations that show increased predation on anchovy by gelatinous predators in warm offshore waters (Castro *et al*., 2000). Using a dome-shaped function for temperature dependence on mortality instead of an exponential function may be suggested, but a negative impact of low temperature on survival is implicitly considered in the model, since low temperature increases the duration that eggs and YSL are exposed to the highest mortality rate. An explicit representation of predator dynamics may be required to get better estimates of survival patterns in future studies, such that mortality can be connected to seasonal changes in predator abundance. This may be particularly important, since changes in predator pressure have been suggested as an explanation of differences between phenologies in larval growth and prey abundance (Buckley and Durbin, 2006). The “maternal influence” on egg traits (size, chemical composition) and its impact on ELS survival is another aspect that could be represented, since observations suggest changes in egg size and hatching success as the main

spawning season progresses (Castro et al., 2009). These were beyond the scope of our study.

Table 4.1. Main variables of the Individual Based Model

Type	Variable	Units or Categories	Symbol	Dependence
SI	Worth	Number of individual		M
	Age	day		
	Mortality	day^{-1}	M	Stage, BL, T
Position	Longitude, Latitude	Degrees	lon, lat	u, v
	Horizontal Location	grid units or m	x, y	u, v
	Depth	m	z	w, larval swimming
	Bottom Depth	m		lon, lat
Development	Stage	Egg, yolk-sac larvae, feeding larvae		DV
	Fractional development	Fraction [0-1]	DV	Temperature
Individual Size	Weight	mg of fish	W	$\Delta W/\Delta t$
	Body Length	mm	BL	$\Delta W/\Delta t$, W
Environment	Horizontal currents	$m\ s^{-1}$	u, v	grid units, z, time
	Vertical current	$m\ s^{-1}$	w	grid units, z, time
	Prey Density:			
	Nanophytoplankton (j=1)	mmol N m^{-3} (*)	PD_1	grid units, z, time
	Diatom (j=2)	mmol N m^{-3} (*)	PD_2	grid units, z, time
	Microzooplankton (j=3)	mmol N m^{-3} (*)	PD_3	grid units, z, time
	Mesozooplankton (j=4)	mmol N m^{-3} (*)	PD_4	grid units z, time
	Temperature	°C	T	grid units, z, time
Bioenergetics	Growth	mg fish day^{-1}	$\Delta W/\Delta t$	C, A, R
	Consumption	mg prey day^{-1}	C	v_j, K_j, PD_j, T, W, BL
	Respiration	mg fish day^{-1}	R	T, W
	Vulnerability coefficient prey type *j*	Fraction [0-1]	v_j	Prey type, BL

(*) Coefficient for the conversion of plankton concentration from mmol N m^{-3} to gram of prey m^3 is 1 (Megrey *et al*., 2007)

mg of prey and fish are in wet weight.

Table 4.2. Mean body length sensitivity analysis to changes in bioenergetics parameters.

Parameter	Symbol	Value	Mean impact on BL at day 30 (%)
Multiplier for allometric effect on C	a_C	4.90	(-5, 6)
Exponent for allometric effect on C	b_C	0.45	(-4, 5)
Multiplier for allometric effect on R	a_R	2.23	(1, -1)
Exponent for allometric effect on R	b_R	0.90	(-3, 2)
Half saturation constants for phytoplankton	K_1 & K_2	1.50	(1, -1)
Half saturation constants for zooplankton	K_3 & K_4	1.00	(3, -2)

The first and second numbers in the fourth column are the BL variation associated with a 10% decrease and increase of the parameter value reported in the third column, respectively

C: Consumption; R: Respiration

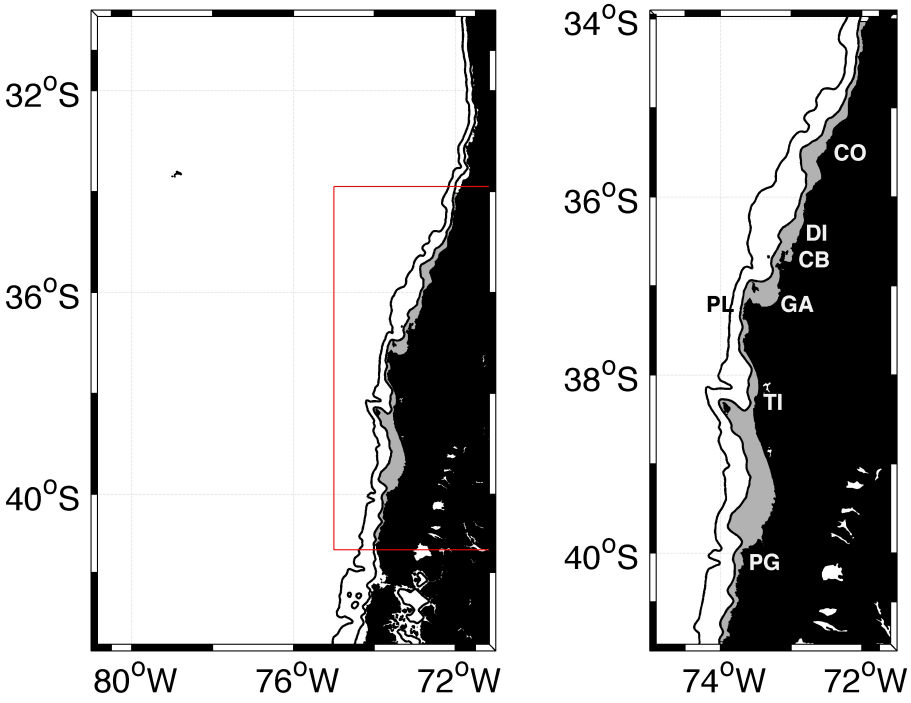

Figure 4.1. Study region. Left. Ocean circulation model domain showing the seeding region in light gray; red box demarks the right panel area. Right. Detailed seeding region with locations of Constitucion (CO), Dichato (DI), Concepcion Bay (CB), Gulf of Arauco (GA), Punta Lavapie (PL), Tirua (TI), and Punta Galera (PG). The 100 and 500 m bathymetric contours are indicated in both panels.

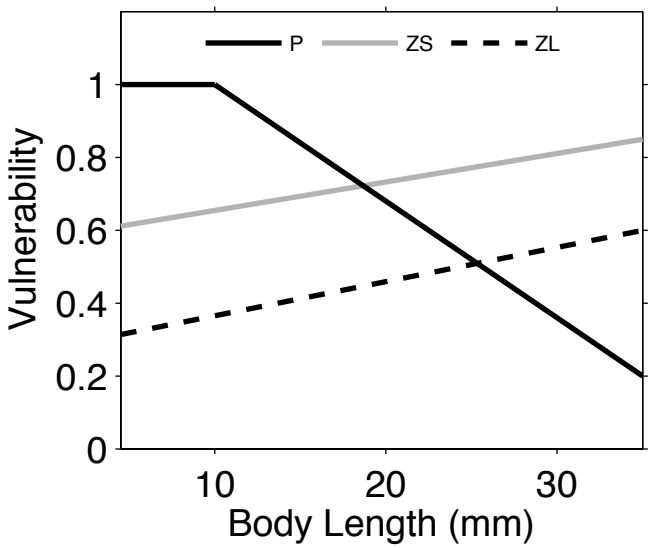

Figure 4.2. Prey vulnerability coefficients (v_j). Vulnerability is a function of larval body length and plankton type: phytoplankton (P), microzooplankton (ZS), and mesozooplankton (ZL).

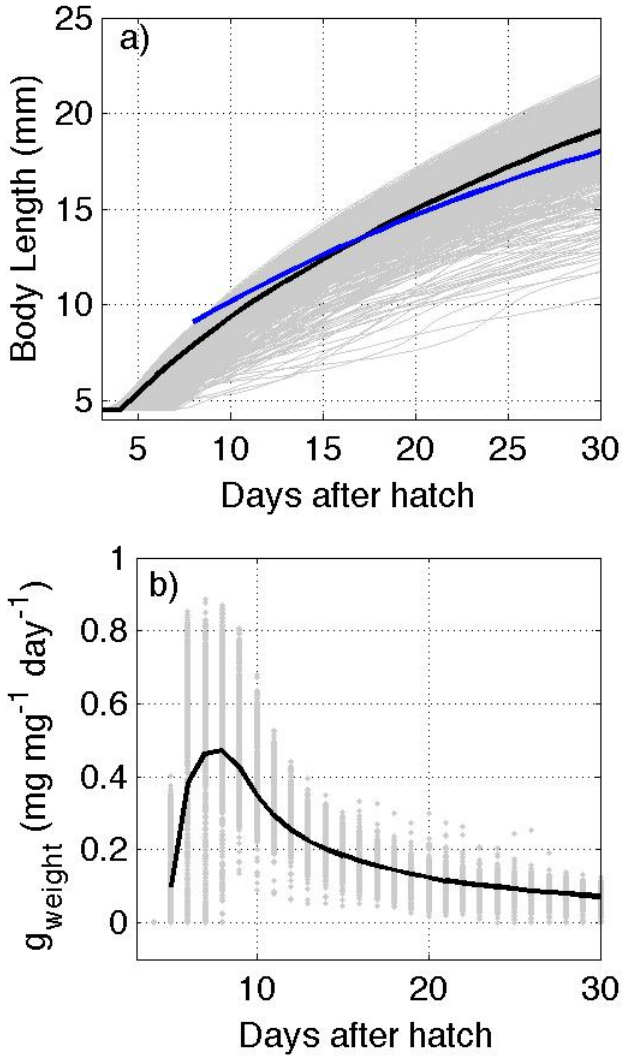

Figure 4.3. Modeled body length (top panel) and specific weight growth rate (*g*, bottom panel) as a function of days after hatch. IBM estimates were generated from simulation initialized at 10 m depth on Aug 1 of 2005. Black solid lines depict mean value for a given day. Blue line in left panel corresponds to a von Bertalanffy growth model by Hernandez and Castro (2001) derived from field observations.

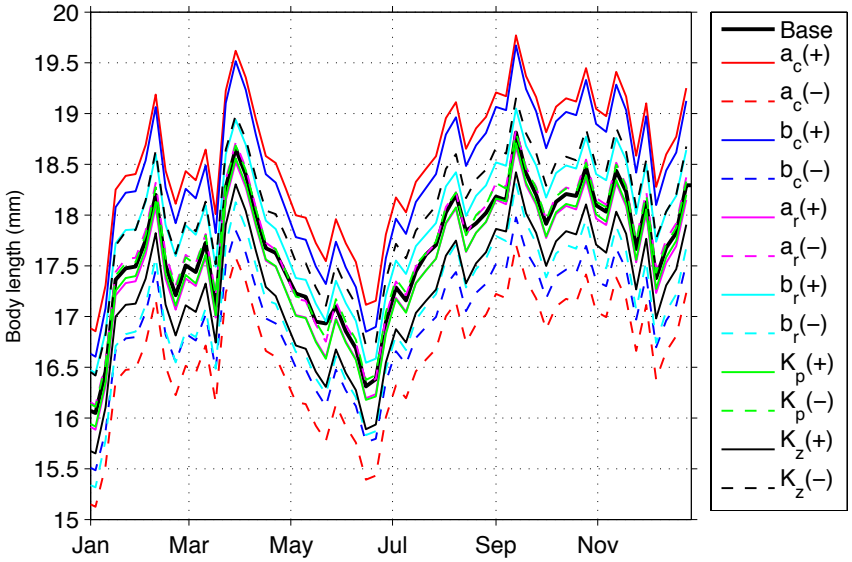

Figure 4.4. Sensitivity of body length at day 30 to bioenergetic parameters. Results are derived from ADV05 during a representative year (2005). Parameter names are indicated in Table 4.2. Plus/minus signs indicate 10% increase/decrease in the parameter value.

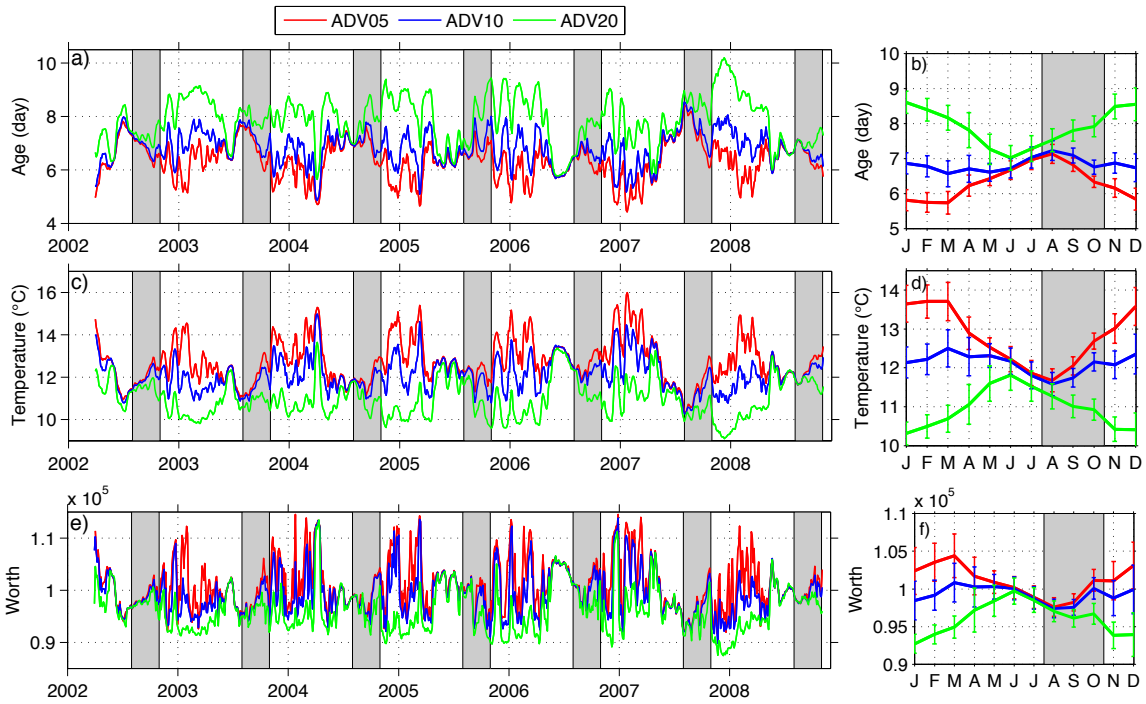

Figure 4.5. Stage duration, temperature, and early survival. Temporal variability of average stage duration, temperature and early survival through egg and yolk-sac larvae stages at initial depths of 5 (red), 10 (blue) and 20m (green). Left panels show 3-day time series of a) mean age at yolk-sac absorption, c) mean temperature, and e) mean SI worth at day 8. Right panels (b, d, f) are monthly climatologies derived from the 3-day time series. Error bars show 1 SD. Gray shaded area indicates main anchovy spawning period.

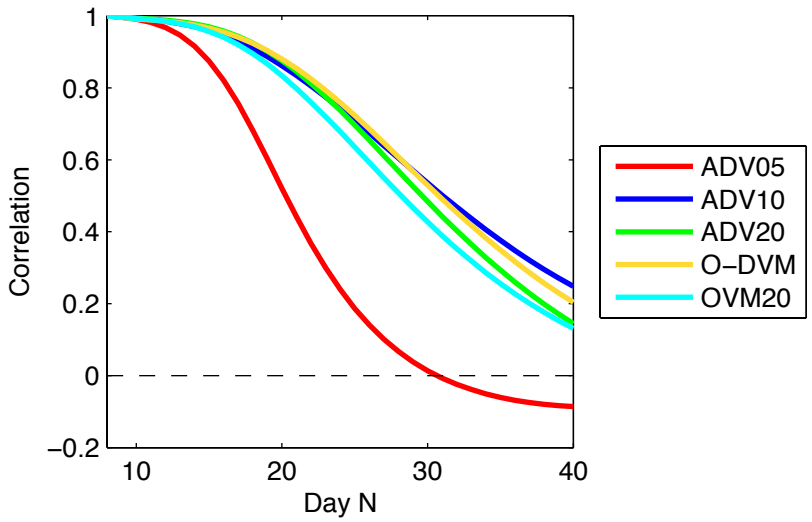

Figure 4.6. Correlation coefficient between the mean SI worth time series at day 8 and day N for the considered experiments.

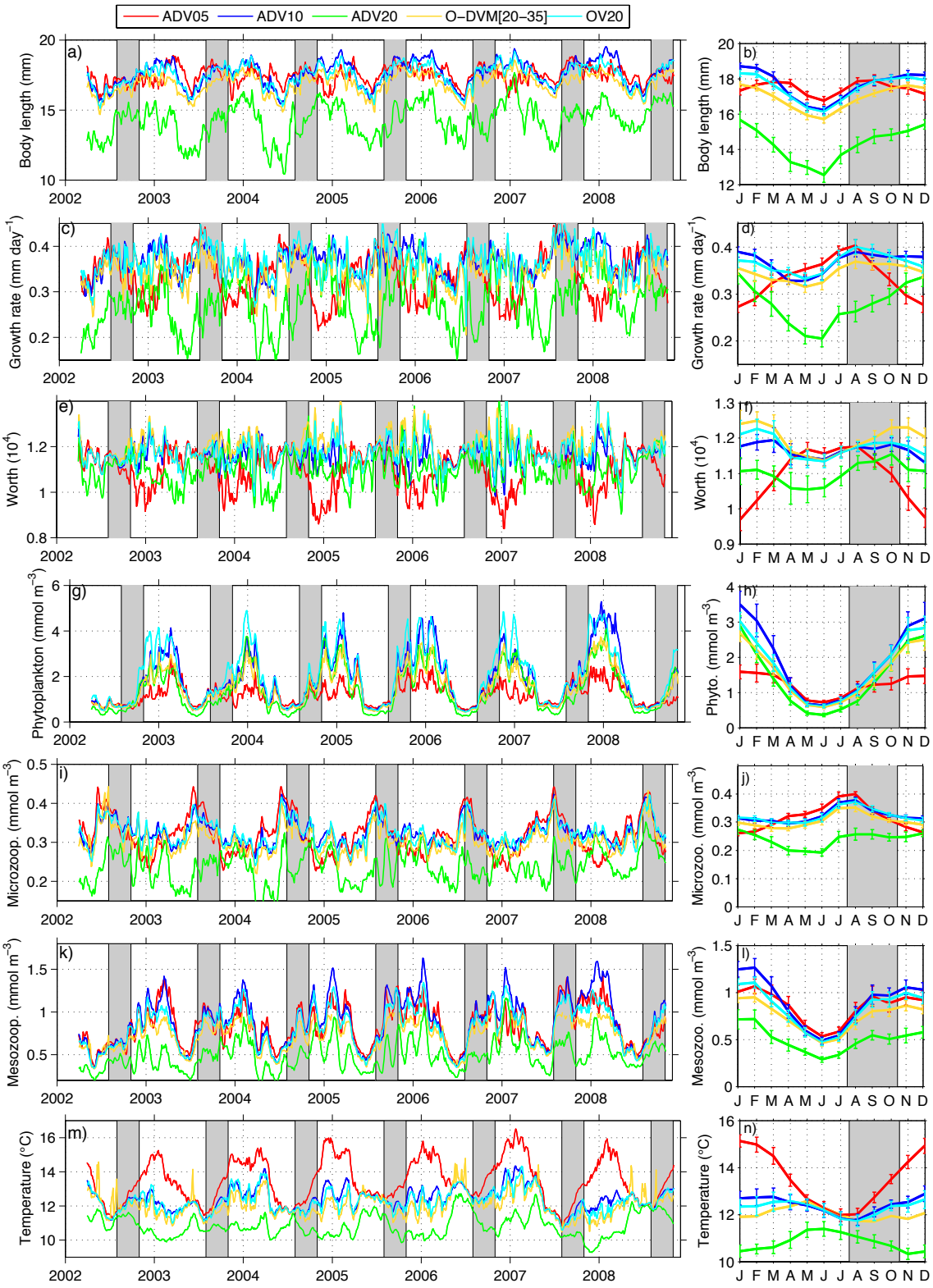

Figure 4.7 (legend on next page)

Figure 4.7 (previous page). Body length, growth rate, survival (worth), and environmental variability derived from all individuals (retained and non-retained): temporal variability of mean body length (a-b), mean growth rate (c-d), and mean super individual worth (e-f) at day 30 after spawning; g-h), mean phytoplankton concentration derived from individual trajectories over the larval feeding period; i-j) and k-l) as in g-h but for microzooplankton and mesozooplankton, respectively; m-n) mean temperature over simulation period. Error bars in right panels show 1 SD. Gray shaded area indicates main anchovy spawning period.

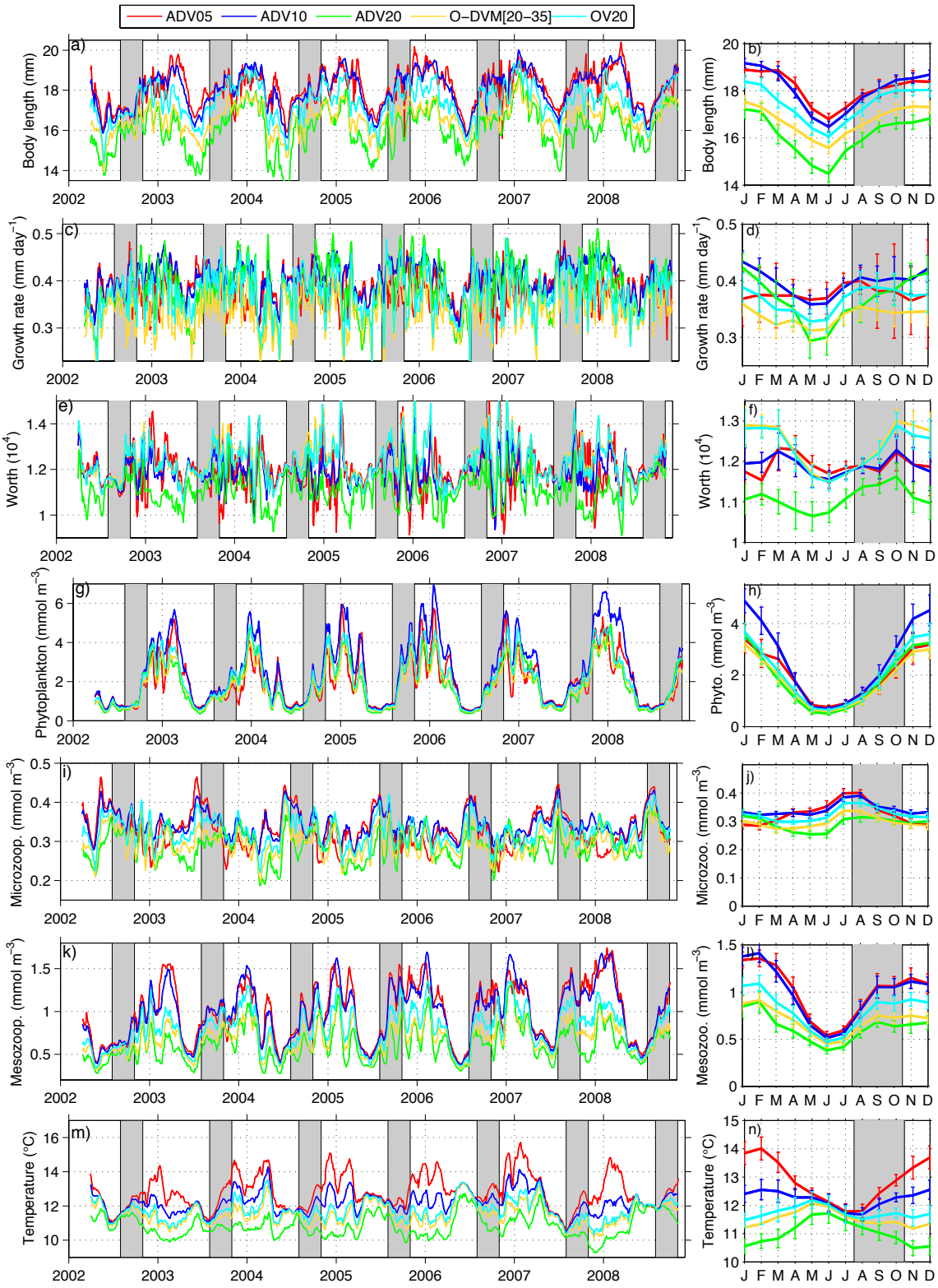

Figure 4.8. As in Fig. 4.7 but for individuals retained nearshore only.

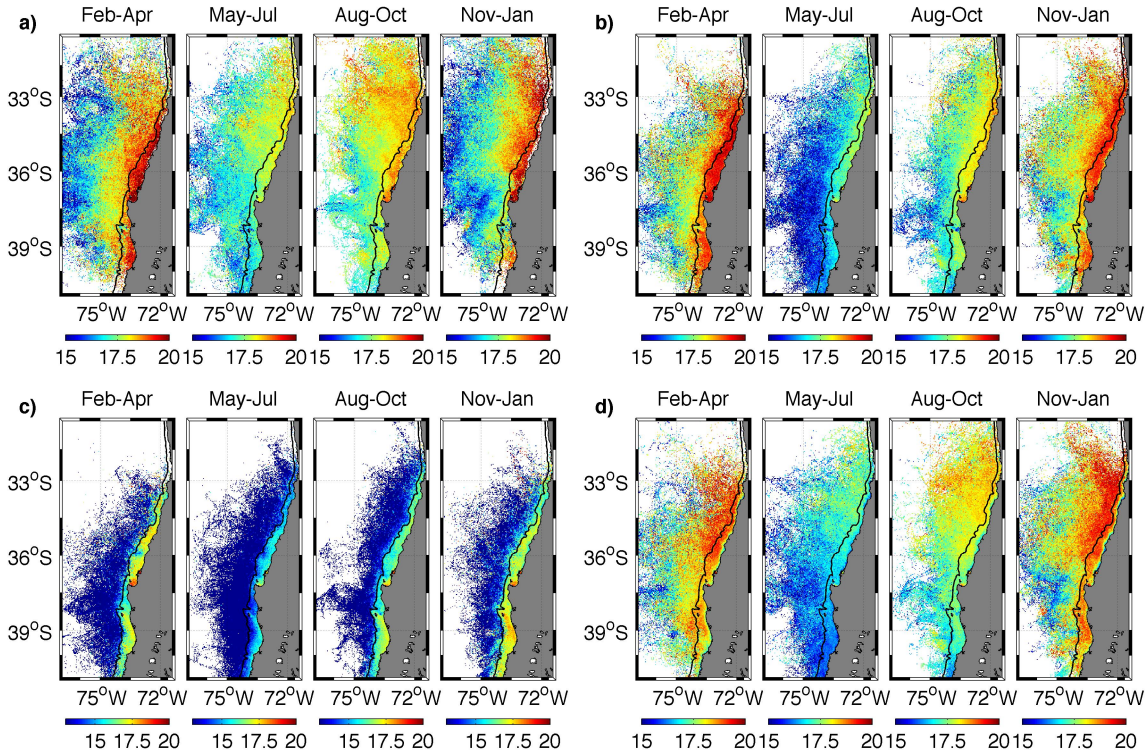

Figure 4.9. Seasonal patterns of mean (2002-2008) individual body length at day 30 after spawning for a) ADV05, b) ADV10, c) ADV20, and d) OVM20. Estimates of mean body length are weighted by SI worth. Black contour depicts the 500 m isobath. Note that the colorbar in panel c) shows a different range than in other panels.

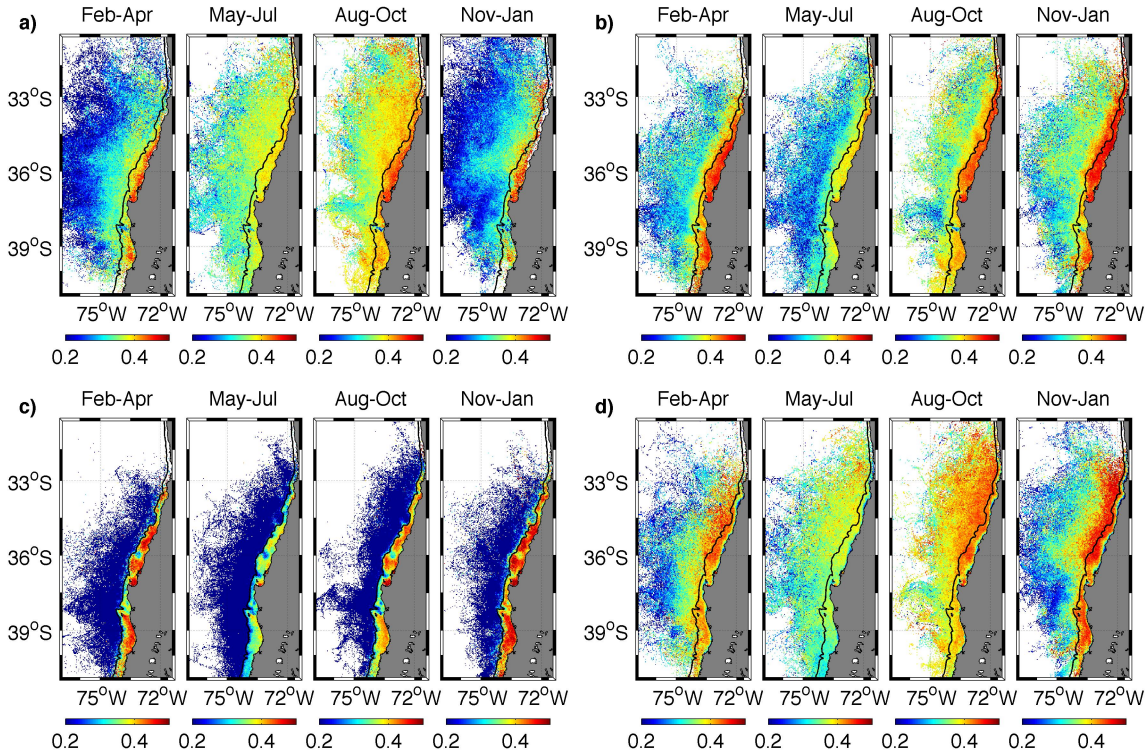

Figure 4.10. Seasonal patterns of mean (2002-2008) individual growth rate at day 30 after spawning for a) ADV05, b) ADV10, c) ADV20, and d) OVM20. Estimates of mean growth rate are weighted by SI worth. Black contour depicts the 500 m isobath.

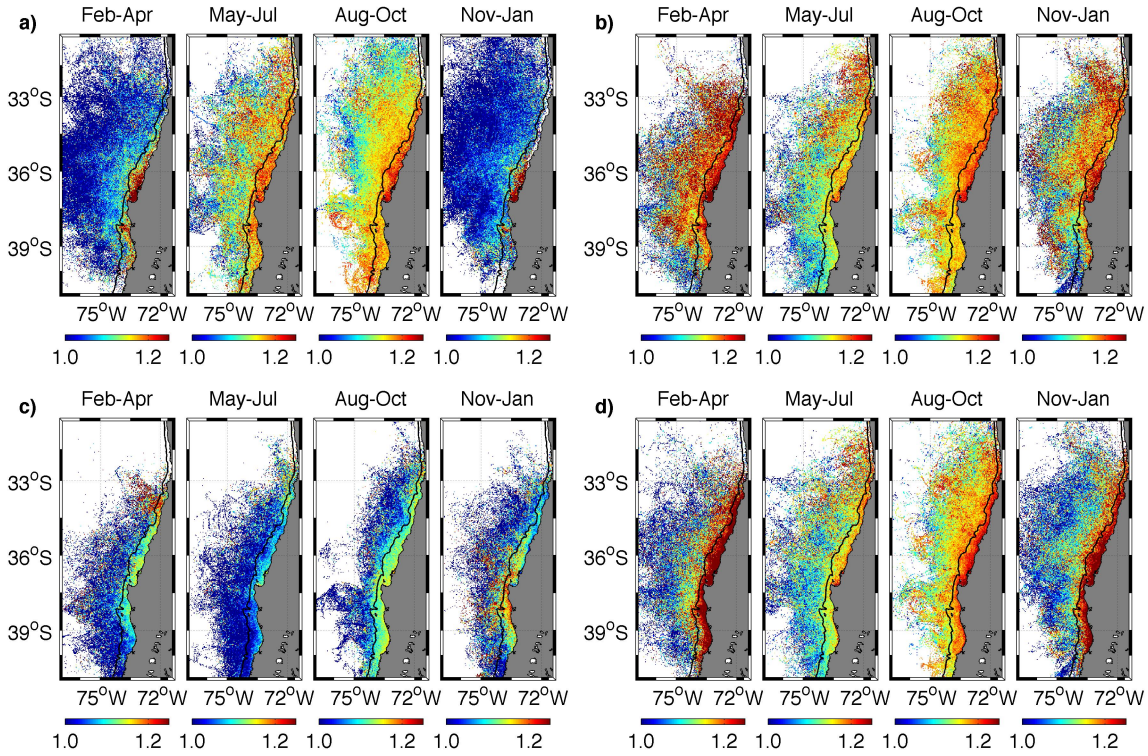

Figure 4.11. Seasonal patterns of mean (2002-2008) SI worth at day 30 after spawning for a) ADV05, b) ADV10, c) ADV20, and d) OVM20. Black contour depicts the 500 m isobath. SI worth is in unit of 10^4 individuals. SI worth at spawning was 10^6.

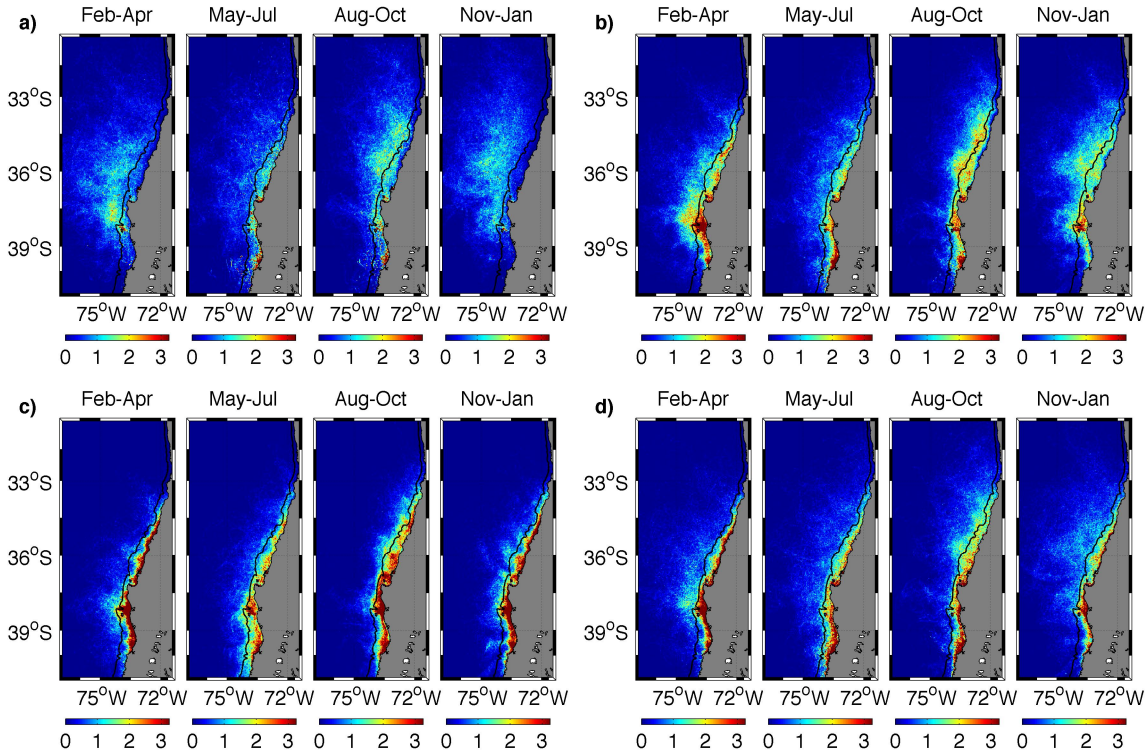

4.12. Seasonal patterns of mean (2002-2008) individual density at day 30 after spawning for a) ADV05, b) ADV10, c) ADV20, and d) OVM20. Black contour depicts the 500 m isobath. Density unit is 10^3 individuals per grid point.

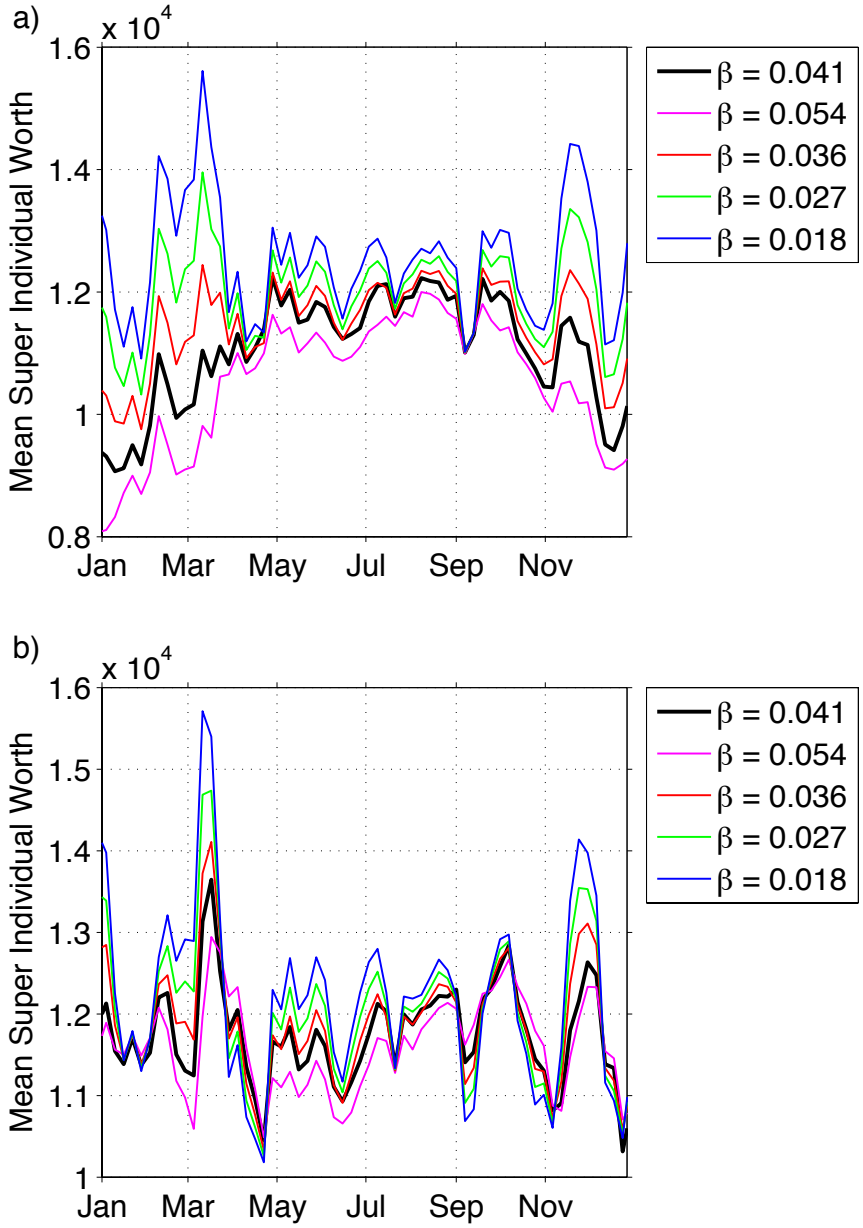

Figure 4.13. Sensitivity of mean SI worth to the exponent of the temperature dependent mortality (Eq. 13). Results derived from a) ADV05 and b) ADV10 during a representative year (2005).

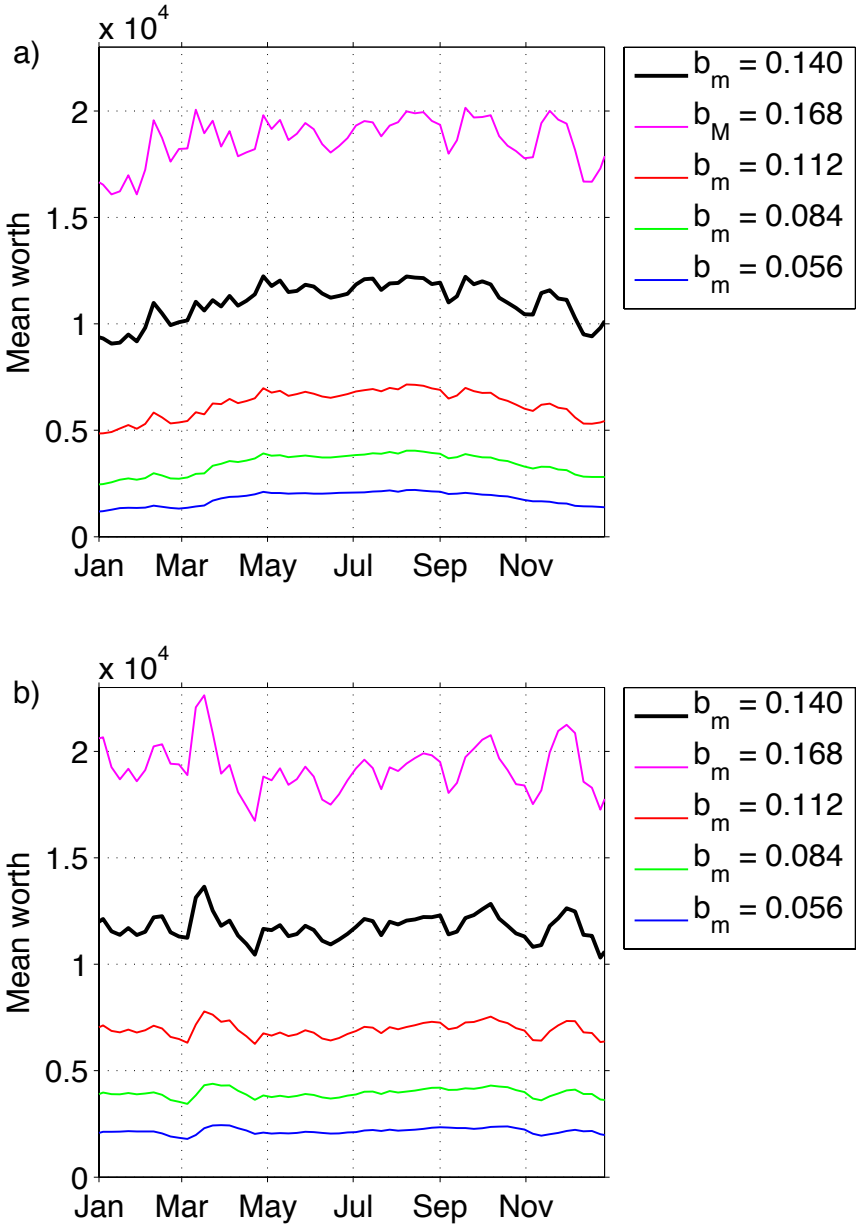

Figure 4.14. Sensitivity of mean SI worth to the allometric exponent effect on mortality (Eq. 13). Results derived from a) ADV05 and b) ADV10 during a representative year (2005).

5. Concluding Remarks

Intensive spatial and temporal sampling of the ocean, including the physics and multiple trophic levels, in order to understand the coupled biophysical processes that control the dynamics of marine populations like zooplankton or fish, is rarely feasible as the manpower and ships required are often beyond the resources available. Although field sampling of everything, everywhere and at all times would be preferable, it is not feasible. However, coupled ocean circulation and lower trophic level models that simulate physics, nutrients, and plankton dynamics at multiple time scales, are capable of revealing complex interactions between marine biota and the climate system. Since the role of environmental variability as a main driver of changes in abundance and distribution of marine populations is widely accepted (e.g. Checkley *et al*., 2009), marine ecologists and fisheries scientists have become increasingly interested in using coupled models to examine fish population dynamics (Megrey *et al*., 2007; Rose et al., 2010). This has led to the development of Eulerian-Lagrangian modeling approaches that explicitly represent spatiotemporal dynamics of prey and individual fish (Curchitser *et al*., 2013). In this dissertation, we use such a model to explore the coupling between reproductive strategies, including the dynamics of the early life stages (ELS), of the small pelagic anchovy and common sardine and coastal upwelling ecosystem dynamics off central Chile.

Although high-resolution ocean circulation and lower trophic level models have been widely used to examine ocean and plankton dynamics in upwelling systems, few of those models were configured for the southern Humboldt System (e.g. Baird *et al*., 2007). The adequacy of the boundary condition and forcing products that provided realistic circulation, hydrography, and plankton dynamics in the southern Humboldt system was one of the main challenges of the Eulerian-Lagrangian approach. Despite this challenge, our regional ocean model reasonably reproduced the predominant spatiotemporal variability in coastal circulation and plankton biomass off central Chile. Chapter 2 reported a relevant intraseasonal variability in upwelling (~50 day) and associated biomass and composition of plankton. Intraseasonal changes in plankton are strongly

correlated to alongshore-coastal wind disturbances linked to Madden Julian Oscillations, a large-scale atmospheric pattern that appears to influence ocean circulation and climate worldwide (Madden and Julian, 1972). The intraseasonal patterns exemplify the model's ability to reproduce realistic patterns in this coastal upwelling ecosystem. We recognize there may be some bias in the modeled ocean circulation linked to wind overestimation nearshore, as satellite winds do not resolve properly the coastal wind drop-off (Renault *et al*., 2012), which may overestimate upwelling and underestimate sea temperatures and retention in the nearshore regions. An increased spatial resolution of the ocean model (0.5 or 1 km horizontal), along with an increasing spatiotemporal resolution in the atmospheric products used to force the model (e.g. hourly winds), are required for a better representation of sub-mesoscale processes and sub-synoptic variability that might be important for ichthyoplankton retention nearshore. Other concerns are the incorporation of river discharge and tides, neither of which were included in the current model. Freshwater inflow could affect plankton production (by increasing vertical stratification and/or adding nutrients) and favor concentration of ELS (generating frontal structures), and tides could increase mixing over the shelf and influence the distribution of ELS nearshore. However, we are confident that those biases and potential shortcomings of the model do not strongly impact our main conclusions. This study should be considered as a initial step toward assessing coastal retention in small pelagic fish in the southern Humboldt Current.

The time evolving ocean circulation model was used as a laboratory to examine the physical and ecological dynamics impacting the fate of ELS. Instead of addressing interannual variability in historical observations of recruitment, we focus on the factors that determine reproductive success in small pelagic fish by documenting the dominant patterns in ELS dispersal, coastal retention, development and growth, and by examining plausible scenarios of fish survival. Despite the enormous ecological and economical importance of *E. ringens* and *S. bentincki* in the Humboldt System, many aspects of the biology, distribution, and behavior of anchovy and sardine ELS remain poorly observed. Previous studies have documented the critical influence of vertical location on

ichthyoplankton dispersal (e.g. Fiksen *et al*., 2007; Brochier *et al*., 2008). Ichthyoplankton buoyancy, larval swimming, and ocean circulation determine vertical distribution of ELS. There are no observational studies reporting egg or larval buoyancy in Peruvian anchovy and common sardine in the Humboldt System. There is some evidence of active vertical positioning of late larvae (Landaeta and Castro, 2012), but still the underlying mechanisms behind the patterns are not well understood. Uncertainties about the vertical distribution of eggs and larvae led us to develop scenarios of initial spawning depth and vertical migration of late larvae, which allowed examination of the fate of ELS under several plausible dispersal patterns.

Variations in the initial spawning depth and vertical migration of late larvae caused substantial changes in the long-term average retention as well as in the seasonal pattern of retention. For example, north of Point Lavapie, individuals seeded at 5 m have a low probability of being retained nearshore in seasons other than winter, whereas eggs seeded at 20 m showed maximum retention in summer. Seasonal changes in the vertical current shear and mesoscale variability were important to explain those seasonal patterns. Vertical migration was shown to be an efficient mechanism for increasing nearshore retention only when larvae avoid the most offshore advective surface layer. This result is in agreement with previous studies on plankton dynamics (Carr *et al*. 2008, Drake *et al*., 2013). In addition to those differences in retention, results derived from the Individual Based Model (IBM) showed that initial spawning depth and larval vertical migration significantly influences larval growth, as the prey concentration experienced by individuals differ among dispersal trajectories. High retention derived from individuals spawned at 20 m did not translate to favorable condition for larvae, since the colder temperatures and reduced prey availability slowed development and growth, and lead to increased mortality. High retention and rapid growth are derived for individuals seeded at 10 m. Individuals that performed vertical migration increased shelf retention and survival at the cost of decreased growth. Our studies highlight the role of active vertical positioning as a mechanism to increase retention and favor larval aggregation over the shelf. Future studies will need to explore other factors driving vertical migration, as most

likely larval vertical positioning is influenced also by distribution of prey and predators. A mechanistic modeling approach, which explicitly simulates the interaction among larvae, prey and predators under varying conditions of light, might generate more realistic larval vertical behavior (e.g. Vikebø *et al*. 2007), with potential implications on nearshore retention, growth and survival. Additional observational studies are needed to parameterize that type of model.

Advection to unfavorable habitats (Hjort, 1914; Sinclair and Illes, 1989), starvation (Cushing, 1990) and predation (Miller et al., 1988; Leggett and DeBlois, 1994) are the three main mechanisms controlling ELS survival. Chapter 3 examined Hjort hypothesis of larval drift to favorable/unfavorable habitats, linking habitat suitability to a bathymetric criterion (the 500 m isobath). The approach was used to identify relevant dispersal and connectivity dynamics that promoted retention in prey-rich locations. The main spawning locations (shoreward of the 100 m isobath) favored coastal retention, and the main spawning timing (Aug-Oct) was only partially associated with high retention. This latter result did not support the hypothesis that postulated a coupling between coastal retention and spawning phenologies. Instead, we found that the principal spawning season favored connectivity between the southern spawning region and the main nursery region north of Point Lavapie. In addition, Chapter 3 showed support for Cushing's match-mismatch hypothesis of coupling between fish spawning and plankton production phenologies. The negative impact of poor feeding conditions, including increasing mortality on slow developing/growing individuals, was addressed in Chapter 4. Shortest egg and YSL duration, and therefore lowest mortality, did not occur during the main spawning period. This somewhat surprising result appears to be related to the weak correlation between early and late larvae survival, suggesting that egg abundance is a weak predictor of fish recruitment. However, we recognize that interannual changes in egg production could impact adult abundance (e.g. Fiechter *et al.*, 2015). This aspect was not included in the model, since the initial SI number and SI worth was the same in all simulations. Advection of ELS to unfavorable offshore locations led to poor prey conditions, decreased larval growth, and higher temperature, all variables that increased

individual mortality. Maximum larval size 30 days after spawning did not occur during the main spawning period but during summer. However, increased prey concentrations also promoted rapid larval growth during the main reproductive period, consistent with Cubillos *et al*. (2001) hypothesis. Survival over the shelf showed a weak seasonal pattern, with a maximum during the late spawning season (Oct).

Our study provides insights on ocean and early life stages dynamics that could be considered in future observational studies and fishery management. A relevant aspect is the intraseasonal upwelling variability, which could have a strong influence on dispersal and growth of larvae. The potential coupling between spawning intensity and intraseasonal upwelling oscillations requires further examination, since reproductive traits (fecundity, egg size) of adult females appear to respond quickly (on order of weeks) to environmental factors such as temperature and food (Claramunt *et al*., 2012). To properly examine the intraseasonal dynamics we need a sampling frequency of ~1 or 2 weeks, increasing the typical monthly resolution of fishery monitoring. Also requiring further investigation is how disturbances in spawning phenologies will impact the reproductive success of small pelagic fishes. Changes in spawning phenology can be triggered by changes in age/size population structure, since young/small fishes have lower fecundity and shorter spawning periods than older/larger fishes (Claramunt *et al*., 2013). A dominance of slow growing fish due to overfishing of fast growing fish may explain a delayed peak in the main reproductive period of common sardine during the last decade (Cubillos *et al*., 2013). Changes in spawning phenologies could also result from disturbances in environmental patterns, such as the predicted increase in coastal upwelling due to climate change (Garreaud and Falvey, 2009), which might increase the advective losses of larvae during spring-summer, impacting negatively on individuals spawned during the late spawning season. Since changes in spawning phenology induced by fishing pressure and environmental variability could have opposite sign, we might expect increasing vulnerability to overfishing in both sardine and anchovy populations.

The IBM we used provided a framework to examine the dynamics that influence the reproductive success of small pelagic fish. However, the limited information available about the processes and variables influencing growth, and especially mortality related parameters creates uncertainty in our model estimates of ELS survival. Explicit representation of predator abundances and dynamics is needed to understand seasonal and intraseasonal mortality rates that strongly determine survival. In this study we focused on describing egg and early larval dynamics. The logical next step would be extending the study through the late larval period to recruitment to the juvenile stage. This would require using a more complex movement sub-model that incorporates both horizontal and vertical late larval and juvenile swimming. We consider the IBM used in this study as a first step toward the development of more complex models, which will consider more mechanistic approaches to simulate foraging, predation, and movement, including the explicit representation of species interactions. The models described here make an important contribution to understanding the factors that influence reproductive success in marine populations, and prediction of population responses to environmental and human disturbances.

6. Bibliography

Agostini, V.N., Bakun, A., Francis, R.C. (2007) Larval stage controls on Pacific sardine recruitment variability: high zooplankton abundance linked to poor reproductive success. *Mar. Ecol. Prog. Ser.*, 345: 237-244

Aguirre, C., Pizarro, Ó., Strub, P.T., Garreaud, R., Barth, J.A. (2012) Seasonal dynamics of the near-surface alongshore flow off central Chile. *J. Geophys. Res.*, 117, C01006, doi:10.1029/2011JC007379.

Arrizaga, A. (1981) Nuevos antecedentes biologicos para la sardina comun, *Clupea* (*Strangomera*) *bentincki*, Norman 1936. *Bol. Soc. Biol. Concepcion*, 52: 5–66.

Atlas, R., Hoffman, R.N., Ardizzone, J., Leidner, S.M., Jusem, J.C., Smith, D.K., Gombos D. (2011), A cross-calibrated, multiplatform ocean surface wind velocity product for meteorological and oceanographic applications. *Bull. Amer. Meteor. Soc*., 92: 157-174. doi: 10.1175/2010BAMS2946.1

Baird, M.E., Leth, O., Middleton, J.F. (2007) Biological response to circulation driven by mean summertime winds off central Chile: A numerical model study. *J. Geophys. Res*., 112, C07031, doi:10.1029/2006JC003655

Bakun, A. (1996) Patterns in the ocean. Ocean processes and marine population dynamics: University of California Sea Grant, California, USA, in cooperation with Centro de Investigaciones Biologicas de Noroeste, La Paz, Baja California Sur, Mexico.

Bane, J.M., Spitz, Y.H., Letelier, R.M., Peterson, W.T. (2007) Jet stream intraseasonal oscillations drive dominant ecosystem variations in Oregon's summertime coastal upwelling system. *PNAS*, 104(33): 13262-13267.

Batchelder, H.P., Daly, K.L., Davis C.S, Ji, R., Ohman M.D., Peterson, W.T., Runge J.A. (2013) Climate Impacts on zooplankton Population Dynamics in Coastal Marine Ecosystems. *Oceanography*, 26: 34:51.

Batchelder, H.P. (2006) Forward-in-Time/Backward-in-Time Trajectory (FITT/BITT) Modeling of Particles and Organisms in the Coastal Ocean. *Journal of Atmospheric and Oceanic Technology* 23: 727-741

Batchelder, H.P., Edwards, C.A., Powell, T.M. (2002) Individual-based models of copepod populations in coastal upwelling regions: implications of physiologically and environmentally influenced diel vertical migration on demographic success and nearshore retention. *Prog. Oceangr.*, 53: 307-333.

Belmadani, A., Echevin, V., Dewitte, B., Colas F. (2012) Equatorially-forced intraseasonal propagations along the Peru-Chile coast and their relation with the nearshore eddy activity in 1992-2000: A modelling study. *J. Geophys. Res.*, doi:10.1029/2011JC007848.

Bertrand, A., Segura, M., Gutierrez, M., Vasquez, L. (2004) From small-scale habitat loopholes to decadal cycles: a habitat-based hypothesis explaining fluctuation in pelagic fish populations off Peru. *Fish and Fisheries,* 5: 296–316.

Boyra, G., Rueda, L., Coombs, S.H., Sundby, S., Ådlandsvik, B., Santos, M., Uriarte, A. (2003) Modelling the vertical distribution of eggs of anchovy (*Engraulis encrasicolus*) and sardine (*Sardina pilchardus*). *Fish. Oceanogr*., 12: 381–395.

Brink, K.H., Robinson A.R. (1998) *The Global Coastal Ocean: Processes and Methods*, Volume 10, *The Sea*, John Wiley & Sons, Inc., New York, 604 + xiii pp.

Brochier, T., Lett, C., Fréon, P. (2011) Investigating the 'northern Humboldt paradox' from model comparisons of small pelagic fish reproductive strategies in eastern boundary upwelling ecosystems. *Fish and Fisheries*, 12: 94–109. doi: 10.1111/j.1467-2979.2010.00385.x

Brochier, T., Lett, C., Tam, J., Fréon, P., Colas, F., Ayón, P. (2008) An individual-based model study of anchovy early life history in the northern Humboldt Current system. *Prog. Oceangr.,* 79: 313–325.

Buckley, L.J., Durbin E.G. (2006) Seasonal and inter-annual trends in the zooplankton prey and growth rate of Atlantic cod (*Gadus morhua*) and haddock (*Melanogrammus aeglefinus*) larvae on Georges Bank. *Deep-Sea Res*. *II*, 53: 2758-2770.

Cambon, G., Goubanova, K., Marchesiello, P., Dewitte, B., Illig, S., Echevin, V. (2013) Assessing the impact of downscaled winds on a regional ocean model simulation of the Humboldt system. *Ocean Modelling*, 65: 11-24

Cargnelli L.M., Gross M.R. (1996) The temporal dimension in fish recruitment: birth date, body size, and size dependent survival in a sunfish (bluegill: *Lepomis macrochirus*). *Can. J. Fish. Aquat. Sci*., 53: 360−367

Carr, S.D., Capet, X.J., McWilliams, J.C., Pennington, J.T., Chavez, F.P. (2008) The influence of diel vertical migration on zooplankton transport and recruitment in an upwelling region: estimates from a coupled behavioral-physical model. *Fish. Oceanogr.*, 17: 1–15. doi: 10.1111/j.1365-2419.2007.00447.x

Carton, J., Giese, B. (2008) A reanalysis of ocean climate using Simple Ocean Data Assimilation (SODA). *Mon. Wea. Rev*., 136 (8): 2999–3017.

Castillo-Jordan, C., Cubillos, L.A., Paramo, J. (2007) The spawning spatial structure of two co-occurring small pelagic fish off central southern Chile in 2005. *Aquat. Living Resour.*, 20: 77-84.

Castillo, J., Saavedra, A., Galvez, P. (2005) Evaluacion acustica de la biomasa, abundancia, distribucion espacial y caracterizacion de cardumenes de anchoveta y sardina comun durante el periodo de reclutamiento, Zona Centro-Sur, Verano 2005. FIP Rep. No 2004-05: 205 pp.

Castro, L.R., Clarmunt, G., Krautz, M.C., Llanos-Rivera, A., Moreno, P. (2009) Egg trait variation in anchoveta *Engraulis ringens*: a maternal response to changing environmental conditions in contrasting spawning habitat. *Mar. Ecol. Prog. Ser.*, 381: 237-248.

Castro, L.R., Salinas G.R., Hernández, E.H. (2000) Environmental influences on winter spawning of the anchoveta *Engraulis ringens* off Central Chile. *Mar. Ecol. Prog. Ser.,* 197: 247–258

Castro, L.R., Hernández, E.H. (2000) Early Life Survival of the Anchoveta *Engraulis ringens* Off Central Chile during the 1995 and 1996 Winter Spawning Seasons. *Trans. Am. Fish. Soc.*, 129: 1107-1117.

Catalan, I.A., Macias, D., Sole, J., Ospina-Alvarez, A., Ruiz, J. (2013) Stay off the motorway: Resolving the pre-recruitment through a spatially explicit individual based model (SEIBM). *Prog. Oceanogr.*, 111: 140-153.

Chapman, D.C. (1985), Numerical treatment of cross-shelf open boundaries in a barotropic coastal ocean model. *J. Phys. Oceanogr.*, 15: 1060-1075.

Chavez, F.P., Ryan, J., Lluch-Cota, E., Niquen, M. (2003) From Anchovies to Sardines and Back: Multidecadal Change in the Pacific Ocean. *Science*, 299: 217-221

Checkley, D.M., Ayón, P., Baumgartner, T.R., Bernal, M., Coetzee, J.C., Emmett, R., Guevara-Carrasco, R., Hutchings, L., Ibaibarriaga, L., Nakata, H., Oozeki, Y., Planque, B., Schweigert, J., Stratoudakis, Y., van der Lingen, C.D. (2009) Habitats. In: Checkley, D., Alheit, J., Oozeki, Y., Roy, D. (Eds.), Climate Change and Small Pelagic Fish. Cambridge University Press, pp. 12–14.

Chenillat, F., Riviere, P., Capet, X., Franks, P.J.S., Blanke, B. (2013) California Coastal Upwelling Onset Variability: Cross-Shore and Bottom-Up Propagation in the Planktonic Ecosystem. *Plos One,* 8(5): e62281. doi:10.1371/journal.pone.0062281

Claramunt, G., Cubillos, L.A., Castro, L., Hernández, C., Arteaga, M. (2013) Variation in the spawning periods of *Engraulis ringens* and *Strangomera bentincki* off the coasts of Chile: a quantitative analysis. *Fish. Res.*, 160: 96-102

Claramunt, G., Castro, L.R., Cubillos, L.A., Hirche, H.J., Perez, G., Braun M. (2012) Inter-annual reproductive trait variation and spawning habitat preferences of *Engraulis ringens* off northern Chile. *Revista de Biologia Marina y Oceanografia*, (47): 227-243.

Coombs, S.H., Boyra, G., Rueda, L.D. *et al*. (2004) Buoyancy measurements and vertical distribution of eggs of sardine (*Sardina pilchardus*) and anchovy (*Engraulis encrasicolus*). *Marine Biology*, 145 (5): 959–970.

Correa-Ramirez, M.A., Hormazabal, S., Morales, C.E. (2012) Spatial patterns of annual and interannual surface chlorophyll-a variability in the Peru–Chile Current System. *Prog. Oceanogr.* doi:10.1016/j.pocean.2011.07.008

Cubillos, L.A., Claramunt, G., Castro, L.R. (2013) Simulation of fishery-induced changes on the reproductive cycle of common sardine, *Strangomera bentincki*, off central southern Chile. *Fish. Res.*, 160: 103-111

Cubillos, L.A. *et al*. (2009) Reproductive dynamic of anchoveta and common sardine, southern-central Chile, year 2006 (*in Spanish*). *Technical Report, FIP-2006-13*, University of Concepcion, 141 pp.

Cubillos, L.A., Claramunt, G. (2009) Length-structured analysis of the reproductive season of anchovy and common sardine off central southern Chile. *Mar. Biol*. (2009) 156:1673–1680, doi: 10.1007/s00227-009-1202-5

Cubillos, L.A., Ruiz, P., Claramunt, G., Gacitua, S., Nunez, S., Castro, L.R., Riquelme, K., Alarcon, C., Oyarzun, C., Sepulveda, A. (2007) Spawning, daily egg production, and spawning stock biomass estimation for common sardine (*Strangomera bentincki*) and anchovy (*Engraulis ringens*) off central southern Chile in 2002. *Fish. Res.*, 86: 228-240.

Cubillos, L.A., Arcos, D.F. (2002) Recruitment of common sardine (*Strangomera bentincki*) and anchovy (*Engraulis ringens*) of central-south Chile in the 1990s and the impact of the 1997–1998 El Niño. *Aquat. Living Resour.,* 15: 87–94.

Cubillos, L.A., Bucarey, D.A., Canales, M. (2002) Monthly abundance estimation for common sardine *Strangomera bentincki* and anchovy *Engraulis ringens* in the central-southern area off Chile (30–40_S). *Fish. Res*., 57:117–130.

Cubillos, L.A., Arcos, D.F., Bucarey, D.A., Canales, M.T. (2001) Seasonal growth of small pelagic fish off Talcahuano, Chile (37°S, 73°W): a consequence of their reproductive strategy to seasonal upwelling? *Aquat. Living Resour*., 14: 115–124.

Curchitser, E.N., Batchelder H.P., Haidvogel D.B., Fitcher J., Runge J. (2013) Advances in Physical, Biological, and Coupled Ocean Model During the US GLOBEC Program. *Oceanography*, 26(4): 52-67.

Cury, P., Bakun, A., Crawford, R.J.M., Jarre-Teichmann, A., Quinones, R.A., Shannon, L.J., Verhey H.M. (2000) Small pelagics in upwelling systems: patterns of interaction and structural changes in "wasp-waist" ecosystems. *ICES J. Mar. Sci*., 211: 603–618.

Cury, P., Roy, C. (1989) Optimal environmental window and pelagic fish reproductive success in upwelling areas. *Can. J. Fish. Aquat. Sci*., 46: 670-680.

Cushing, D.H. (1990) Plankton production and year-class strength in fish populations; an update of the match/mismatch hypothesis. *Adv. Mar. Biol.*, 26: 249–293.

Cushing, D.H. (1975) Marine ecology and fisheries. Cambrigde University Press, London. 278 pp.

Dee, D.P. *et al*. (2011) The ERA-Interim reanalysis: configuration and performance of the data assimilation system. *Q.J.R. Meteorol. Soc.*, 137: 553–597. doi: 10.1002/qj.828

Dewitte, B., S. Illig, L. Renault, K. Goubanova, K. Takahashi, D. Gushchina, K. Mosquera, S. Purca (2011) Modes of covariability between sea surface temperature and wind stress intraseasonal anomalies along the coast of Peru from satellite observations (2000–2008). *J. Geophys. Res. Oceans (1978–2012)*, 116, C4

Drake, P.T., Edwards, C.A., Morgan, S.G., Dever, E.P. (2013) Influence of larval behavior on transport and population connectivity in a realistic simulation of the California Current System. *Journal of Marine Research*, 71(4): 317-350, doi: 10.1357/002224013808877099

Duchon, C. (1979) Lanczos filtering in one and two dimensions. *J. Appl. Meteorol.*, 18: 1016-1022

Echevin, V., Aurelie, A., Marina, L., Michelle, G., Olivier, A., Alice, P., Gilles, G. (2014) Intraseasonal variability of nearshore productivity in the Northern Humboldt Current System: the role of coastal trapped waves. *Cont. Shelf Res.,* 73: 14-30.

Echevin, V., Aumont, O., Ledesma, J., Flores, G. (2008) The seasonal cycle of surface chlorophyll in the Peruvian upwelling system: A modelling study. *Prog. Oceangr.*, 79: 167–176

Escribano, R., Daneri, G., Farías, L., Gallardo, V., González H., *et al*. (2004) Biological and chemical consequences of the 1997–1998 El Niño in the Chilean coastal upwelling system: a synthesis. *Deep Sea Res. II*, 51.20: 2389-2411.

FAO (2012) Statistical Yearbook: World Food And Agriculture, 362 pp. Food and Agriculture Organization of the United Nations, Italy.

Fiechter, J., Rose, K.A., Curchitser, E.N., Hedstrom, K.S. (2015) The role of environmental controls in determining sardine and anchovy population cycles in the California Current: Analysis of an end-to-end model. *Prog. Oceangr.* http://dx.doi.org/10.1016/j.pocean.2014.11.013

Fiksen, Ø., Jørgensen, C., Kristiansen, T. *et al*. (2007) Linking behavioural ecology and oceanography: larval behaviour determines growth, mortality and dispersal. *Mar. Ecol. Prog. Ser.*, 347: 195–205.

Fischer, G., Karakas, G. (2009) Sinking rates and ballast composition of particles in the Atlantic Ocean: implications for the organic carbon fluxes to the deep ocean. *Biogeosciences*, 6: 85-105

Flather, R.A. (1976) A tidal model of the northwest European continental shelf. *Memoires de la Societe Royale de Sciences de Liege*, 6: 141-164.

Galperin, B., Kantha, L.H., Hassid, S., Rosati, A. (1988) A quasi-equilibrium turbulent energy model for geophysical flows. *J. Atmos. Sci.*, 45: 55-62.

Garreaud, R., Falvey, M. (2009) The coastal winds off western subtropical South America in future climate scenarios. *Int. J. Climatol*., 29: 543–554, doi:10.1002/joc.1716.

Garreaud, R., Munoz, R. (2005) The low-level jet off the subtropical west coast of South America: structure and variability. *Mon. Wea. Rev*., 133: 2246–2261

Geider, R.J., McIntyre, H.L., Kana, T.M. (1997) Dynamic model of phytoplankton grwoth acclimation: Response of the balanced growth rate and the chlorophyll-a: Carbon ratio to light, nutrient limitation and temperature. *Mar. Ecol. Prog. Ser.*, 148: 187-200

Gerlotto, F., Castillo, J., Saavedra, A., Barbieri, M.A., Espejo, M., and Cotel, P. (2004) Three-dimensional structure and avoidance behaviour of anchovy and common sardine schools in central southern Chile. *ICES J. Mar. Sci.*, 61: 1120-1126.

Ghil, M., Mo, K. (1991) Intraseasonal oscillations in the global atmosphere, part 1, Southern hemisphere. *J. Atmos. Sci.*, 48: 780–790

Gomez, F., Montecinos, A., Hormazabal, S., Cubillos, L.A., Correa-Ramirez, M.A., Chavez F.P. (2012) Impact of spring upwelling variability off southern-central Chile on common sardine (*Strangomera bentincki*) recruitment. *Fish. Oceanogr*., 21: 405–414. doi: 10.1111/j.1365-2419.2012.00632.x

González, C.E., Escribano, R., Hidalgo, P. (2015) Intra-seasonal variation and its effects on copepod community structure off Central/southern Chile (2002-2009), *Hydrobiologia*: 758: 61-74.

Goubanova, K., Illig, S., Machu, E., Garçon, V., Dewitte B. (2013) SST subseasonal variability in the central Benguela upwelling system as inferred from satellite observations (1999–2009). *J. Geophys. Res. Oceans*, 118: 4092–4110, doi:10.1002/jgrc.20287.

Grimm, V., Railsback, S.F. (2005) Individual-Based Modeling and Ecology. Princeton University Press, New Jersey.

Hanson, P.C., Johnson, T.B., Schindler, D.E., Kitchell, J.F. (1997) Fish bioenergetics 3.0 for Windows. Technical Report WISCU-T-97-001. University of Wisconsin Sea Grant Institute, Madison, WI, USA.

Hernandez, E.H., Castro, L.R. (2000) Larval growth of the anchoveta, *Engraulis ringens*, during the winter spawning season off central Chile. *Fishery Bulletin,* 98(4): 704-710

Hjort, J. (1914) Fluctuations in the great fisheries of the northern Europe viewed on the light of biological research. Rapp.P.-v Reun. Cons. int. Explor. Mer., 178.

Hormazabal, S., Shaffer, G., Pizarro, O. (2002) Tropical Pacific control of intraseasonal oscillations off Chile by way of oceanic and atmospheric pathways. *Geophys. Res. Lett*., 29(6), doi:10.1029/2001GL013481

Hormazabal, S., Shaffer, G., Letelier, J., Ulloa, O. (2001) Local and remote forcing of sea surface temperature in the coastal upwelling system off Chile. *J. Geophys. Res.*, 106: 16,657–16,671

Houde, E.D. (1989) Comparative Growth, Mortality, and Energetic of Marine Fish Larvae: Temperature and Implied Latitudinal Effects. *Fishery Bulletin*, 87: 471:495.

Houde, E.D. (1987) Fish early life dynamics and recruitment variability. *Am. Fish. Soc. Symp*., 2: 17-29

Husebø, A., Stenevik, E.K., Slotte, A., Fossum, P., Salthaug, A., Vikebø, F., Aanes, S., et al. 2009. Effects of hatching time on year-class strength in Norwegian spring-spawning herring (*Clupea harengus*). *ICES J. Mar. Sci.*, 66: 1710–1717.

Illig, S., Dewitte, B., Goubanova, K., Cambon, G., Boucharel, J., Monetti, F., Romero, C., Purca, S., Flores R. (2014), Forcing mechanisms of intraseasonal SST variability off central Peru in 2000–2008. *J. Geophys. Res. Oceans*, 119: 3548–3573, doi:10.1002/2013JC009779.

Kalnay, E., Kanamitsu, M., Kistler, R., Collins, W., Deaven, D., *et al*. (1996) The NCEP/NCAR 40-Year Reanalysis Project. *Bull. Amer. Meteor. Soc.*, 77: 437–471.

Kishi, M., Kashiwai, M., Ware, D., Megrey, B., Eslinger, D., *et al*. (2007) NEMURO - a lower trophic level model for the North Pacific marine ecosystem. *Ecol. Modell*., 202 (1–2): 12–25

Kitchell, J.F., Stewart, D.J., Weininger, D. (1977) Applications of a bioenergetics model to yellow perch (*Perca flavescens*) and walleye (*Stizostedion vitreum*). *J. Fish. Res. Bd. Can*. 34: 1922–1935.

Landaeta, M.F., Castro, L.R. (2012) Vertical distribution and gas bladder inflation/deflation in postlarval anchoveta *Engraulis ringens* during upwelling events. *Journal of the Marine Biological Association of the United Kingdom*, 93: 321-331.

Lasker, R. (1975) Field criteria for survival of anchovy larvae: relation between inshore chlorophyll maximun layers and successful first feeding. *Fishery Bulletin US*, 73: 453-462.

Le Pape, O., Bonhommeau, S. (2015) The food limitation hypothesis for juvenile marine fish. *Fish and Fisheries*, 16: 373–398. doi: 10.1111/faf.12063

Leggett, W.C., Deblois, E. (1994) Recruitment in marine fishes: is it regulated by starvation and predation in the egg and larval stages? *Netherlands Journal of Sea Research*, 32 (2): 119–134.

Leth, O., Middleton, J.F. (2006) A numerical study of the upwelling circulation off central Chile: Effects of remote oceanic forcing. *J. Geophys. Res.*, 111, C12003, doi:10.1029/2005JC003070.

Lett, C., Penven P., Ayón, P., Fréon, P. (2007) Enrichment, concentration and retention processes in relation to anchovy (*Engraulis ringens*) eggs and larvae distributions in the northern Humboldt upwelling ecosystem, *Journal of Marine Systems*, Volume 64, Issues 1–4: 189-200

Li Q.P., Franks, P.J.S., Landry, M.R., Goericke, R., Taylor A.G. (2010) Modeling phytoplankton growth rates and chlorophyll to carbon ratios in California coastal and pelagic ecosystems. *J. Geophys. Res.* (115) (G4): 1–12.

Liu, Y., Liang, X.S., Weisberg, R.H. (2007) Rectification of the bias in the wavelet power spectrum. *Journal of Atmospheric and Oceanic Technology,* 24(12): 2093-2102

Llanos-Rivera, A., Castro, L.R. (2006) Inter-population differences in temperature effects on *Engraulis ringens* yolk-sac larvae. *Mar. Ecol. Prog. Ser.,* 312: 245–253.

Llanos-Rivera, A., Herrera, G., Bernal, P. (2004) Food size selectivty and diet overlap in larvae of Clupeiform species from central Chile. *Cah. Biol. Mar*., 45: 1-8.

Madden, R.A., Julian, P.R. (1972) Description of global-scale circulation cells in the Tropics with a 40–50 day period. *J. Atmos. Sci*, 29: 1109–1123.

Marchesiello, P., McWilliams, J., Shchepetkin A. (2001) Open boundary conditions for long-term integration of regional oceanic models. *Ocean Modell*., 3: 1–20, doi:10.1016/S1463-5003(00)00013-5.

Masumoto, Y., Sasaki, H., Kagimoto, T., Komori, N., Ishida, A., *et al*. (2004) A fifty year eddy-resolving simulation of the world ocean: Preliminary outcomes of OFES (OGCM for the Earth Simulator). *Journal of Earth Simulator* 1 (April): 35–56.

Megrey, B.A., Rose, K.A., Klumb, R.A., Hay, D.E., Werner, F.E., Eslinger, D.L., Smith, S.L. (2007) A bioenergetics-based population dynamics model of Pacific herring (*Clupea harengus pallasi*) coupled to a lower trophic level nutrient-phytoplankton-zooplankton model: description, calibration, and sensitivity analysis. *Ecol. Modell.*, 202: 144–164.

Miller, T.J. (2007) Contribution of individual-based coupled physical–biological models to understanding recruitment in marine fish populations. *Mar. Ecol. Prog. Ser.,* 347: 127–138.

Miller, T.J., Crowder, L.B., Rice, J.A., Marshall, E.A. (1988) Larval size and recruitment mechanisms in fishes: toward a conceptual framework. *Can. J. Fish. Aquat. Sci.* 45: 1657–1667.

Montecinos, A., Gomez, F. (2010) ENSO modulation of upwelling season off southern-central Chile. *Geophys. Res. Lett*., 37:L02708

Montecinos, A., Aceituno, P. (2003) Seasonality of the ENSO related rainfall variability in central Chile and associated circulation anomalies. *J. Clim*., 16: 281– 296

Morales, C.E., Hormazabal, S., Andrade, I., Correa-Ramirez, M.A. (2013) Time-Space Variability of Chlorophyll-a and Associated Physical Variables within the Region off Central-Southern Chile. *Remote Sens., 5*: 5550-5571.

Mullon, C., Freon, P., Parada, C., van der lingen, C., Huggett, J. (2003) From particles to individuals: modelling the early stages of anchovy (*Engraulis capensis/encrasicolus*) in the southern Benguela. *Fish. Oceanogr.,* 12 (4/5): 396–406.

Ney, J.J. (1993) Bioenergetics modeling today: growing pains on the cutting edge. *Trans. Am. Fish. Soc.*, 122: 736–748.

Olivar, M., Salat, J., Palomera, I. (2001) Comparative study of spatial distribution patterns of the early stages of anchovy and pilchard in the NW Mediterranean Sea. *Mar. Ecol. Prog. Ser.*, 217: 111–120.

Ospina-Alvarez, A., Palomera, I., Parada, C. (2012a) Changes in egg buoyancy during development and its effects on the vertical distribution of anchovy eggs. *Fish. Res*., 117-118: 86-95

Ospina-Alvarez, A., Parada, C., Palomera, I. (2012b) Vertical migration effects on the dispersion and recruitment of European anchovy larvae: From spawning to nursery areas. *Ecol. Modell.*, 231: 65-79

Parada, C., Colas, F., Soto-Mendoza, S., Castro, L. (2012) Effects of seasonal variability in across-and alongshore transport of anchoveta (*Engraulis ringens*) larvae on model-based pre-recruitment indices off central Chile. *Prog. Oceangr.,* 92 (2012): 192-205.

Parada, C., Mullon, C., Roy, C., Freon, P., Hutchings, L., van der Lingen, L. (2008) Does vertical migratory behavior retain fish larvae onshore in upwelling ecosystems? A modeling study of anchovy in the southern Benguela. *African Journal of Marine Science*, 30: 437-452

Parada, C., Van Der Lingen, C.D., Mullon, C., Penven, P. (2003) Modelling the effect of buoyancy on the transport of anchovy (*Engraulis capensis*) eggs from spawning to nursery grounds in the southern Benguela: an IBM approach. *Fish. Oceanogr*., 12: 170–184.

Parrish, R.H., Bakun, A., Husby, D.M., Nelson, C.S. (1983) Comparative climatology of selected environmental processes in relation to eastern boundary current pelagic fish reproduction. *FAO Fishery Report,* 291(3): 731-777.

Pauly, D. (1987) Managing the Peruvian ecosystem: a synthesis. In: Pauly, D., Tsukayama, I. (Eds.), The Peruvian Anchovy and its Upwelling Ecosystem: Three Decades of Change. ICLARM Studies and Reviews 15, Instituto del Mar del Perú

(IMARPE), Callao, Peru; Deutsche Gesellschaft für Technische Zusammenarbeit (GTZ), GmbH, Eschborn, Federal Republic of Germany; and International Cen-ter for Living Aquatic Resources Management (ICLARM), Manila, Philippines, pp. 325–342.

Pauly, D., Tsukayama, I. (1987) The Peruvian Anchovy and its Upwelling Ecosystem: Three Decades of Change. ICLARM Studies and Reviews 15, Instituto del Mar del Perú (IMARPE), Callao, Peru; Deutsche Gesellschaft für Technische Zusammenarbeit (GTZ), GmbH, Eschborn, Federal Republic of Germany; and International Center for Living Aquatic Resources Management (ICLARM), Manila, Philippines.

Peck M.A., Hufnagl, M. (2012) Can IBMs tell us why most larvae die in the sea? Model sensitivities and scenarios reveal research needs. *Journal of Marine Systems,* 93: 77–93.

Pedraza-Garcia, M. and Cubillos, L.A. (2007) Population dynamic of two pelagic fish in the central-south area off Chile: delayed density-dependence and biological interaction. *Environ. Biol. Fishes,* 82: 111–122.

Platt, T., Gallegos, C.L., Harrison, W.G. (1980), Photoinhibition of photosynthesis in natural assemblages of marine phytoplankton. *J. Mar. Re*s., 38: 687-701.

Politikos, D., Somarakis, S., Tsiaras, K.P., Giannoulaki, M., Petihakis, G., Machias, A., Triantafyllou, G. (2015) Simulating anchovy's full life cycle in the northern Aegean Sea (eastern Mediterranean): a coupled hydro-biogeochemical-IBM model. *Prog*. *Oceangr*. http://dx.doi.org/10.1016/j.pocean.2014.09.002.

Politikos D., Triantafyllou, G., Petihakis G., Tsiaras K.P., Somarakis S., Ito S.I., Megrey B. (2011) Application of a bioenergetic growth model for European anchovy (*Engraulis encrasicolus*) linked with a lower trophic level ecosystem model. *Hydrobiology*, 670: 141-163.

Pyper, B.J., Peterman, R.M. (1998) Comparison of methods to account for autocorrelation in correlation analyses of fish data*. Can. J. Fish. Aquat. Sci*., 55: 2127–2140.

Rahn, D.A., Rosenbluth, B., Rutllant, J.A. (2015) Detecting Subtle Seasonal Transitions of Upwelling in North-Central Chile. *J. Phys. Oceanogr.*, 45: 854-867

Rahn, D.A. (2012), Influence of large scale oscillations on upwelling-favorable coastal wind off central Chile. *J. Geophys. Res.*, doi:10.1029/2012JD018016

Renault, L., Dewitte, B., Marchesiello, P., Illig, S., Echevin, V., Cambon, G., Ramos, M., Astudillo, O., Minnis, P., Ayers, J. K. (2012) Upwelling response to atmospheric coastal jets off central Chile: A modeling study of the October 2000 event, *J. Geophys. Res*., 117, C02030, doi:10.1029/2011JC007446

Renault, L., Dewitte, B., Falvey, M., Garreaud, R., Echevin, V., Bonjean F. (2009) Impact of atmospheric coastal jet off central Chile on sea surface temperature from satellite observations (2000–2007). *J. Geophys. Res*., 114, C08006, doi:10.1029/2008JC005083.

Rice, J. (1995) Food web theory, marine food webs, and what climate changes may do to northern marine fish populations. In: Climate Change and Northern Fish Populations (ed R. J. Beamish). *Canadian Special Publication of Fisheries and Aquatic Sciences*, 121: 561–568.

Rose, K.A. *et al*. (2015) Demonstration of a fully-coupled end-to-end model for small pelagic fish using sardine and anchovy in the California Current. *Prog*. *Oceangr*, http://dx.doi.org/10.1016/j.pocean.2015.01.012.

Rose, K.A. (2012) End-to-end models for marine ecosystems: are we on the precipice of a significant advance or just putting lipstick on a pig? *Scientia Marina*, 76: 195–201.

Rose, K.A *et al*. (2010) End-to-end models for the analysis of marine ecosystems: challenges, issues, and next steps. *Marine and Coastal Fisheries* 2: 115–130.

Rose, K.A., Megrey, B., Werner, F., Ware, D. (2007) Calibration of the NEMURO nutrient–phytoplankton–zooplankton food web model to a coastal ecosystem: Evaluation of an automated calibration approach. *Ecol. Modell.* (202)(1–2): 38–51.

Rose, K.A., Cowan, J.H., Clark, M.E., Houde, E.D., Wang, S.B. (1999) An individual based model of bay anchovy population dynamics in the mesohaline region of Chesapeake Bay. *Mar Ecol. Prog. Ser.*, 185: 113–132.

Rutllant, J.A., Rosenbluth, B., Hormazabal, S. (2004) Intraseasonal variability of wind-forced coastal upwelling off central Chile (30_S). *Cont. Shelf Res*., 24: 789–804, doi:10.1016/j.csr.2004.02.004.

Rutllant, J.A., Fuenzalida, H. (1991) Synoptic aspects of the central Chile rainfall variability associated with the Southern Oscillation. *Int. J. Climatol*., 11: 63–76.

Saldías, G., Sobarzo, M., Largier, J., Moffat, C., Letelier, R. (2012) Seasonal variability of turbid river plumes off central Chile based on high-resolution MODIS imagery. *Remote Sens. Environ.*, 123: 220-233.

Scheffer, M., Baveco, J.M., DeAngelis, D.L., Rose, K.A., van Nes, E.H. (1995) Superindividuals a simple solution for modeling large populations on an individual basis. *Ecol. Modell*., 80: 161–170.

Schwartzlose, R.A. *et al*. (1999) Worldwide large-scale fluctuations of sardine and anchovy populations. *South African Journal of Marine Sciences,* 21: 289–347.

Serra, J.R. (1983) Changes in the abundance of pelagic resources along the Chilean coast. *FAO Fish. Rep*. 291: 255-281.

Shaffer, G., Hormazabal, S., Pizarro, O., Salinas, S. (1999) Seasonal and interannual variability of currents and temperature over the slope off central Chile, *J. Geophys. Res.*, 104: 29,951–29,961

Shannon, L.J., Field J.G., Moloney C.L. (2004) Simulating anchovy–sardine regime shifts in the southern Benguela ecosystem. *Ecol. Modell*., 172: 269–281

Shchepetkin, A., McWilliams, J. (2005) The regional oceanic modeling system (ROMS): A split-explicit, free-surface, topography-following coordinate oceanic model, *Ocean Modell*., 9: 347–404, doi:10.1016/j. ocemod.2004.08.002.

Sinclair, M., Iles, T. D. (1989) Population regulation and speciation in the oceans. *J. Cons. Int. Explorer. Mer*., 45: 165-175.

Smith, W., Sandwell, D. (1997) Global seafloor topography from satellite altimetry and ship depth soundings. *Science*, 277: 1956–1962, doi:10.1126/science.277.5334.1956.

Soto-Mendoza, S., Castro, L.R., Llanos-Rivera, A. (2010) Variabilidad espacial y temporal de huevos y larvas de *Strangomera bentincki* y *Engraulis ringens*, asociados a la desembocadura del río Itata, Chile. *Revista de Biología Marina y Oceanografía*, 45(3): 471-487.

Spitz, Y.H., Newberger, P.A., Allen, J.S. (2003), Ecosystem response to upwelling off the Oregon coast: Behavior of three nitrogen-based models. *J. Geophys. Res.,* 108: doi: 10.1029/2001JC001181

Strub, P.T., Mesías, J.M., Montecino, V., Rutllant, J., Salinas, S. (1998) Coastal ocean circulation off western South America. In: Robinson, A.R., Brink, K.H. (Eds.), The Sea. John Wiley and Sons, New York, pp. 273–314.

Thornton, K.W., Lessem, A.S. (1978) A temperature algorithm for modifying biological rates. *Trans. Am. Fish. Soc*., 107: 284–287.

Torrence, C., Compo G.P. (1998) A practical guide to wavelet analysis. *Bull. Am. Meteorol. Soc*., 79: 61–78.

Travers, M., Shin, Y.J., Jennings, S., Cury, P. (2007) Towards end-to-end models for investigating the effects of climate and fishing in marine ecosystems. *Prog. Oceanogr.,* 75: 751-770.

Urtizberea, A., Fiksen, Ø., Folkvord, A., Irigoien, X. (2008) Modelling growth of larval anchovies including diel feeding patterns, temperature and body size. *J. Plankton Res.,* 12: 1369–1383.

van der Lingen, C.D., Bertrand, A., Bode, A., Brodeur, R., Cubillos, L.A., Espinoza, P., Friedland, K., Garrido, S., Irogoien, X., Miller, T., Mollmann, C., Rodriquez-Sanchez, R., Tanaka, H., Temming, A. (2009) Trophic dynamics. In: Checkley, D.M., Jr., Alheit, J., Oozeki, Y., Roy, C. (Eds.), Climate Change and Small Pelagic Fish. Cambridge University Press, pp. 112–157.

Villavicencio, Z., Muck, P. (1983) Maintenance ration, maintenance density, and growth efficiency of *Engraulis ringens* and *Sardinops sagax*, as measurements of their ecological potential. *Bol. Inst. Mar*. *Peru-Callao*, 7(4): 69-108

Vikebø, F., Jørgensen, C., Kristiansen, T., Fiksen, Ø. (2007) Drift, growth, and survival of larval Northeast Arctic cod with simple rules of behaviour. *Mar. Ecol. Prog. Ser.,* 347: 207–219.

von Storch, H., Zwiers, F.W. (1999), Statistical Analysis in Climate Research, 484 pp., Cambridge Univ. Press, Cambridge, U. K.

Werner, E.E., Gilliam, J.F. (1984) The Ontogenetic Niche and Species Interactions in Size-Structured Populations. *Annual Review of Ecology and Systematics*, 15: 393-425

Wheeler, M.C., Hendon, H.H. (2004) An all-season real-time multivariate MJO Index: Development of an Index for Monitoring and Prediction. *Mon. Weather Rev*., 132: 1917–1932, doi:10.1175/1520-0493(2004) 132<1917:AARMMI>2.0.CO;2.

Xu, Y., Rose, K.A, Chai F., Chavez F.P., Ayon, P. (2015) Does spatial variation in environmental conditions affect recruitment? A study using a 3-D model of Peruvian anchovy. *Prog. Oceanogr*. http://dx.doi.org/10.1016/j.pocean.2015.04.002

Xu, Y., Chai, F., Rose, K.A., Ñiquen, C.M., Chavez, F.P. (2013) Environmental influences on the interannual variation and spatial distribution of Peruvian anchovy

(*Engraulis ringens*) population dynamics from 1991 to 2007: a three dimensional modeling study. *Ecol. Modell.*, 264: 64–82.

Yanez-Rubio, A., Llanos-Rivera, A., Castro, L.R., Claramunt, G., Herrera, L. (2011) Variation in type, width, volume and carbon content of anchoveta *Engraulis ringens* food items during the early larval stages. *Journal of the Marine Biological Association of the United Kingdom*, 91 (6): 1207-1213

Yoshie, N, Yamanaka, Y., Rose, K.A., Eslinger, D.L., Ware, D.M., Kishi, M.J. (2007) Parameter sensitivity study of a lower trophic level marine ecosystem model ‘‘NEMURO’’. *Ecol. Model.,* 202: 26–37

Zheng, J. (1996) Herring stock-recruitment patterns in the North Atlantic and northeast Pacific Oceans. *Fish. Res*., 26: 257–277.

Appendix A

Model-Data Comparisons of Selected Physical and Biochemical Fields

Mean state of physical fields

The model's ability to reproduce SST and mixed layer depth (MLD) is evaluated. The mean annual model SST reproduces well the spatial pattern of the satellite SST. Temperature differences between model and satellite data are small, usually < 1°C (Fig. A1a-b). A narrow coastal fringe of negative values, mainly between 35-37°S, suggests a slight model underestimation near the coast, whereas temperature differences elsewhere are slightly positive (Fig. A1b). MLD was derived offline from the model temperature and salinity, estimated using the 0.2°C and 0.03 practical salinity units criteria used in the CARS 2009 (CSIRO Atlas of Regional Seas) climatology (Fig. A1c). The model MLD has a marked cross-shore gradient, with values ca. 10 m at the coast and >40 m at 76°W. The model and CARS have MLD that differ by -10 to 10 m (Fig. A1d), but most of the MLD differences over the continental shelf are <5 m. The most positive differences occur around 74°W, south of 36°S, whereas MLD differences are negative and small north of 34°S.

A vertical section of temperature at 35°S is used to compare the mean annual model temperature with the World Ocean Atlas (WOA, version 2013) (Fig. A1e). Overall, the model reasonably reproduces the mean features in WOA temperature, with the isotherms shoaling (deepening) shoreward in the upper layer (below 200 m). Model temperature is ca. 1.5°C cooler than WOA temperature in the coastal upper layer, probably due to upwelling being overly strong in the model. This could be a consequence of wind stress near shore being too high, since QuikSCAT does not resolve winds within 25 km or more from shore (Renault *et al*., 2012). In addition, the colder temperature near the coast could be the result of a shallower thermocline, which is evident as negative values between 100-400 m depth (Figure A1f). It is worth noting that the multidecade WOA climatology comparison with the model period (2003-2008) may be partially biased.

Annual mean meridional flows at 35°S in the model are shown in Figure A1g. The vertical section reveals (1) a surface-intensified equatorward coastal jet (>15 cm s^{-1}), (2) a poleward Peru-Chile undercurrent beneath that coastal jet with a core located at 200 m depth (~7 cm s^{-1}), and (3) an equatorward coastal transition zone jet ca. 75°W. These features are consistent with previously validated modeling studies (e.g. Aguirre *et al*., 2012; Cambon *et al*., 2013) and observations (Strub *et al*., 1998).

Sea level variability

The seasonal progression of sea level anomalies (SLA) derived from model outputs and AVISO (Archiving, Validation, and Interpretation of Satellite Oceanographic data) altimetry are compared in Figure A2a-h. The model reproduces the main spatial patterns observed in the seasonal time scale, although the amplitude of the model anomalies slightly exceeds that of AVISO, especially over the middle-inner shelf. In addition, the model sea level is significantly correlated to coastal sea level observations from Valparaiso (33°S; Fig. A2i) and Talcahuano (36.7°S; Fig. A2j). The amplitudes of the seasonal signals in the model and observed sea level are similar, but the intensity of the observed intraseasonal signal seems to be stronger than the model intraseasonal signal. The correlation of the low-passed (f_c = 1/15 day^{-1}) time series in Valparaiso and Talcahuano is 0.45 and 0.62, respectively. In the 30-80 day intraseasonal band the correlation is 0.45 and 0.44, respectively.

Biological model

Modeled phytoplankton (diatom + nanophytoplankton) at the surface is compared with satellite chlorophyll (Fig. A3a-f). Ideally, this comparison would be based on knowledge of the spatial and temporal conversion factors that related chlorophyll to phytoplankton nitrogen, which are known to be highly variable (Li *et al*, 2010). Lacking information on that relationship, we instead examine directly chlorophyll and phytoplankton mean fields,

by assuming that the CHL:N ratio is approximately 1.0. Overall, the main patterns in satellite chlorophyll are reproduced by the model phytoplankton, including the locations with maximum chlorophyll over the shelf. Phytoplankton and chlorophyll averaged over the annual cycle (Fig. A3a, d) show a marked cross-shore gradient, with shelf concentrations one order of magnitude larger than the concentrations over the coastal transition zone (200-300 km offshore). The model appears to underestimate the phytoplankton biomass in the southern coastal region, especially during fall-winter (Fig. A3c, f). However, the satellite sensor might overestimate phytoplankton biomass in that region due to higher dissolved organic matter concentrations linked to strong river run-off during fall-winter. Our model did not include coastal freshwater runoff, which is greatest in the southern region. Comparison of NO_3 with nitrate from the WOA in a vertical section at 35°S show large discrepancies in the nearshore surface waters and at 100-300 m across the section (Fig. A3g, h). The overestimation of model NO_3 at the surface reflects the too strong coastal upwelling and the too shallow surface mixed layer (Fig. A1f). Although the stronger upwelling of NO_3 rich water near the coast may lead to higher phytoplankton production, we consider that the model does a reasonable good job reproducing the main temporal and spatial patterns of phytoplankton production.

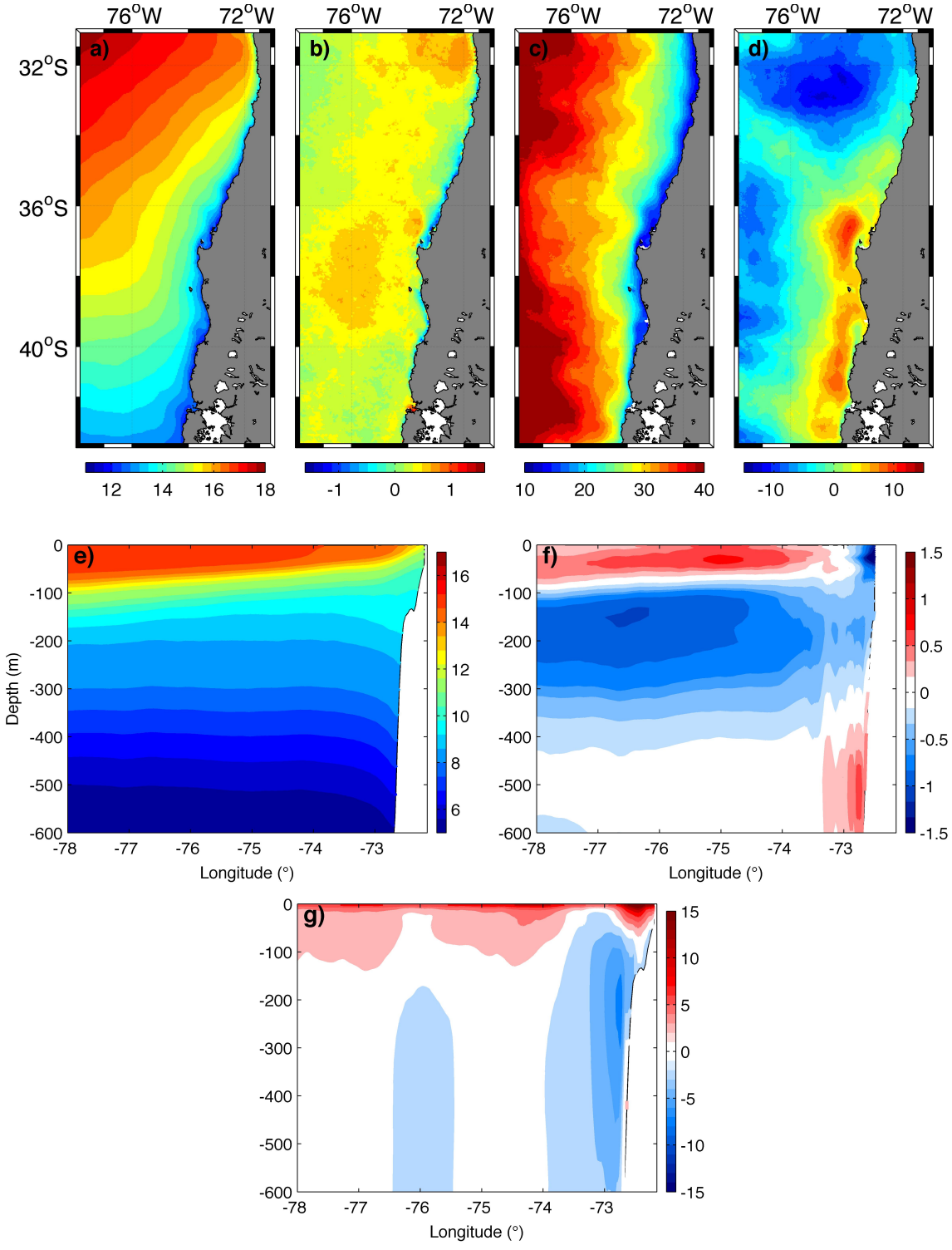

Figure A1 (legend on page 137)

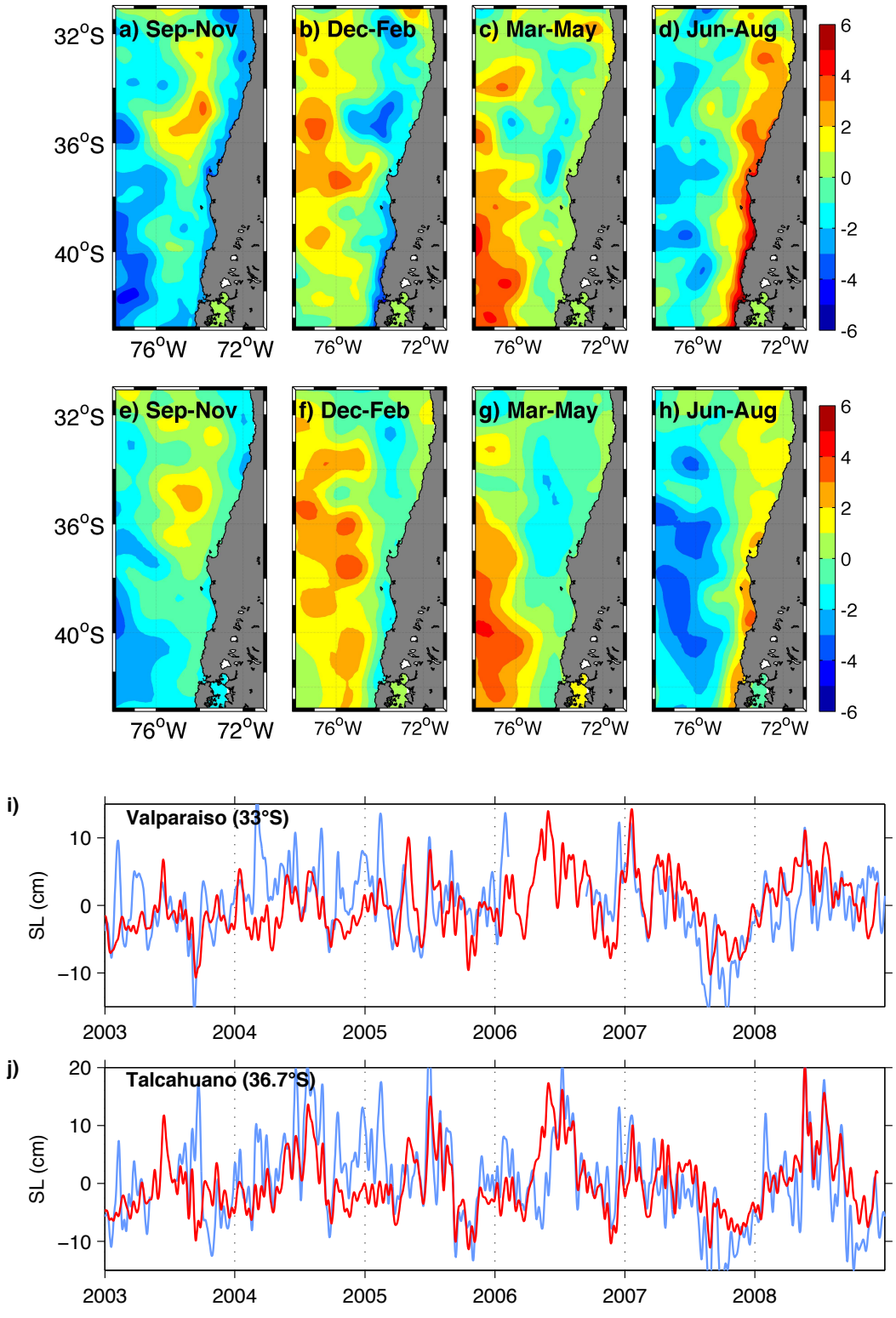

Figure A2 (legend on page 137)

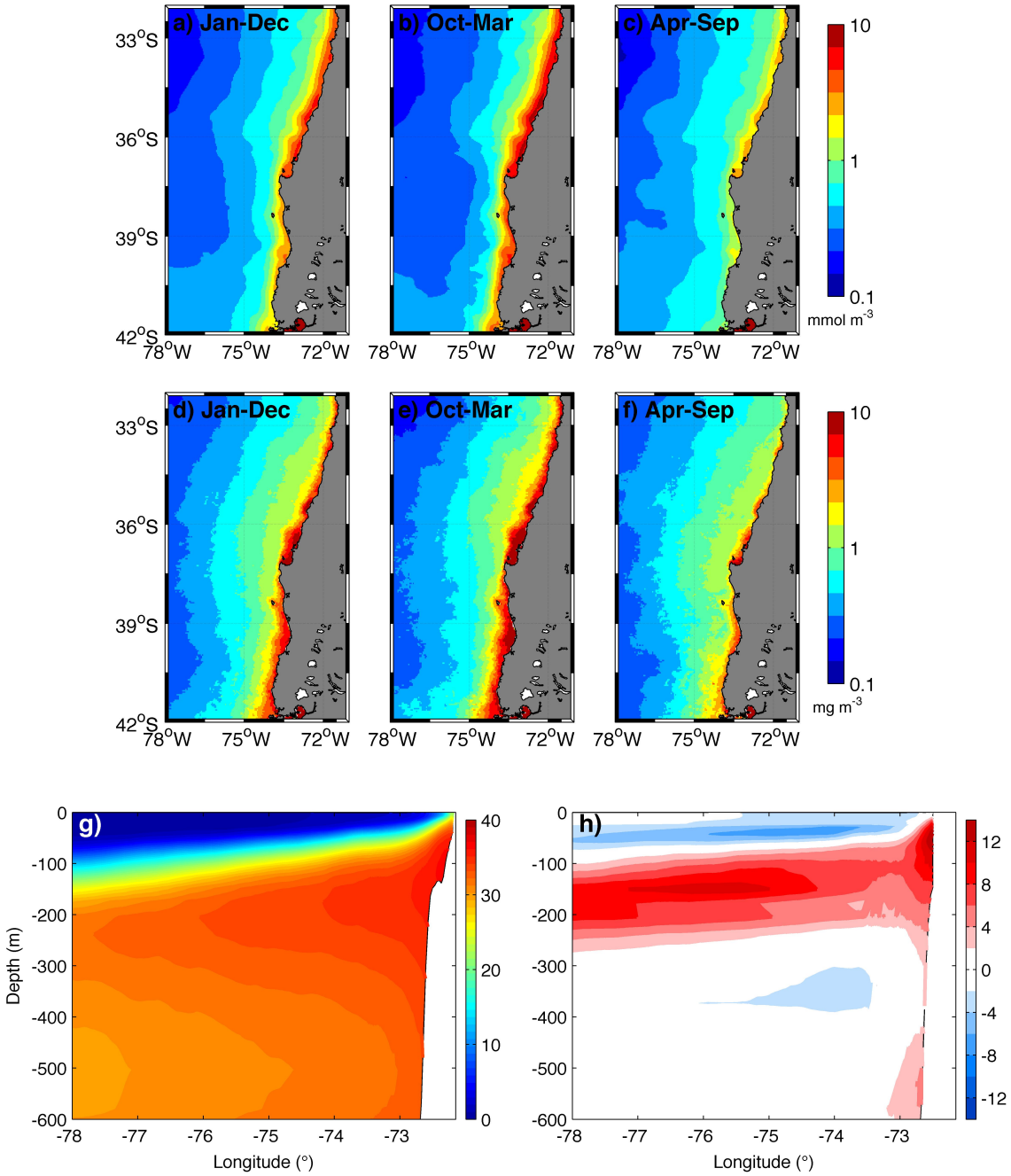

Figure A3 (legend on page 137)

Figure A1 (page 133). a) Annual mean model SST, b) model minus satellite annual mean SST, c) annual mean model mixed layer depth, d) model minus CARS annual mean mixed layer depth. Vertical sections at 35°S of e) annual mean model temperature, f) model minus WOA annual mean temperature, g) annual mean model meridional velocity. Model average fields were estimated for the six years: 2003-2008.

Figure A2 (page 134). a-h) Seasonal climatology (2003-2008) of sea level anomalies (cm) from model (a-d) and AVISO (e-h); i-j) Low-passed (cut-off frequency = 1/5 day^{-1}) time series of coastal sea level from model (red) and Valparaiso (i) and Talcahuano (j) coastal stations (blue).

Figure A3 (page 135). Mean model surface phytoplankton (a-c) and mean satellite chlorophyll-a (d-f); Vertical sections at 35°S of g) annual mean model NO_3, and h) model minus WOA NO_3 annual mean. Average fields were estimated for the period 2003-2008.